Cell-type-specific efferocytosis restricts the functional plasticity of alveolar macrophages to prioritize resolution of inflammation over antibacterial defense

Inaugural Dissertation

submitted to the

Faculty of Medicine

in partial fulfillment of the requirements

for the PhD-Degree

of the Faculties of Veterinary Medicine and Medicine

of the Justus Liebig University Giessen

by

Better, Julian

of

Marburg, Germany

Giessen, August 21st, 2025

From the Department of Medicine V, Infectious Diseases and Infection Control

of the Faculty of Medicine of the Justus Liebig University Giessen

Director: Prof. Dr. med. Susanne Herold, PhD

Chair: Prof. Dr. Friedemann Weber

Vice chair and Co-Supervisor: Prof. Dr. med. vet. Stephanie Krämer

First Reviewer and Supervisor: PD. Dr. med. univ. Ulrich Matt, PhD

Second Reviewer: Prof. Dr. Johan Garaude

Date of Doctoral Defense: December 8th, 2025

Table of contents

Introduction

Pneumonia, acute lung injury and Acute Respiratory Distress Syndrome

Definitions

Pneumonia, a common acute lower respiratory tract infection that affects the alveoli and distal airways, poses a significant global health challenge. It contributes more to the global disease burden than any other infectious disease and maintains high mortality rates despite decades of medical advancements. Even with the advent of antibiotics, bacterial pneumonias remain a substantial medical challenge, and the increasing prevalence of antibiotic resistance threatens modern medicine as a whole (1-3).

Pneumonia is broadly divided into community-acquired pneumonia (CAP) or hospital-acquired pneumonia (HAP) because of substantial differences in the causative microorganisms. While CAP is any pneumonia contracted outside the hospital or within 48 hours of hospital admission, HAP develops after 48 hours of hospital admission and includes ventilator-associated pneumonia (VAP) referring to patients that are endotracheally intubated for more than 48 hours necessitating invasive mechanical ventilatory support. Aspiration pneumonia, considered as part of the continuum between CAP and HAP rather than a distinct entity, occurs as a result of inhalation of contents from the stomach or pharynx into the lungs and is associated with worse outcomes, especially in older patients with comorbidities (4).

The most frequent causative microorganisms of CAP are *Streptococcus pneumoniae* (*S. pneumoniae*), *Mycoplasma pneumoniae*, *Haemophilus influenzae* (*H. influenzae*), and respiratory viruses. Less common bacterial pathogens, causing CAP, include *Legionella pneumophila*, *Chlamydia pneumoniae*, *Staphylococcus aureus* (*S. aureus*), *Enterobacteriaceae*, such as *Escherichia coli* (*E. coli*) and *Klebsiella pneumoniae* (*K. pneumoniae*), and *Pseudomonas aeruginosa* (*P. aeruginosa*). The most frequent viral pathogens isolated are influenza viruses, human rhinovirus, human parainfluenza viruses, Respiratory syncytial virus (RSV), human Metapneumovirus (HMPV), and Coronaviruses (CoV) (4-6).

Conversely, the most frequent microorganisms causing HAP and VAP are *Enterobacteriaceae*, non-fermenting gram-negative bacilli, such as *P. aeruginosa*, *Acinetobacter spp.*, and *Stenotrophomonas spp.*, as well as *S. aureus* (4, 5).

The widespread, gram-negative, aerobic, lophotrichous flagellated *P. aeruginosa* is of particular clinical relevance due to its inherent antibiotic resistance, its capability to develop additional resistance, and pathogenicity, which poses a significant therapeutic challenge. The pathogenicity of *P. aeruginosa* is mainly attributed to its numerous virulence factors and genetic adaptability, allowing it to thrive in diverse environments. Key virulence factors include surface structures like polar flagella, pili, and lipopolysaccharides (LPS), as well as secreted products, type-III secretion system proteins, quorum-sensing molecules, and alginate. Lung injury associated with *P. aeruginosa* is caused by both the organism's direct damage to lung tissue and the host's excessive immune response (7).

Overall, pneumonia is more frequently found in vulnerable groups, such as children under 5 years old and older adults with existing chronic illnesses. The progression of the disease primarily hinges on the host immune response (4, 6).

Immunosuppressed patients represent a distinct population where opportunistic infections also play a pivotal role. These include *Pneumocystis jirovecii* pneumonia, fungal infections like invasive broncho-pulmonary aspergillosis (IBPA), or viral herpes infections such as Cytomegalovirus (CMV) and Herpes simplex virus (HSV) pneumonia (8).

Lung tissue damage resulting from pneumonia or non-infectious insults can be life-threatening. This damage can manifest locally as acute lung injury (ALI) or systemically, as seen in sepsis with multi-organ dysfunction. ALI can progress to severe, life-threatening respiratory failure, known as acute respiratory distress syndrome (ARDS), often requiring invasive mechanical ventilation (1-3).

ARDS is characterized by the sudden onset of noncardiogenic pulmonary edema, hypoxemia, and the necessity for mechanical ventilation. The 2012 Berlin definition for diagnosing ARDS specifies that respiratory failure must occur within one week of a known injury or the appearance of new and/or worsening respiratory symptoms with radiographic evidence of bilateral opacities that cannot be fully attributed to cardiac failure, fluid overload, or other etiologies. The severity of ARDS is further graduated by the ratio of partial pressure of oxygen to the fraction of inspired oxygen (PaO_2/FiO_2) while applying positive end-expiratory pressure (PEEP) or continuous positive airway pressure (CPAP) (1-3, 9).

ARDS, and ALI in general, can be triggered by a variety of insults, classified based on their nature as either infectious or non-infectious, and origin as either pulmonary or extra-pulmonary. ARDS most commonly arises in the context of pneumonia (both bacterial and

viral), aspiration of oropharyngeal or gastric contents (referred to as “pulmonary acid aspiration”), sepsis (originating from the lungs, peritoneum, urinary tract, soft tissue, or skin), or severe trauma (including blunt or penetrating injuries or burns). Less common causes of ARDS include acute pancreatitis, transfusion-associated ALI, non-cardiogenic shock, and inhalation injury. Notwithstanding the diversity of ARDS etiologies, pneumonia and sepsis constitute the majority of cases (30-60% or 15%, respectively) (1-3, 9).

Clinical importance

About 10% of patients in the intensive care unit meet the criteria for ARDS, and 20 to 25% of all critically ill patients needing mechanical ventilation develop ARDS. Despite improvements in supportive care, ARDS continues to be a major cause of morbidity and mortality among critically ill patients, with mortality rates ranging from 35-46% (1-3, 9).

Some viruses are particularly prone to triggering severe pneumonia and ARDS, such as severe acute respiratory syndrome (SARS)-CoV (2003), Influenza virus (H1N1; 2009), Middle east respiratory syndrome (MERS)-CoV (2012), SARS-CoV2 (2019), which resulted in the coronavirus disease 2019 (COVID-19) pandemic, and RSV (9).

A substantial impact of respiratory viral infections lies in their ability to facilitate secondary bacterial pneumonia, with *S. pneumoniae* being the most frequently isolated microorganism complicating viral pneumonia. Secondary bacterial pneumonia occurs as the immune response triggered by the virus and damage to the epithelial cells increases host susceptibility to bacterial invasion, potentially leading to more severe and invasive infections (10-16).

During the 1918 influenza A (H1N1) pandemic, secondary bacterial pneumonias caused the majority of all influenza-related deaths, and they affected more than 30% of patients with 2009 pandemic influenza A (H1N1) who were treated in intensive care units worldwide. An extensive analysis of critically ill patients with 2009 pandemic influenza in U.S. intensive care units showed that bacterial coinfections typically occur within the first six days of influenza infection, exhibit symptoms similar to influenza alone, and significantly increase the risk of mortality (16).

While pneumonia is the leading primary cause of ARDS, secondary bacterial pneumonia also frequently complicates ARDS, thus worsening patient outcome. Consistent with this, patients with ARDS face a higher risk of developing secondary bacterial pneumonia compared to intubated patients who do not have ARDS (1-3, 17-20).

Particularly prevalent in critically ill patients, pulmonary acid aspiration leads to sterile pneumonitis. This condition occurs in patients with impaired consciousness—caused by factors such as general anesthesia and analgosedation, intoxication, or stroke—due to diminished reflexes and a reduced closure of the epiglottis (21).

Pulmonary acid aspiration has been found to occur in the great majority of intubated patients and is one of the strongest independent risk factors for the subsequent development of a VAP. Therefore, pulmonary acid aspiration and consecutive secondary bacterial pneumonia can trigger or worsen ARDS (21, 22).

Up to now, treatment of ARDS primarily involves lung-protective ventilation, as no specific therapeutics have been identified (23).

Conclusively, the absence of specific and effective treatments for ARDS, coupled with its unacceptably high mortality rate, highlights an urgent need for innovative therapeutic strategies.

Pathophysiology of acute lung injury

Humans rely on a constant supply of oxygen (O_2) to sustain metabolism and life. Unlike fuels such as carbohydrates, fats, and proteins, which can be stored in liver, fat tissue, or even cytoplasm, O_2 constantly needs to be supplied to mitochondria in accordance with the cell's immediate demands (24).

Inspiration carries air through the conducting zone of the respiratory tract including large airways until the distal bronchioles to deliver O_2 to the respiratory zone of the lung. The respiratory zone, comprised of the respiratory bronchiole, alveolar ducts, and alveoli, is the site of respiration where the actual gas exchange takes place (25).

Upon entering the bloodstream, O_2 is bound to hemoglobin and transported through the cardiovascular system to reach the peripheral cells while carbon dioxide (CO_2), a byproduct of metabolism, is eliminated from the body during expiration, following the opposite route (24). Inspiration and expiration, termed ventilation, requires lung parenchyma to expand or recoil, respectively, driven by the excursion of chest and diaphragm (26).

The lung comprises about 500 million alveoli, spanning a surface area of roughly 140m^2 comparable the size of a tennis court (25, 26). Alveoli are separated by an alveolar septum containing stromal cells, connective tissue, and pulmonary capillaries (27, 28). As a result, up to 95% of the alveolar surface is covered by pulmonary capillaries, the finest division of the

pulmonary vascular tree. The air-blood barrier, a membrane of less than 1μm, separates alveolar air from the pulmonary circulatory system, allowing gases to diffuse rapidly between them within 0.25-0.75 seconds (25).

Alveolar epithelial cells (AECs) type I and endothelial cells line the alveolar space or pulmonary capillaries, respectively. Therefore, the air-blood barrier is formed by AECs type I and endothelial cells including their basement membranes. AECs type I cover 95% of the inner surface of each alveolus owing to their very thin and elongated shape. They facilitate gas-exchange and maintain ion and fluid balance within alveoli. On the other hand, twice as much but significantly smaller cuboidal AECs type II complete the mosaic of the alveolar epithelium. They secrete lung surfactant and serve as a local stem cell niche, thereby regulating alveolar surface tension or regenerating alveolar epithelium after lung injury, respectively (27-29).

Various soluble factors, such as mucins, lysozyme, lactoferrin, immunoglobulins A and G, and defensins, in the airway fluid contribute to the first line of defense (30-32).

Stromal cells including fibroblasts differentiate towards lipofibroblasts, myofibroblasts, pericytes, or other cell types. They produce collagen and elastic fibers offering mechanical support and provide nutritional factors (27-29).

Tissue-resident alveolar macrophages (AMs), the most abundant immune cell type in the distal lung parenchyma, are mononuclear phagocytes situated at the luminal side of alveoli closely attached to the airway epithelium patrolling in distal airways and alveoli to phagocytose foreign material and pathogens (27).

Conclusively, sustaining life through the effective gas exchange requires the elaborate interplay between respiration, ventilation, and perfusion facilitated by the structural and functional microarchitecture of the lung.

In contrast to lung homeostasis, ALI/ARDS is associated with several local and systemic pathological changes, including immune dysfunction, inflammatory responses, and abnormal coagulation. A variety of cells, especially macrophages, monocytes, dendritic cells (DCs), polymorphonuclear neutrophils (PMNs), T-cells, epithelial cells, and endothelial cells, contribute to these processes. These cellular activities cause abnormalities in lung tissue, leading to the pathognomonic damage of the alveolar-capillary barrier (1-3).

In the affected lung tissue, several pathological changes are evident, including dysfunction of the endothelial barrier, presence of cell-free hemoglobin, impaired clearing of pulmonary edema, cell death, cellular aging, and cellular dysfunction. Hence, pathological samples from

ARDS patients often show diffuse alveolar damage with accumulation of protein-rich inflammatory fluid in the alveolar space resulting in impaired gas exchange, increased work of breathing, and radiographic alterations (1-3, 33).

In ARDS, both local and systemic inflammation play key roles in damaging lung epithelial and endothelial cells with divergent views on the initiation of the inflammatory syndrome (33).

Activated AMs in the lungs release a plethora of pro-inflammatory mediators in response to external stimuli, which stimulates the surrounding tissue and recruits other inflammatory cells, such as neutrophils and monocytes, into the microvasculature, prompting their migration into the airways (34).

In addition, blood-derived factors activate the intravascular immune system, causing neutrophils to infiltrate the lung capillaries, adhere to or become trapped within these small vessels, and disrupt the vital oxygen-exchanging alveolar–capillary unit (34, 35).

Activated PMN, typically absent in healthy airspaces, are recruited from lung blood vessels early in ARDS contributing to tissue damage by the release of oxidants, proteases, additional inflammatory mediators such as prostaglandins and leukotrienes, and neutrophil extracellular traps (NETs). NETs, made up of DNA, myeloperoxidase (MPO), histones, and proteases, further intensify inflammation by activating the NLRP3 inflammasome, which leads to the release of IL-1β and IL-18 (33, 35). This intense inflammatory response triggers platelet aggregation and the formation of microthrombi in the lung vasculature, which causes death to erythrocytes, epithelial and endothelial cells with formation of paracellular gaps (36).

Increased epithelial and endothelial permeability further promotes influx of inflammatory cells into inflamed alveoli. While being a necessity for effective clearance of pathogens, it also leads to impaired barrier function promoting interstitial and alveolar edema (37).

Additionally, impaired transepithelial ion transport, due to decreased activity, expression, or mislocalization of epithelial sodium and chloride channels as well as the Na^+/K^+-ATPase, leads to reduced clearance of alveolar edema (38).

Infiltrated leukocytes release soluble, death-inducing ligands, such as tumor necrosis factor alpha (TNF-α) and TNF-related apoptosis-inducing ligand (TRAIL). These ligands attach to receptors on epithelial cells, triggering intracellular pathways that lead to cell death and damage to the air-blood barrier (3).

Furthermore, bacterial pathogens can promote tissue damage by release of toxins, such as α-hemolysin and β-toxin secreted by *S. aureus* (39).

Cell-free hemoglobin from ruptured erythrocytes contribute to increased barrier permeability (39) while formation of fibrin and hyaline membranes over the exposed basal membrane further impair gas exchange (3).

For patients with ARDS, mechanical ventilatory support is essential and lifesaving, but high tidal volumes, inspiratory pressures, or both can exacerbate the inflammatory response and dysfunction of the pulmonary endothelial barrier. This mechanical ventilation enhanced worsening of the ALI is referred to as ventilator-associated lung injury (33, 37).

Pathological changes of the alveolar microenvironment during ALI/ARDS as opposed to homeostasis are depicted in Fig. 1.

From an immunological perspective, ARDS can be divided into hypoinflammatory and hyperinflammatory subphenotypes based on the systemic host response. Still, systemic host responses in ARDS do not always reflect the alveolar host response. Discrepancies have been noted between the levels of proinflammatory cytokines in bronchoalveolar lavage fluid and those in the systemic circulation. This indicates that inflammatory heterogeneity in ARDS is multidimensional, encompassing subphenotypes of both systemic and alveolar inflammation (33, 38).

Attempts to modulate inflammation for the treatment of ARDS have failed to demonstrate a mortality benefit (34, 36).

Therefore, putative therapeutic applications warrant a deeper understanding of the immunological phenotypes influencing ARDS pathology.

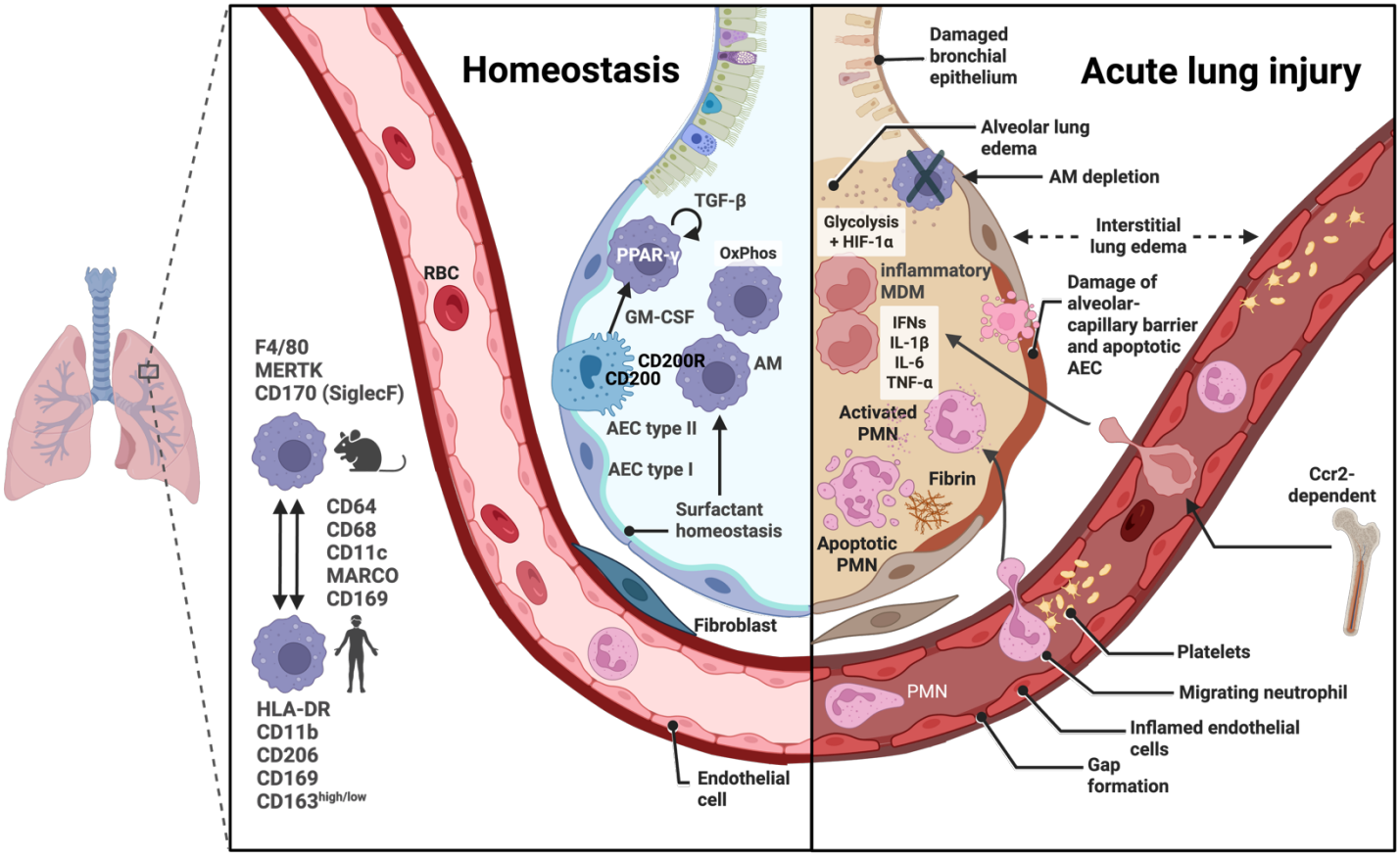

Figure 1. Alveolar microenvironment during homeostasis and acute lung injury

Left: Immunophenotypical identity of mouse and human AMs (hAMs) including conserved markers.

Homeostasis: AMs are maintained by TGF-ß and AEC type II-derived GM-CSF promoting PPAR-γ transcription. Macrophage and epithelial receptor-ligand interaction, e.g. engagement of CD200R/CD200 regulate AM responses. AMs rely on oxidative phosphorylation (OxPhos) for lipid catabolism.

ALI: The alveolar microenvironment shows desquamated bronchial epithelium, damaged alveolar-capillary barrier, and alveolar/interstitial edema. The vascular compartment is compromised revealing inflamed endothelial cells, paracellular gap formation, migrating leukocytes, dying erythrocytes, and immunocoagulopathy indicated by platelet aggregation. Apoptotic PMNs and AECs accrue. Ccr2-dependent recruited bone marrow-derived inflammatory MDMs and recruited activated PMNs contribute to inflammation characterized by interferons (IFNs), IL-1ß, IL-6, TNF-α. Glycolytic MDM metabolism stabilizes HIF-1α. Fibrin and hyaline membranes covering the exposed basal membrane further impair gas-exchange. Fibroblasts are activated.

*Created with BioRender.com; based on Bain CC, MacDonald AS, 2022 (40) and Pervizaj-Orugaj L, Ferrero MR, Matt U, Herold S, 2023 (205).

Macrophages

Heterogeneity of Macrophages

Macrophages are primarily stationary phagocytes that reside within the tissues of every organ throughout the body. Macrophage biology has been a subject of study for over a century, ever since Elie Metchnikoff first described them at the end of the 19th century. However, the past two decades have arguably brought significant changes to fundamental concepts in macrophage biology, including a deeper understanding of their identity and their capacity to self-renew locally (40).

While traditionally, based on in vitro culture systems using bone marrow-derived macrophages (BMDMs), macrophages have been categorized as M1 ("classically activated") or M2 ("alternatively activated"), it is now clear that this binary classification fails to capture the complexity in terms of different organ-specific macrophages and in terms of macrophage plasticity *in vivo* (41).

Advances in technology have unveiled a significant amount of heterogeneity among macrophages from different organs and from different niches of the same tissue, in terms of their immunophenotype, transcriptome, and metabolome (42, 43).

Macrophages have been appreciated for clearance of debris, apoptotic cells, and invading pathogens but it has only recently become evident that they also fulfill much broader roles and are precisely adapted to the needs of the local tissue microenvironment in which they reside in. Indeed, diverse, spatially and temporally dynamic microenvironmental cues encountered by macrophages *in vivo* are the primary factors determining macrophage differentiation, activation, and function (40).

Alongside, the importance of microenvironmental imprinting is underscored by the unique function of the specific organ they reside in. For example, cardiac macrophages participate in electric signal conduction and peritoneal macrophages reside in a rather sterile microenvironment while AMs are constantly exposed to the surrounding environment at the gas exchange surface in the alveolar niche.

This underscores the importance of thoroughly considering the tissue-specific environment, both in steady state and during inflammation, in order to fully comprehend the role of tissue-resident macrophages.

Ontogeny of tissue-resident lung macrophages

A lot of phenotypically and transcriptionally different lung macrophages exist which are distributed throughout the lung and can broadly be divided into tissue-resident versus recruited macrophages. Tissue-resident lung macrophages are separated in alveolar (=airway) and interstitial (=parenchymal) macrophages (AMs or IMs, respectively), based on the anatomical location they reside (40).

Tissue-resident macrophages originate from at least two distinct erythro-myeloid progenitors (EMPs) that emerge and develop in the extra-embryonic yolk sac at embryonic days 7.5 (early EMPs) and 8.5 (late EMPs). The late EMPs transition through an intermediary monocytic stage in the fetal liver. In mice, the AM pool develops from yolk sac-derived early EMPs at embryonic age E8.5-9.0. Secondly, the AM pool is expanded by fetal liver monocytes originating in the fetal liver from yolk sac-derived late EMPs from E12.5 onward. In the following, AMs differentiate into long-lived cells governed by unique environmental stimuli, fully populating the alveolar space from the first week postnatally onward (44-47).

Recent evidence has demonstrated superior developmental and functional capacity of fetal monocytes over primitive macrophages in AM development. Fetal monocytes, driven by Myb, outcompeted primitive macrophages in empty alveolar niches, preferentially differentiating into mature AMs. This process is linked to increased mitochondrial and glycolytic capacity, combined with the suppression of transcription factors c-Maf and MafB. Notably, AMs originating from primitive macrophages were ineffective in clearing alveolar proteinosis and in providing protection against fatal lung failure after influenza virus infection (48).

In general, murine studies indicate that tissue-resident macrophages can have a remarkably long lifespan (ranging from months to years up to a life span in organs such as the brain, liver, lungs, and skin). Moreover, they are capable of self-renewal, sustaining their homeostatic population without input from circulating monocytes. In contrast, in other tissues, the populations of tissue-resident macrophages are replenished by monocyte-derived cells at varying intervals. For instance, in the intestine, locally sustained tissue-resident macrophages coexist with monocyte-derived populations that have a relatively short lifespan, each serving unique functions crucial for maintaining gut homeostasis and supporting intestinal physiology (40, 46, 49, 50).

The adult AM pool is thought to self-renew locally with neglectable contribution of monocytic precursors during homeostasis (40, 49).

Still, using a humanized mouse model, classical CD14+CD16- monocytes have been identified as circulating precursors of lung tissue monocytes as well as IMs and AMs (51).

The homeostatic framework changes upon tissue injury. ALI depletes AMs to varying extent depending on nature and severity of the insult. After ALI has subsided, replenishment of the AM pool preferably depends on local proliferation of AMs. However, during more severe ALI (e.g. IAV pneumonia or COVID-19), circulating Ly6C^{hi} (lymphocyte antigen 6 family member C) blood monocyte precursors are recruited to the lung to aid in the inflammatory response and replenish parts of the depleted AM pool by differentiating towards AM-like macrophages dependent on several genes, including Torc1, Pparg, and Tgfb1, as well as microenvironmental and niche-specific signals (50, 52-56).

Opposing to a single influx of monocytes that gradually transform into pro-resolving AM-like macrophages, an alternative model has been proposed. Thereby, successive waves of different MDMs may participate in both tissue injury and repair including replenishment of the AM pool (50).

Interestingly, with accumulating injurious events throughout the life span, MDMs might surpass AMs in quantity paralleled with a gradual decrease in the number of AMs with aging. These changes in the AM pool may significantly alter host defense and partially be causative of the increased susceptibility to lung infection and severity of lung injury observed in the elderly population (57-59).

Notwithstanding that, replenishment of the AM pool after ALI and the recruitment dynamics of MDMs to tissues is an area of ongoing research. Prospectively, it remains to be clarified how different lung inflammatory conditions alter the AM subset diversity and function throughout the life span.

Identity and phenotype of tissue-resident lung macrophages

Lung tissue-specific identity of AMs is facilitated by granulocyte-macrophage colony-stimulating factor (GM-CSF), mainly released by AECs type II (44). GM-CSF activates peroxisome proliferator-activated receptor gamma (PPAR-γ), a nuclear receptor involved in the regulation of fatty acid degradation, lipid transport and storage, as well as cholesterol metabolism (Fig. 1, 60). Additionally, PU.1 has been shown to be important for terminal differentiated AMs by mediating GM-CSF-dependent effects on innate immune functions and surfactant catabolism (61).

Moreover, AM development and differentiation is regulated by BACH2 (B lymphoid transcriptional repressor broad complex tramtrack bric-á-brac and Cap'n'collar homology 2) being involved in the regulation of lipid and cholesterol metabolism as well as TGF-β promoting differentiation of AMs and maintaining homeostasis in an autocrine manner (62). Low levels of macrophage colony-stimulating factor (M-CSF) as well as ZEB2 (zinc finger E box binding homeobox 2 transcription factor) and neutrophil-derived 12-hydroxyeicosatetraenoic acid (12-HETE) are required for survival or tissue-specific identity of AMs, respectively (63-65).
Murine AMs of uninflamed lungs are immunophenotypically characterized by high expression of CD170 (cluster of differentiation 170), alias Siglec-F (sialic-acid-binding immunoglobulin-like lectin F), integrin CD11c, CD169 (Siglec1), scavenger macrophage receptor with collagenous structure (MARCO), CD64 (high affinity FcγR1), CD68 (lysosomal membrane glycoprotein), and efferocytic receptor MerTK (Mer-tyrosine kinase), while lacking surface expression of integrin CD11b and pattern recognition receptor CD14 (40, 54, 66, 67).
Transcriptionally, murine AMs are defined by a high expression of Ear1, Pparg, Chil3, Fabp4/5 (40, 54, 66, 68-70).
A fraction of the residing AM pool can be retrieved by bronchoalveolar lavage (BAL) with AMs posing the sole macrophage population in the recovered bronchoalveolar lavage fluid (BALF) and airways in healthy lungs (67).
On the other hand, murine IMs express high levels of CD11b while lacking expression of SiglecF (40, 54, 66, 67). There is much less known about IM identity compared to AMs, owing to the difficulty of isolating them from intact lung tissue when applying standard protocols for enzymatic digestion (67).
Immunophenotypically, at least three distinct subsets of IMs have been identified based on the expression of CD11c, CD206 (mannose receptor), major histocompatibility complex class II (MHC-II), Lyve1, CD169, and CCR2 (67). Based on this, IM1 ($CD11c^{low}MHC\text{-}II^{low}$), IM2 ($CD11c^{low}MHC\text{-}II^{high}$), and IM3 ($CD11c^{+}MHC\text{-}II^{high}$) are flow-cytometrically distinguished during homeostasis. In addition, all IMs express F4/80, CD64, CD68, CD11b, and CX3CR1 (40, 67).
Lung IMs are parenchymal macrophages that are supposed to be derived from postnatal monocytes (67, 71). TGF-β1 released from endothelial cells is required for IM development and function in the murine lung (71).
Spatially, $CD169^{+}$ nerve- and airway associated IMs have been described (72). They are localized around the large bronchiolar airways in close proximity to sympathetic airway-

associated nerves embedded in the bronchovascular bundle. Functionally, these IMs are required for restricting viral spread and regulating lung inflammation (72). IMs have also been shown to mediate the clearance of apoptotic alveolar epithelium during influenza infection and therefore actively contributes to resolution of inflammation (73).

The aforementioned expression markers of murine lung-resident macrophages show overlap with expression profiles of other myeloid cells, especially $CD11c^+$ DCs and Siglec-F^+CD11b^+ eosinophils. Hence, for identification by flow cytometry, additional markers like CD64, CD68, and/or MerTK, help to appropriately distinguish tissue-resident lung macrophages from other leukocytes (54, 66).

Immunophenotyping of human AMs (hAMs) shows high levels of HLA-DR, CD206, CD169, MARCO, CD64, and CD68. Importantly, Siglec8, the human paralog of the defining characteristic marker of murine AMs, Siglec-F, is absent in hAMs (40, 66). They can be subdivided into the numerous $CD163^{hi}$ and rare $CD163^{low}$ AMs. Transcriptionally hAMs are characterized by expression of Fabp4, Serping1 and Apoc1 (40, 66).

Nonetheless, human and murine AMs share core gene signatures including the expression of Pparg, Fabp4, Ffar4, and Fn1 (40, 66).

Immunophenotypical identity of mouse and hAMs including conserved markers are depicted in Fig. 1.

Phenotypic and transcriptional characteristics of human IMs in homeostasis are less understood due to limited access to healthy human lung tissue. Currently, human IMs are identified as HLA-$DR^+CD36^+CD11b^+CD169^-$ (66, 67). Limited evidence suggests varying expression of HLA-DR and CD36 defining different human IM subsets (74).

Noteworthy, neither AMs nor IMs can be classified using the M1/M2 system as both types of macrophages simultaneously express M1 and M2 markers during homeostasis emphasizing the inadequacy of applying the M1/M2 model *in vivo*.

Function and plasticity of alveolar macrophages

AMs are the most abundant leukocytes in the distal lung acting as sentinel cells essential for maintenance of homeostasis, clearance of smaller amounts of bacteria to avert invasive infection, orchestration of inflammation, as well as resolution of inflammation (27, 75, 76). Thus, AMs are plastic cells that must swiftly adapt anti- and pro-inflammatory properties aiming to restore tissue homeostasis (75).

Although, AMs only reside in one out of three alveoli, the pores of Kohn enable AMs to migrate between adjacent alveoli (60).

Morphologically, AMs are large, vacuolar cells, with prominent pseudopodia, qualifying them for phagocytosis of cellular debris, senescent cells, and pathogens (68).

In order to prevent excessive and potentially damaging pro-inflammatory reactions in response to environmental antigens encountered by AMs during homeostasis, these cells are kept in a hyporesponsive state through a variety of inhibitory mechanisms, such as mannose receptor, MARCO, CD200R, TREM2, IL-10R, TGF-βR, necessitating physical engagement with AECs (75).

In the absence of infection, AMs regulate pulmonary surfactant, a lipid-protein complex produced by AECs type 2 that reduces surface tension preventing alveoli from collapsing, thus, allowing for efficient ventilation and gas exchange. In line, the transcriptional profile of AMs demonstrates the importance of lipid metabolism in both mice and humans. Surfactant metabolism requires the key regulator GM-CSF to activate PPARγ. Genetic mutations or autoimmunity affecting GM-CSF, GM-CSF receptor, or PPARγ signaling lead to immature and dysfunctional AMs resulting in spontaneous pulmonary alveolar proteinosis (PAP) due to accumulation of surfactant and defective surfactant catabolism. Consequently, PAP can lead to impaired gas exchange and increased susceptibility to infection (Fig. 1, 56, 77).

AMs produce immunomodulatory cytokines, especially TGF-β and interleukin-10 (IL-10) , which regulate ion and fluid transport in AECs (75). Furthermore, AM-released extracellular vesicles containing SOCS (suppressor of cytokine signaling) modulates epithelial responsiveness to toll-like receptor (TLR) ligands. Thereby, AMs also help regulating the integrity and responsiveness of the airway epithelium (75).

While AMs are typically kept hyporesponsive in non-inflammatory alveolar spaces, they are capable of switching to pro-inflammatory roles under certain conditions. This switch can be triggered by the destruction of AECs and the resulting loss of immunosuppressive ligands as well as recognition of pathogen-associated molecular patterns (PAMPs) and damage-associated molecular patterns (DAMPs) indicating infection or injury, respectively. Being equipped with various pattern recognition receptors (PRRs), such as toll-like receptors (TLRs), nucleotide-binding oligomerization domain-containing protein (NOD)-like receptors, and retinoic acid inducible gene-I (RIG-I)-like helicases, AMs can inhibit IL-10 receptor signaling and activate pathways involving IL-1R-associated kinase, p38, and NF-κB signaling, thus

promoting inflammation. Upon activation, AMs increase their phagocytic activity and secrete oxygen-, arachidonic acid-, and nitric oxide (NO) derivatives, as well as pro-inflammatory cytokines (like IL-1, IL-6, and TNF-α), chemokines, lysozymes, antimicrobial peptides, and proteinases (78-82).

Immunometabolism of macrophages

An evolutionary perspective on immunometabolism

Species, organisms, and cells must all grow and reproduce or survive dynamic environments with a limited pool of resources. Metabolic reprogramming, the proper allocation of the limited pool of resources controlled by intrinsic and extrinsic signals, is necessary to achieve fundamental processes of life. An evolutionary framework on metabolic reprogramming conceptualizes how resources are allocated between growth, reproduction, and maintenance programs as a function of environmental quality. Maintenance programs can be divided into two metabolically distinct programs: the energy-preserving, catabolic dormancy programs and the energy-consuming anabolic defense programs. On the cellular level, activated immune cells largely require glucose to mount a robust response. This is consistent with the anabolic processes that immune cell activation entails, including rapid proliferation and synthesis of biomolecules, including cytokines, antimicrobial proteins and lipid mediators. Simultaneously, tissues not directly involved in the immune response engage catabolic metabolism and switch fuel usage from glucose to fatty acids and ketones, which support tissue protective pathways, since dormancy programs in general, such as hibernation, are highly resistant to stress. Consecutively, immunometabolism describes how changes in cellular metabolism of immune cells alters their immune effector function and vice versa, providing a fundamental explanation for cellular plasticity, and aiming to explore the link between metabolic regulation and various disease states (83).

The field of immunometabolic research has been pioneered by Warburg in the 20th century by describing the metabolic alterations and aerobic glycolysis occurring in cancer cells and has gained significant attention over the last 15 years facilitated by new unbiased omics-approaches (84).

Impact of metabolic pathways and metabolites on immune functions in macrophages

Six major metabolic pathways, glycolysis, the tricarboxylic acid (TCA) cycle, the pentose phosphate pathway (PPP), fatty acid oxidation (FAO), fatty acid synthesis (FAS) and amino acid (AA) metabolism, are involved and closely connected to oxidative phosphorylation (OxPhos). Because TCA cycle, FAO, and OxPhos occur in mitochondria, they are key immunometabolic hubs (85).

A hallmark metabolic change of pro-inflammatory macrophages is enhanced glycolysis. Glycolysis is not the most efficient method for ATP production as it only produces 2 ATP molecules from 1 glucose molecule, whereas oxidative phosphorylation yields 36 ATP molecules from a single glucose molecule (85). However, glycolysis can be quickly activated through the induction of its related enzymes. In contrast, enhancing oxidative phosphorylation requires mitochondrial biogenesis, which is a more complex and likely slower process. Therefore, cells needing rapid ATP production often switch to glycolysis. Even more crucial than quick ATP generation is glycolysis's ability to supply biosynthetic intermediates necessary for rapid cell growth. Growth factors and other activating signals stimulate increased glucose uptake and glycolysis, which provides ATP, supports the TCA cycle, and supplies intermediates for the pentose phosphate pathway, glycosylation reactions, and the synthesis of essential biomass components such as serine, glycine, alanine, and acetyl-CoA for lipid synthesis (85).

As a result of metabolic adaptations, metabolic intermediates of the TCA cycle accumulate and play roles beyond metabolism, particularly in macrophages which are involved in the regulation of inflammation, resolution, and repair (85).

Citrate is exported from the mitochondria and used to produce fatty acids, essential for membrane biogenesis. Additionally, excess citrate can be channeled into pathways that produce nitric oxide and prostaglandins, which are vital effector molecules for macrophages (85).

Another metabolite derived from citrate is itaconic acid, which is one of the highest induced metabolites in activated BMDMs and has been demonstrated to possess direct bactericidal properties, e.g. against *Salmonella enterica* ssp. *enterica* serovar *Typhimurium* and *Mycobacterium tuberculosis* while other bacteria, such as *S. aureus* and *P. aeruginosa*, exploit host-derived itaconate to facilitate biofilm formation (85, 86). However, accumulating

evidence has been focusing on its important immunomodulatory and -suppressive role. Itaconate inhibits succinate dehydrogenase (SDH), thereby reducing reverse electron transport (RET), mtROS production, and HIF-1α-dependent secretion of pro-inflammatory cytokines including IL-1β, IL-18, IL-12, and IL-6 while promoting mitochondrial RNA release and interferon (IFN) type 1 signaling (86-90). Itaconate also suppresses IRAK4, leads to the degradation of nuclear factor κB (NF-κB), and alters ubiquitination, affecting cytokines such as TNF-α (86). Itaconate alkylates Kelch-like ECH-associated protein 1 (KEAP1) and activates nuclear factor erythroid-derived 2-related factor-2 (Nrf2), which helps modulate oxidative stress and enhances macrophage phagocytosis (91), and it directly inhibits TET-2, reducing the transcription of pro-inflammatory genes (92). Importantly, glucocorticoids have been shown to increase itaconate production to mediate their anti-inflammatory responses (93). Increased production of itaconate has also been observed upon mitochondrial reprogramming in an uncoupling protein 2 (Ucp2)-dependent manner which triggers GATA3-induced differentiation of pro-resolving macrophages in response to the alarmin IL-33 and independent of IL-4. Remarkably, IL-33 initially induces the expression of pro-inflammatory genes in BMDMs before skewing their plasticity towards pro-resolving alternatively activated macrophages. The targeted deletion of GATA3 in mononuclear phagocytes effectively halted the IL-33-driven differentiation of alternatively activated macrophages and subsequently impaired tissue repair *in vivo* using a murine model of muscle injury (94). In a murine model of LPS-induced ALI, pre-treatment with 4-OI significantly reduced ALI, as evidenced by decreased pulmonary edema, reduced infiltration of inflammatory cells, and lower production of inflammatory cytokines. Stimulation with LPS triggered NLRP3-mediated pyroptosis both *in vitro* and *in vivo* through cleavage of gasdermin D (GSDMD) and, consecutively, release of IL-18 and IL-1β. This was preventable with 4-OI pre-treatment as 4-OI reduced mitochondrial reactive oxygen species (mtROS) production and prevented mitochondrial DNA release into the cytosol by inhibiting the opening of the mitochondrial permeability transition pore (mPTP) in AMs under oxidative stress. Furthermore, 4-OI pre-treatment significantly suppressed the expression of cyclic GMP-AMP synthase (cGAS), stimulator of IFN genes (STING), and phosphorylation of IFN regulatory factor 3 (IRF3) both *in vitro* and *in vivo*. Mechanistically, this study demonstrates that 4-OI ameliorates ARDS by restoring mitochondrial function and inhibiting NLRP3-mediated pyroptosis in AMs (95). Surprisingly, recent evidence has shown that the anti-inflammatory metabolite itaconate enhances AM-mediated inflammatory responses by

inhibition of succinate dehydrogenase and consecutive NLRP3 inflammasome-dependent pyroptotic response, thus worsening lung injury *in vivo* (96). Interestingly, this effect has not been observed with itaconate derivatives (96), which might be due to their their comparatively low inhibitory potential of succinate dehydrogenase (SDH) (97). In addition, the anti-inflammatory effect of itaconate on MDMs has been reproduced, therefore suggesting differential roles of itaconate on AMs and MDMs (96).

Hence, these findings underscore the importance to study tissue-specific responses of macrophages.

Accumulation of succinate in activated macrophages evokes a pro-inflammatory immune response, e.g., through inhibition of prolyl hydroxylases (PHD) or mtROS production which leads to the stabilization of HIF1α and continuous production of IL-1β (89, 98, 99).

Opposingly, the generation of α-ketoglutarate (αKG) through glutaminolysis or glycolysis-dependent fueling of the TCA-cycle is critical for the alternative (M2) activation of BMDMs. Epigenetic reprograming through αKG-dependent dioxygenases, namely the Jumonji-C (JmjC) family of lysine demethylases (KDMs) (JmjC-KDMs), ten-eleven translocation (TET) DNA cytosine-oxidizing enzymes, and PHDs, plays an important role. For example, αKG promotes FAO, OxPhos, and the Jmjd3-dependent epigenetic reprogramming of M2-specific genes strengthened by a high αKG/succinate ratio. In this regard, αKG plays a crucial role in contributing to endotoxin tolerance following M1 activation. In BMDMs, α-KG inhibits M1 polarization by enhancing PHD activity to suppress IKKβ activation and the consecutive NF-κB-dependent inflammatory response (100, 101). In AMs, αKG inhibits the polarization towards an M1 phenotype by suppressing the mTORC1/p70S6K pathway. Simultaneously, it promotes the M2 phenotype by enhancing the nuclear translocation of PPARγ, thereby ameliorating murine LPS-induced ALI/ARDS (102). Moreover, the production of α-KG, boosted by Rspondin3-driven metabolism, aids in catalyzing DNA hydroxymethylation via TETs in IMs during ALI. This process aids in the epigenetic reprogramming of IMs preventing inflammatory lung injury (103).

Fumarate is another important TCA-metabolite involved in immunometabolic reprogramming of macrophages (104, 105). Viral infection-induced inflammation leads to a reconfiguration of the urea cycle and TCA cycle in murine and human BMDMs, fueling a cyclic pathway known as the aspartate–argininosuccinate (AAS) shunt. Fumarate production by the AAS shunt is driven by argininosuccinate synthase (ASS1) in the cytosol enhancing inflammation. The

genetic removal of ASS1 lowers intracellular fumarate levels, decreases IFN-β production, and suppresses mitochondrial respiration (104). In addition, fumarate produced during viral infections, such as *Influenza A virus* IAV, or fumarate esters increase IFN-β output of BMDMs by directly succinating the mitochondrial antiviral signaling (MAVS) protein and, thereby, activating the retinoic acid-inducible gene (RIG)-I-like receptor pathway (105). Interestingly, dimethyl fumarate (DMF), a fumarate derivative, has been employed for decades in the treatment of relapsing-remitting multiple sclerosis (RRMS) and psoriasis. It demonstrates beneficial anti-inflammatory effects across a variety of immune cells including macrophages. Conversely, reduced expression of fumarate hydratase (FH) a TCA cycle enzyme that converts fumarate to malate is associated with chronic inflammatory diseases such as systemic lupus erythematosus (SLE) or systemic sclerosis (105).

Moreover, fatty acid synthesis (FAS) is another metabolic imprint of pro-inflammatory macrophages while, opposingly, fatty acid oxidation (FAO) preferentially supports non-inflammatory, tolerogenic, and alternatively activated macrophages (83). Accumulation of fatty acids and lipoproteins in macrophages is linked to the formation of foam cells and progression of inflammatory diseases, including atherosclerosis. Enhancing FAO, e.g., by boosting expression of a constitutively active form of CPT1A in macrophages, decreases lipid accumulation and reduced inflammatory cytokine production (85). BMDMs, activated by IL-4, rely on FAO. This M2 pathway is driven by the signal transducer and activator of transcription 6 (STAT6) and PPARγ-co-activator 1β (PGC1β), which helps suppress inflammatory signals (85). Overall, FAO and FAS appear to have opposing roles in the immune system (85).

Moreover, the metabolism of amino acids (AAs) such as glutamine, arginine, and tryptophan is crucial to moderate the function of immune cells (85).

Glutamine catabolism plays a crucial role in regulating various aspects of immune cell function, is thought to be particularly important in immune responses to severe conditions like sepsis, and burns (106). Sufficient glutamine levels are necessary for the production of IL-1β and generating nitric oxide (NO) in BMDMs by contributing to arginine synthesis following LPS stimulation (85).

Arginine is metabolized through two primary pathways in BMDMs, the NO synthesis and arginase pathways. When macrophages channel arginine into the NO synthesis pathway, arginine is converted to NO via citrulline, facilitated by inducible NO synthase (iNOS) leading to an inflammatory M1 phenotype. In contrast, arginine's flow through the arginase pathway

is linked to a tolerant and regenerative immune response promoting collagen formation via proline and cell proliferation through ornithine and polyamines (85).

Tryptophan plays a critical role in modulating immune function while especially its catabolism by macrophages prevents proliferation of pathogens and T-cells (85).

Finally, the cell employs master regulators to sense environmental conditions. Amino acid abundancy and energy status are sensed through activity of mTOR or AMPK, respectively, thereby coupling environmental conditions to growth, proliferation, and immunity (85).

Still, mechanistically, most of the insight gained into immunometabolism has been derived from studies using *ex vivo*-generated macrophages or *in vitro* cell lines, lacking the specific microenvironment and disease context *in vivo*.

Immunometabolism in a lung-specific context

Alveolar macrophages are situated in a distinctly unique microenvironment, the alveolar niche. The alveolar niche is continuously exposed to the external environment through respiration, characterized by high oxygen levels, an abundance of phospholipids and cholesterol, and a low concentration of glucose. During homeostasis, alveoli feature some of the highest oxygen concentrations in the human body, with a partial pressure of approximately 100mmHg at sea level, equivalent to 13.2% O_2. Given that pulmonary surfactant is a rich source of phospholipids and cholesterol, AMs are equipped for lipid catabolism and cholesterol handling and therefore poised to engage in OxPhos during homeostasis. Dysfunctional OxPhos impairs homeostasis and their capacity to self-maintain leading to local AM depletion. Moreover, the glucose concentration in the airway lumen is about one-tenth of that found in the blood, making the airway one of the environments with the lowest glucose levels encountered by cells (107-109). Tissue-resident AMs exhibit relatively low expression of glycolytic proteins and do not rely on glycolysis for LPS-induced inflammation. Additionally, glycolysis alone is insufficient to maintain normal AM function when the ETC is inhibited. This indicates that AMs have a glycolytic deficiency and cannot rely solely on glycolysis-derived energy for survival (110).

However, acute inflammation can drastically change the airway environment. Fluid buildup and impaired gas exchange during ARDS/ALI dramatically alter homeostatic conditions to a microenvironment characterized by high glucose and low oxygen levels as well as decreased lipid and protein (107). Under hypoxic conditions or when exposed to pharmacological

pseudohypoxia (via PHD inhibitors), AMs can adopt a glycolytic phenotype that improves their survival in the presence of ETC inhibitors. This hypoxic, glycolytic reprogramming is mediated by HIF-1α (111).

Evidence has shown that in a murine model of influenza-induced ARDS, MDMs express high levels of glycolytic and pro-inflammatory genes, alongside with low levels of genes related to OxPhos (107, 110, 111). This expression pattern in MDMs remains relatively consistent throughout the acute phase of infection, while surviving AMs transition from an OxPhos-dominant gene profile to one dominated by glycolysis in a HIF-1α-dependent manner as ARDS progresses (107, 111). These findings indicate that while HIF-1α is not essential for the steady-state function or proinflammatory response of AMs, it plays a crucial role in adapting to hypoxia and promoting survival during ARDS (107, 111).

Infiltrating immune cells further perpetuate the inflammatory environment by consuming oxygen and nutrients, reducing their availability to resident cells. Given that, AMs need to adapt their metabolism from OxPhos to anaerobic glycolysis to maintain effector functions (107).

In comparison, by the time MDMs populate the airway in cases of ARDS/ALI, the original low glucose, high oxygen, and lipid-rich environment of the steady-state lung has already undergone a dramatic transformation. Nutritionally, the inflamed airway more closely resembles the conditions typical of the peripheral blood and bone marrow, from which MDMs originate (107). These conditions, combined with monocytic imprinting, favor a glycolytic phenotype to drive cellular processes during ARDS/ALI (107). In the context of virus-induced ARDS/ALI, it is widely recognized that MDMs exacerbate lung inflammation (107, 112, 113). They are important to limit viral replication and limit secondary bacterial infection during resolution of lung injury (107, 114) but pose an independent risk factor for severe outcome (112, 113). Initially, MDMs may be well-equipped to curb viral replication or prevent secondary bacterial pneumonia during post-viral recovery, but their presence is often linked to excessive inflammation (107).

With regards to species-dependent differences in immunometabolism, human MDMs activated by lipopolysaccharide (LPS) do not undergo a shift towards glycolysis but continue to depend on OxPhos for ATP production. In contrast, LPS activation in murine BMDMs results in a glycolytic reprogramming accompanied by inhibited OxPhos. Moreover, the inhibition of

glycolysis with 2-deoxyglucose (2-DG) results in cell death in murine but not human macrophages (115).

Collectively, these findings highlight that immunometabolism of macrophages differs depending on the species and tissue-specific microenvironment.

Mitochondria at the interface between environment, metabolism, and immunity

Mitochondrial biology

Mitochondria are key organelles integrating extracellular signals and cellular metabolism, to orchestrate biological output that profoundly influences cell fate and viability by regulating programmed cell death, calcium homeostasis, generation of mtROS, as well as inflammation (116, 117).

These energy-producing organelles are enclosed by an inner and outer mitochondrial membrane (IMM or OMM, respectively). According to the endosymbiont theory, approximately 2 billion years ago, a free-living α-proteobacterium was engulfed by an ancestral eukaryotic cell, leading to a symbiotic relationship (118). Over the course of evolution, mitochondria lost the majority of their proteobacterial genetic material and transferred numerous genes to the nuclear genome through a process called endosymbiotic gene transfer (119). Consequently, most components of mitochondria are encoded by the nuclear genome. The small circular mitochondrial genome (mtDNA) primarily encodes the translation machinery and components of the respiratory chain complexes I, III, IV, and V, which are essential for OxPhos. This process is carried out through the coordinated actions of the TCA cycle and the electron transport chain (ETC) (117).

The ETC is a vital part of aerobic respiration that takes place within the IMM of eukaryotic cells. It comprises a series of protein complexes (I, II, III, IV) and electron carriers, such as flavoproteins, cytochromes, and ubiquinone. These components collaboratively facilitate the transfer of electrons, originating from the oxidation of redox molecules like NADH and $FADH_2$, through a sequence of reactions, ultimately passing them to molecular oxygen (O_2), which acts as the final electron acceptor. Energy, released during the flow of electrons through the ETC, allows to pump protons (H+) across the IMM, creating an electrochemical gradient known as the proton motive force (PMF = Δp). Subsequently, the resultant chemiosmotic potential

facilitates ATP synthesis via F_0F_1-ATP synthase (complex V of the ETC) also known as chemiosmosis. Hence, OxPhos involves the ETC and chemiosmosis (120).

Notwithstanding that, mitochondria have long simply been referred to as the "powerhouses of cells." In fact, it is widely understood that cellular function of these organelles extends well beyond just energy production. Mitochondrial processes that regulate cellular function as a result of nutrient availability and environmental cues involve dynamics of mitochondrial morphology, apoptotic and immune signaling, as well as metabolic flexibility (116, 117).

Mitochondrial morphology

Mitochondria are dynamic organelles that can transition between elongated filamentous forms and compact spherical shapes. The counterbalance between the divergent processes of mitochondrial fission and fusion, collectively known as mitochondrial dynamics, defines the overall shape and structure of the dynamic mitochondrial network. Mitochondrial dynamics play a crucial role in mitochondrial quality control, cell division, as well as cellular stress and immune signaling (116, 117, 121).

During health, under homeostatic conditions, mitochondrial dynamics typically demonstrate a more fused, interconnected network of mitochondria. When nutrients are scarce, mitochondria tend to become hyperfused to promote functional cooperation among themselves and to protect the cell. On the other hand, when excessive nutrients or cellular stress signals, including inflammation, predominate, the mitochondrial network becomes hyperfragmented, with fission outweighing fusion (116, 117, 122).

Key proteins that have been identified as regulators of fission and fusion are mitofusins (MFNs) which mediate outer mitochondrial membrane fusion, optic atrophy 1 (OPA1) and mitochondria genome maintenance 1 (MGM1) which facilitate inner mitochondrial membrane fusion, as well as dynamin-related protein 1 (DRP1) and dynamin 1 in close association with the endoplasmic reticulum (ER) which are involved in the division of both outer and inner mitochondrial membranes. Mitochondrial fusion involves the physical merging of the membranes of two separate mitochondria while mitochondrial division is the process of splitting a single organelle into two or more independent entities (116, 117).

Dynamics of mitochondrial morphology regulate cellular quality and function. Any imbalance in mitochondrial fusion and fission dynamics can lead to cellular and tissue dysfunction as has

been implicated in Alzheimer's disease, Parkinson's disease, metabolic dysfunction-associated steatotic liver disease, and cardiac ischemia-reperfusion injury (123).

Mitochondrial immune signaling

Activation of PRRs, such as toll-like receptors, through PAMPs and DAMPs leads to the activation of major immune-regulatory transcription factors, such as activator protein 1 (AP-1) and nuclear factor kappa-light-chain-enhancer of activated B cells (NF-κB), ultimately inducing cytokine and chemokine production (124).

PRRs of the RIG-I like receptor family (RLRs), such as RIG-I and melanoma differentiation-associated gene 5 (MDA-5) are crucial for detecting viral double-stranded RNA. When activated, they trigger the induction of an antiviral immune response. Mitochondria play a key role in this mechanism through the expression of mitochondrial antiviral-signaling protein (MAVS) on the OMM. MAVS recruits tumor necrosis factor receptor (TNFR)-associated factors (TRAF) 2, 5, and 6, thereby promoting NF-κB and IRF-3 activation. This results in an increase in IFNs type 1 and other pro-inflammatory cytokines to enhance antiviral immunity. An intact mitochondrial membrane potential (MMP) and balanced dynamics of mitochondrial morphology are prerequisites for an effective RLR-induced antiviral response (125).

Mitochondria are also involved in TLR7 signaling, with this PRR sensing viral single-stranded RNA and its activation leading to increased pro-inflammatory cytokines and IFNs type 1. The OMM protein E3 ubiquitin-protein ligase MARCH5 is crucial for TLR7-mediated signal transmission by interacting with TRAF family member-associated NF-κB-activator (TANK) and limiting its ability to inhibit TRAF6, thus promoting cytokine induction and immune cell activation. MARCH5 localization to the mitochondrial membrane is essential, as mislocalization impairs its function (117).

While regulating immune signaling in responses to both PAMPs and DAMPs, mitochondria can also drive sterile inflammatory responses through the cytosolic release of DAMPs, such as mtDNA, N-formyl peptides (n-FP), and mitochondrial transcription factor A (TFAM) and initiate apoptosis via cytosolic release of cytochrome c (117, 125, 126).

Conclusively, mitochondria play a fundamental role in innate immunity and apoptosis signaling.

The role of mtROS in immune signaling

Traditionally, mtROS have been linked to cellular damage and toxicity. Nonetheless, physiological levels of mtROS are essential for vital cellular processes, comprising metabolic adaptation, differentiation, proliferation, apoptosis, autophagy, immune signaling, and bacterial killing (127-129).

ROS are oxygen-derived molecules that have the ability to readily oxidize other substances. Within cells, a significant portion of ROS originates from superoxide ($O_2-\cdot$), produced by one electron reduction of molecular oxygen (O_2). Superoxide dismutases (SODs) then convert superoxide into hydrogen peroxide (H_2O_2) which can act as an important cellular signaling molecule (130-132).

Eleven distinct mitochondrial sites involved in substrate oxidation and oxidative phosphorylation have been identified to transfer electrons to molecular oxygen generating superoxide or hydrogen peroxide (132). These are oxoacid dehydrogenase complexes that transfer electrons to NAD^+, ETC complexes I and III, and dehydrogenases that use ubiquinone as acceptor, including ETC complex II. However, only complex III and glycerol 3-phosphate dehydrogenase (G3PDH) produce superoxide that is released to the external side of the mitochondrial membrane and matrix while other sites exclusively generate superoxide or H_2O_2 in the mitochondrial matrix. Especially mtROS produced at complex I, II, and III have been involved in immunological signaling (117). The net release of superoxide or H_2O_2 also depends on the availability of substrates and antioxidant system present (132, 133). Mitochondrial factors that control mtROS production include the local oxygen concentration, redox state of the ETC complexes and MMP (133, 134).

Mitochondria are generally viewed as the primary sources of ROS production. However, a substantial amount of ROS can also be generated in the cytoplasm, cell membrane, or various cellular compartments such as the peroxisomes and endoplasmic reticulum (ER), especially when exposed to different external stimuli, such as pathogens. Cytosolic ROS (cROS) are primarily produced by the nicotinamide adenine dinucleotide phosphate (NADPH) oxidase (NOX) family, which facilitate the transfer of electrons from NADPH to molecular oxygen, resulting in the creation of superoxide and, subsequently, other ROS molecules. In mammals, besides NOX, various isoforms of nitric oxide synthase, including neuronal NOS (nNOS/NOS1), inducible NOS (iNOS/NOS2), and endothelial NOS (eNOS/NOS3), also play a role in the generation of cROS (127, 135).

As has been demonstrated for *S. pneumoniae* and *H. influenzae*, two important bacteria that cause community-acquired pneumonia, AMs eliminate bacteria effectively through a two-phase process. During the initial phagocytosis-associated phase of infection, AMs maintain viability and kill bacteria within their phagolysosomes. This is followed by a later phase in which apoptosis is induced, helping clear the bacteria. In the first phase, the protein myeloid cell leukemia sequence-1 (Mcl-1) ensures mitochondrial stability and helps AMs resist apoptosis. However, AMs have a limited capacity to process bacteria, and in the later phase, a reduction in Mcl-1 expression leads to increased activation of caspase 3/7 and consecutively increased mtROS production. Furthermore, apoptosis-associated bacterial killing requires mtROS for clearance of bacteria *in vivo* with mtROS and nitric oxide (NO) colocalizing with bacteria-containing phagolysosomes (136). Interestingly, upregulation of Mcl-1, as has been found in COPD patients, alters microbicidal function of AMs by inhibiting the delayed phase of apoptosis-associated intracellular bacterial clearance, consecutively increasing susceptibility to bacterial pneumonia (137).

Activation of cytoplasmic TLRs 1, 2, and 4 by PAMPs results in the recruitment of mitochondria to the phagosome in murine macrophages (BMDMs and RAW cells) boosting the production of mtROS. Following the activation of TLRs, the adaptor protein TRAF6 associates with and ubiquitinates ECSIT, an assembly factor of the mitochondrial respiratory chain. Ubiquitination of ECSIT increases mtROS production, thereby enhancing intracellular killing of bacteria (138). Another PRR, the NLRP3 inflammasome, assembled by NLRP3, ASC, and caspase 1, can be activated by divergent stimuli, including ATP, oxidized mtDNA, NETs, or viral ds-RNA. Upon viral ds-RNA detection in an RIG-I and MDA-5-dependent manner, the NLRP3 inflammasome is translocated to mitochondria and mitochondria-associated ER membranes, promoted by MAVS, which aids IL-1β processing and mtROS production (125, 139). Vice versa, following LPS-induced pro-inflammatory reprogramming in murine macrophages (BMDMs and peritoneal macrophages), mtROS are involved in NLRP3 activation through reverse electron transport (RET) at complex I leading to inflammasome-regulated IL-1β secretion (140, 141).

Murine macrophages (BMDMs) that are stimulated with LPS reprogram from producing OxPhos-derived ATP toward utilizing glycolysis, accompanied by an increase in succinate levels. Enhanced mitochondrial oxidation of succinate via succinate dehydrogenase (SDH), along with the rise in MMP, collectively promote reverse electron transport (RET) accompanied by the increased production of mtROS. mtROS-dependent stabilization of HIF-

1α leads to a pro-inflammatory gene expression profile including IL-1β. Conversely, using dimethyl malonate (DMM) to inhibit succinate oxidation encourages an anti-inflammatory response including IL-10 (88). SDH-mediated RET has subsequently been shown to be important for mtROS production in tuberculosis (TB)-infected macrophages, in inflamed microglial cells, and in chondrocyte activation in a model of arthritis (104).

However, recent evidence also highlighted an mtROS-independent activation of the NLRP3 inflammasome. Instead, the mitochondrial ETC sustains NLRP3 inflammasome activation through phosphocreatine (PCr)-dependent generation of ATP mediated by creatine kinase (CK) (142).

Mitochondrial reprograming in inflammatory macrophages has also been associated with inducible nitric oxide specis (iNOS), which catalyzes the conversion of L-arginine to L-citrulline and NO. NO decreases protein levels of ETC complexes I, II, III, and IV and diminishes activity of complexes I, II, and IV in murine macrophages (BMDMs) that are co-stimulated with LPS and IFN-γ (120, 143, 144).

Mechanistically, the synthesis of cardiolipin (CL), a mitochondrial phospholipid, by CL synthase (CRLS1), plays an essential role in driving inflammatory responses, particularly the production of IL-6, IL-1α, pro–IL-1β, and iNOS. Subsequently, iNOS produced NO induces the disassembly of complex II by causing the dissociation of succinate dehydrogenase (A) (SDH(A)). This inhibition pathway of complex II contributes to the acute inflammatory response. The remaining components of complex II, SDH(B), SDH(C), and SDH(D), are sequestered in a CL-dependent manner and released from the mitochondrial network via DRP1-dependent mitochondrial fission to be degraded through selective mitophagy (144).

The importance of mitochondria for macrophage plasticity is further emphasized by the production of NO in pro-inflammatory activated BMDMs, which inhibits the reprogramming towards IL-4-dependent alternatively activated macrophages to sustain an inflammatory response in BMDMs (145).

Vice versa, the important anti-inflammatory cytokine IL-10 promotes mitochondrial respiration by increasing arginase 2 (Arg2) levels which enhance activity of ETC complex II (SDH). This results in decreased levels of succinate, HIF-1α and IL-1β in response to LPS-induced acute inflammation in murine macrophages (BMDMs and RAW cells). These findings shed light on IL-10-mediated metabolic regulation promoting resolution of inflammation (146).

Mitochondrial Ucp2 which is abundantly expressed in monocytes and macrophages throughout tissues (147) has been implicated in mtROS production and bacterial killing. When mice deficient in Ucp2 were challenged with the intracellular pathogen *Toxoplasma gondii* (*T. gondii*), they showed significantly improved survival and decreased brain cyst formation compared to wild type animals. Additionally, knockout animals exhibited increased toxoplasmacidal activity, bactericidal properties against intracellular *Salmonella enterica* ssp. *enterica* serovar *Typhimurium*, and *T. gondii*-provoked mtROS levels (148). Similarly, *Ucp2*$^{-/-}$ mice are more resistant to *Listeria monocytogenes* displaying increased splenic ROS levels (149).

After murine macrophages (RAW cells and BMDMs) engulf *S. aureus*, mtROS are converted into mt-derived H_2O_2 by manganese superoxide dismutase (Mn-SOD). In order to transport mt-derived H_2O_2 to the bacteria-containing phagolysosome, mitochondrial-derived vacuoles (MDVs) are released to facilitate intracellular microbial killing. These MDVs, carrying mt-derived H_2O_2, are prompted by TLR-signaling and the mitochondrial stress pathway dependent on Parkin and Pink1 (150). In contrast, *S. aureus* can promote its survival within macrophages facilitated by caspase-11, which limits mitochondrial recruitment to the bacteria-containing vacuole. In the absence of caspase-11, the association of mitochondria with the vacuoles containing bacteria increases, leading to enhanced mtROS production in murine macrophages (BMDMs). Furthermore, in BMDMs lacking caspase-11, treatment with antimycin-A heightened mtROS production, resulting in enhanced bactericidal properties (151).

In terms of cytokine production, it was shown that LPS via TLR4 and tumor necrosis factor-α (TNF-α) through TNF receptor-associated factors (TRAFs) trigger inflammatory cytokines by generating mtROS (129, 152). For example, signaling pathways mediated by TRAF2 alters the redox status of the cell promoting the production of mtROS to enhance NF-κB activation independent of NF-κB-inducing kinase (NIK, MAP3K14). Interestingly, Bcl-xL interfered with TRAF-mediated mtROS generation to inhibit apoptosis but not NF-κB activation (152).

In addition to immune signaling, mtROS production is enhanced during hypoxia and in response to increased intracellular calcium, e.g., during vasoconstriction of pulmonary vascular smooth muscle cells (129, 130, 153, 154). Hypoxic conditions prompt mitochondria to produce mtROS at complex III contributing to the stabilization of HIFs, which subsequently

trigger the expression of genes that enable metabolic adaptation to reduced oxygen levels (153, 154).

Therefore, within a physiological range, mtROS play an important role in cellular signaling as an adaptation to inflammation and stress (Fig. 2).

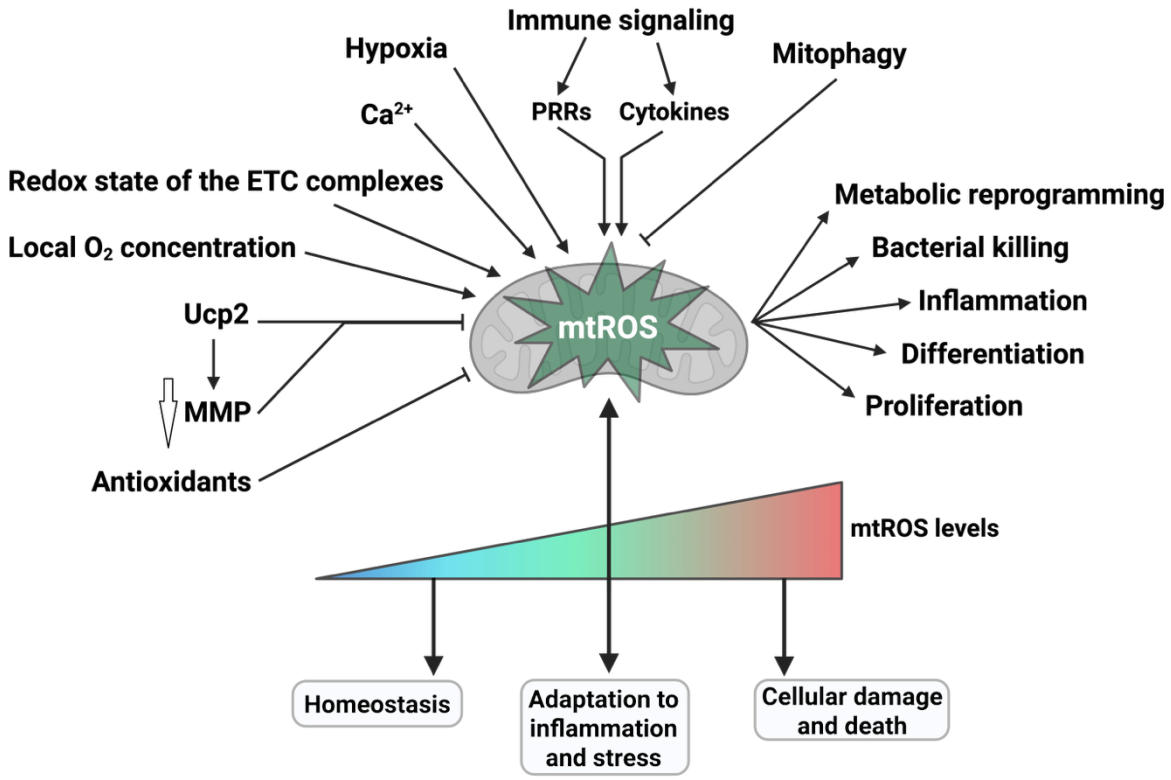

Figure 2. The role of mtROS in immunity

Depending on the extent of the cellular stressor, mtROS are produced from a low up to a high concentration. These levels contribute to a range of cellular processes ranging from homeostasis up to cellular death. But within a medium physiological level, mtROS are needed to adapt to inflammation and stress. mtROS are regulated the MMP, proteins like Ucp2, the local oxygen concentration and redox state of the ETC complexes. Furthermore, calcium, hypoxia, mitophagy, and immune signaling including response to PRRs and cytokines influence mtROS production. Consequently, mtROS influence crucial cellular processes, such as metabolic reprogramming and adaptation, bacterial killing, inflammation, differentiation, and proliferation.

*Created with BioRender.com; based on Sies H, Belousov VV, Chandel NS, et al., 2022 (129) and Sena LA, Chandel NS, 2012 (130).

Resolution of inflammation and tissue repair

The role of macrophages in resolution and repair following acute lung injury

As ALI/ARDS is characterized by damage of the alveolar-capillary barrier, resolution requires its repair to restore tissue function. The molecular events that coordinate the shifting roles of different macrophage populations throughout the processes of ALI and its resolution, is a process we are just beginning to understand in greater detail (50, 155).

In response to a growing array of microenvironmental signals emanating from the regenerating lung tissue MDMs gradually differentiate toward an AM-like phenotype. MDM may acquire the ability to self-renew and remain in the tissue after healing, potentially through downregulation of the transcription factor MAFB and upregulation of molecules that interact with epithelial cells to facilitate the return to tissue homeostasis, such as the receptor/ligand pairs CD200R/CD200, signal regulatory protein-α (SIRPα)/CD47, and CSF2R/GM-CSF, along with immune/epithelial E-cadherin interactions. Alternatively, these macrophages might undergo apoptosis, enabling the restoration of tissue-resident AMs through proliferation and migration, as demonstrated in microglia (50, 156).

In addition, reprogramming of macrophages in response to unique factors present in the injured tissue microenvironment enables them to actively promote resolution and repair. This might be mediated by regulatory T-cells (Tregs) that expand and release factors like amphiregulin, TGF-β, and IL-10, or engage with macrophages through ligand/receptor interactions such as CD40/CD80. Additionally, microvesicles from macrophages or other recovering cell populations may contain signaling molecules such as SOCS2 or microRNAs, which promote reparative phenotypes in macrophages. In return, pro-resolutory reprogrammed macrophages release pro-resolutory substances, including anti-inflammatory agents like IL-10 and TGF-β, growth factors (GFs) that aid in proliferation of AECs, such as platelet-derived growth factor (PDGF), insulin-like growth factor 1 (IGF-1), fibroblast growth factor (FGF). Furthermore, macrophages can secrete factors that promote angiogenesis such as vascular endothelial growth factor (VEGF), PDGF, epiregulin, and amphiregulin, as well as matrix metalloproteinases (MMP-8, -10, and -28), and osteopontin (50, 156-158).

TNF-α released from recruited MDMs can drive AECs to produce GM-CSF, subsequently inducing epithelial proliferation in an autocrine manner. Therefore, inflammatory signaling initiates repair of the epithelial unit, crucial for alveolar restoration (159).

Recent data has highlighted oncostatin M (OSM), a pleiotropic cytokine of the IL-6 family, as a crucial macrophage-derived growth factor that supports AEC proliferation and homeostasis, helping to counteract the immunopathology and tissue injury caused by IFNs type 1 in response to influenza virus pneumonia. When challenged with influenza or a viral mimic, OSM-deficient mice had elevated IFN type 1 responses and higher mortality rates. Administering OSM to the lungs stimulated AEC type II proliferation and was sufficient to protect deficient mice from disease severity. Additionally, OSM encouraged organoid development even in the presence of the growth-suppressing effects of IFNs type 1 (160). Interestingly, GM-CSF, a growth factor and AEC type 2-derived signal indispensable for AM maintenance, was essential for OSM production (36, 160).

Macrophage-derived placenta-expressed transcript 1 (Plet1), produced by MDM-derived macrophages at later stages of the inflammatory process, has been involved in lung tissue repair following severe influenza A virus pneumonia, where Plet1 stimulates the proliferation of epithelial progenitor cells including AECs type II, reconstituting a functional macrophage-epithelial alveolar unit. The expression of Plet1 in MDMs promotes a transition to a pro-repair and homeostatic AM phenotype (55).

Furthermore, resolution and repair of ALI critically depends on the elimination of accrued apoptotic cells (ACs), mainly PMNs and AECs, by lung macrophages, a process termed efferocytosis (161, 162).

The basic concept of efferocytosis

Daily, 200 to 300 billion cells are turned over in the human body, primarily through caspase-dependent apoptosis. For instance, neutrophils, key innate immune cells that defend against invading pathogens, have a short lifespan, with over 100 billion being replaced every day. In the thymus and bone marrow, millions of immature T and B lymphocytes are produced, but only a few mature while the rest are eliminated by apoptosis. During embryogenesis and organ development, apoptosis helps restructure tissues, and aged red blood cells are regularly cleared as part of the body's maintenance. During the resolution of inflammation, immune cells like neutrophils, monocytes, and lymphocytes undergo apoptosis after fulfilling their roles. Still, ACs are rarely detected in tissues because they are removed by phagocytes in a highly specialized process termed “efferocytosis” (163, 164).

Mostly, efferocytosis is managed by tissue-resident professional phagocytes, termed efferocytes, such as macrophages and DCs, but non-professional efferocytes like epithelial cells and fibroblasts can also contribute to the clearance of ACs. In certain tissues, specialized efferocytes like retinal pigmented epithelial cells in the eyes and Sertoli cells in the testes are responsible for clearing ACs (163, 164).

Even though mechanistically similar to the clearance of pathogens, efferocytosis is an immunologically silent process inducing a tissue-repair response, e.g., by release of IL-10 and TGF-β. Opposingly, clearance of pathogens, like Fc receptor-mediated phagocytosis, is designed to initiate a pro-inflammatory immune response (163, 164). Indirectly, efferocytosis inhibits sustained inflammation by preventing ACs from becoming necrotic and releasing pro-inflammatory content (163, 164). Therefore, a failure to efficiently clear apoptotic cells can contribute to non-resolving chronic inflammatory diseases, including atherosclerosis, age-related inflammation, cancer, and infections (78).

Moreover, efferocytosis is crucial not only for tissue homeostasis, but also embryonic development, wound healing, and the resolution of inflammation (163, 164).

Molecular machinery of efferocytosis

The clearance of apoptotic cells typically occurs in four stages. The first stage involves recruitment of the efferocytes. If ACs are not in close proximity, they recruit efferocytes by emitting chemoattractants known as “find-me signals” (165).

In the second stage, phagocytes physically recognize nearby ACs. This recognition involves interactions between ligands on apoptotic cells, referred to as “eat-me signals,” and corresponding receptors expressed on phagocytes. This crucial step allows phagocytes to identify which cells to engulf. The most well-known ligand presented on apoptotic cells is phosphatidylserine (PtdSer), which is detected by various receptors on phagocytes either directly or indirectly (165). PtdSer is directly identified by several receptors, such as BAI1 (also called ADGRB1), TIMD4, CD300LF, STAB1, and STAB2. Additionally, exposed PtdSer can be indirectly recognized by TAM (TYRO3, AXL, and MERTK) receptor tyrosine kinases and MEGF10 through their respective soluble ligands, GAS6 and PROS1 or C1q, respectively (166).

During the third step ACs are being internalized by efferocytes. Ligand-receptor interactions activate distinct signaling pathways beyond engulfment receptors, triggering cytoskeletal

rearrangements necessary to process large targets and traffic apoptotic cargo intracellularly (165).

Finally, the phagosomes containing ACs merge with lysosomes to form phagolysosomes, where the cells are broken down by a variety of lysosome-derived digestive enzymes (80).

Hence, while the molecular machinery of efferocytosis has been well described less is known about the effector responses to cell death (167).

Effector responses following efferocytosis

Cell death triggers a wide range of effector responses, encompassing various immune defense mechanisms, specific functions for maintaining tissues, and developmental roles such as the formation of digits and neuronal circuits. Surprisingly, the intricate and multidimensional information that leads to such a diverse set of effector responses is encoded within the process of cell death. Non-inflammatory cell death typically leads to homeostatic and developmental adaptations, while inflammatory cell death is associated with injury and infection control, as well as inflammation resolution and repair (167).

The same mode of cell death can lead to various temporally and spatially distinct effector functions, influenced by the tissue-specific environment and efferocytes involved. The tissue environment shapes the effector response of the efferocyte in several ways. Either directly through a cytokine milieu unique to that environment, through epigenetic or transcriptional imprinting, or through distinct metabolic functions tied to that environment (167).

Oxylipins, specifically prostaglandin E2 (PGE2), and other metabolites released by pyroptotic cells, a lytic type of cell death, have been found to actively promote tissue repair by alteration of gene expression in macrophages to enhance wound healing (168).

Macrophages are believed to be the primary source of lipid mediators termed “specialized pro-resolving mediators” (SPM), such as resolvins, protectins, and maresins, which are derived from polyunsaturated fatty acids and have been shown to facilitate resolution of tissue damage across various conditions (50, 155, 156). When macrophages are incubated with apoptotic neutrophils or neutrophil microparticles, they increase the expression of the SPMs lipoxin A4 and resolvins D1, D2, and E2, while simultaneously decreasing the expression of pro-inflammatory prostaglandins and leukotriene B4. Lipoxin A4 and resolvin D1 further enhance efferocytosis, creating a feedback loop that boosts their own production (169).

Additionally, efferocytosis upregulates the expression of 12/15-lipoxygenase, a key enzyme involved in SPM biosynthesis (170, 171).

Importantly, clearance of ACs by macrophages leads to inhibition of pro-inflammatory cytokine secretion while releasing anti-inflammatory cytokines, specifically IL-10 (172-175). In this way, clearance of ACs elicits a pro-resolutory phenotype in efferocytes.

Continual efferocytosis

The capability of efferocytes to continuously clear ACs is essential, given the fact that ACs frequently outnumber macrophages in inflamed regions, indicating a high apoptotic cell to efferocyte-ratio (AC:EC-ratio) (176).

Continual efferocytosis poses the challenges to firstly rapidly restore the cell surface area as a substantial amount of plasma membrane is internalized during each AC uptake and secondly degrade large amounts of AC cargo, including fatty-, amino-, and nucleic acids (177, 178).

While phagocytes consume apoptotic cargo, the MMP increases. To counterbalance excessive MMP levels, the phagocyte upregulates Ucp2 which decreases the MMP during efferocytic processing. Conclusively, silencing of Ucp2 leads to sustained high MMP levels following corpse ingestion. This Ucp2-dependent mechanism proves a necessity to prime the efferocyte for continued efferocytosis (177).

Besides changes in MMP, mitochondria also undergo mitochondrial fission soon after interacting with an AC, resulting in cytosolic calcium release to promote vesicular trafficking and phagosome sealing. Therefore, mitochondrial fission promotes continued clearance of ACs (178).

Macrophages that engulf ACs engage in mitochondrial FAO to fuel the ETC facilitating the production of nicotinamide adenine dinucleotide (NAD^+). This leads to enhanced sirtuin-dependent activation of Pre-B-cell leukemia transcription factor 1 (PBX1), which acts as a transcription factor for the pro-resolving cytokine IL-10 promoting resolution and repair *in vivo* (174).

Efferocytosis also relies on glutaminase 1 (GLS1)-mediated glutaminolysis, which occurs via non-canonical glutamine transamination in diverse macrophages. In more detail, reparative macrophages combat oxidative stress through a unique glutamine transamination pathway. This process supports OxPhos, meeting the high-energy demands of cytoskeletal rearrangements during continued efferocytosis. Glutamine also serves as a precursor for

nicotinamide adenine dinucleotide phosphate ($NADP^+$/NADPH) and the antioxidant glutathione, which helps neutralize ROS produced by the highly oxidative efferocytic macrophage. In addition, mice lacking macrophage Gls1 exhibited impaired efferocytosis both *in vivo* and *in vitro*, under reparative conditions or after repeated exposure to dying cells. The clinical and pathological significance of glutaminolysis in this process was demonstrated by its inverse association with the accumulation of necrotic core in both human and murine atherosclerotic lesions (179).

Moreover, tryptophan proves important for continual efferocytosis involving production of the tryptophan metabolite kynurenine regulated through indoleamine 2,3-dioxygenase-1 (IDO1), which then activates the aryl hydrocarbon receptor (AhR). Through these pathways, macrophage IDO1 and AhR play integral roles in promoting secretion of anti-inflammatory mediators, such as IL-10, and enhancement of continued efferocytosis. This translates into a proper resolution and repair response in different mouse models, especially the regression of atherosclerosis induced by lowering plasma low-density lipoprotein (LDL) (175).

Recent evidence has highlighted the importance of glycolysis for efferocytic reprogramming of macrophages towards an anti-inflammatory and pro-resolving phenotype. Transcriptomic profile of phagocytes engulfing ACs revealed upregulation of 33 members of the solute carrier (SLC) family of membrane transporters, with two specifically critical for glycolysis. The AC to phagocyte interaction upregulated SLC2A1 which encodes the glucose transporter 1 (GLUT1). Meanwhile, secretory factors released by ACs increased the level of serum and glucocorticoid-regulated kinase 1 (Sgk1), a kinase that helps relocate GLUT1 to the cell surface. This increased expression of SLC2A1 and Sgk1 led to enhanced glucose uptake and activation of aerobic glycolysis. The engagement in glycolysis proved to be essential for continued efferocytosis through induction of actin polymerization necessary for cytoskeletal rearrangement. At a later stage in efferocytosis, the internalization of an AC increased the expression of SLC16A1 (encodes monocarboxylate transporter 1 (MCT1)), which facilitated the release of lactate. Lactate acts in a paracrine manner, prompting nearby cells to produce IL-10 and TGF-β. Thus, glycolysis driven by SLC2A1 leads to dynamic actin remodeling, enabling the continuous clearance of ACs, and subsequent lactate release mediated through SLC16A1 contributes to the resolution program observed after efferocytosis (180).

Sterols released within efferocytes after degradation of ACs in the phagolysosome activate nuclear sterol receptors like PPARγ, PPARδ, and liver X receptor-α (LXRα). These receptors then

promote the production of anti-inflammatory and pro-tolerogenic cytokines, such as IL-10 and TGF-β, differentiation of Tregs and T helper 2 (Th2)-cells, further promoting the resolution inflammation, as well as enhancement of continual efferocytosis (181-183).

Under physiological hypoxia, macrophages efficiently flux glucose into a noncanonical PPP loop to enhance NADPH production. PPP-derived NADPH directly supports continual efferocytosis by ensuring phagolysosomal maturation and redox homeostasis (184).

The role of efferocytosis in disease pathophysiology

Apoptotic neutrophils serve as a plentiful source for efferocytosis during inflammation. In an experimental model of myocardial infarction, the rapid depletion of neutrophils leads to increased fibrosis, accumulation of ACs within the infarcts, and worsened cardiac function. Neutrophils crucially promote polarization of cardiac macrophages toward an IL-10/TGF-β-producing reparative phenotype with increased expression of the efferocytosis receptors AXL/MERTK. This phenotype proves critical to the clearance of dying cardiomyocytes and has been reproduced *in vitro* through incubation of macrophages with neutrophil gelatinase-associated lipocalin (NGAL) (185).

In myeloid cells, the deletion of Arg1, which encodes arginase 1, reduces synthesis of putrescine. This prevents downregulation of the pro-inflammatory cytokines TNFα and IL-1β, reduces efferocytic capacity, decreases thickening of the fibrous caps of atheromatous plaques, and hinders atherosclerosis regression (186).

Diabetes and obesity demonstrate defective efferocytosis predisposing to impaired inflammation resolution, such as wound healing and atherosclerosis (109, 110, 187).

Loss of MERTK expression mediated by protease disintegrin and metalloproteinase domain-containing protein 17 (ADAM17) in macrophages has been highlighted as a mechanistic explanation of impaired efferocytosis in obesity (188, 189).

Efferocytosis has also been implicated contributing to recovery from intracerebral hemorrhage (ICH) through AXL/MERTK-dependent clearance of eryptotic erythrocytes by MDMs (190).

ARDS is characterized by overexuberant and dysregulated inflammatory responses. Therefore, resolution of ALI/ARDS critically depends on pro-resolution functions of AMs, such as the clearance of apoptotic cells, while defective efferocytosis of AMs is associated with worse outcome during ARDS (161, 162, 191, 192).

In summary, the diverse roles of macrophages in resolution of inflammation and repair include reduction of pro-inflammation, anti-inflammatory and pro-repair signaling, efferocytosis, and the interplay with epithelium and Tregs (155, Fig. 3).

These macrophage hallmark functions to promote resolution and repair critically depend on mitochondrial-directed immunometabolic reprogramming (Fig. 3).

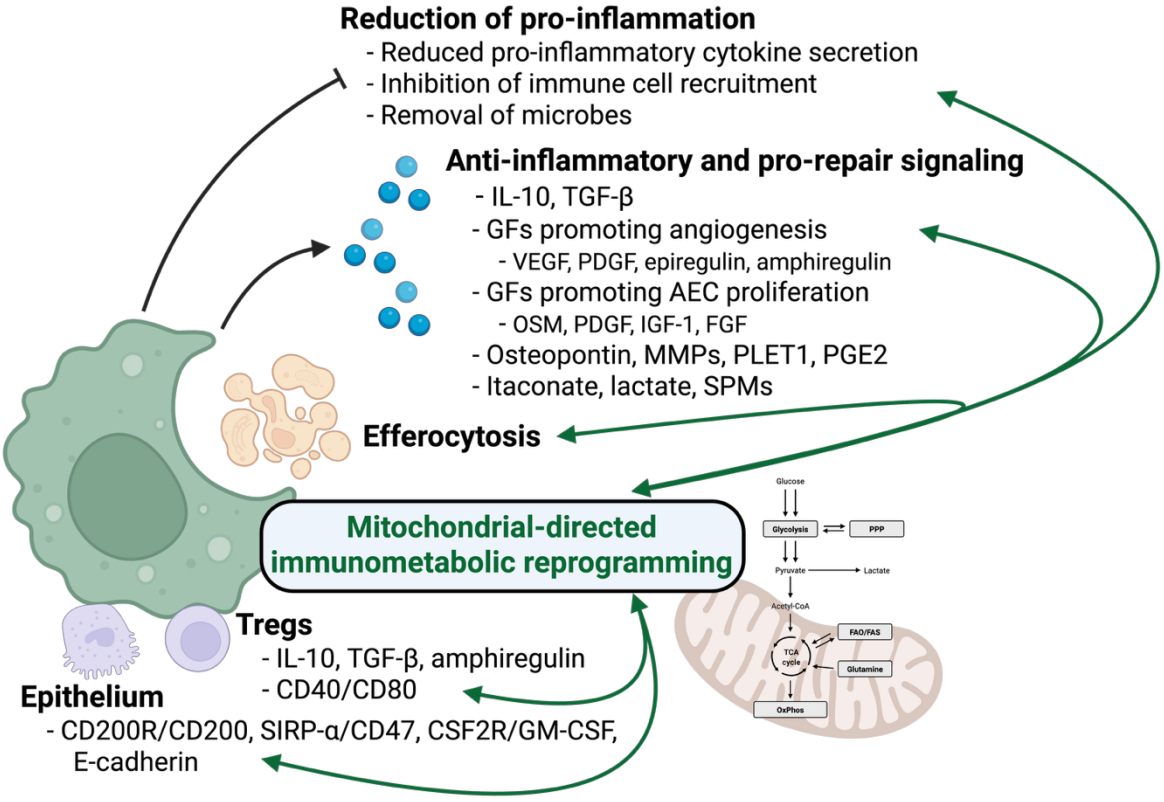

Figure 3. The role of macrophages in resolution of inflammation and repair

Hallmark characteristics of pro-resolving macrophages include reduction of pro-inflammation, anti-inflammatory and pro-repair signaling, efferocytosis, and interplay with the epithelium and Tregs. Engagement in all of these processes induces mitochondrial-directed immunometabolic reprogramming which, in turn, moderates these pro-resolutory tasks to enhance resolution of inflammation and repair.

*Created with BioRender.com; based on Rodríguez-Morales P, Franklin RA, 2023 (155).

Resolution of inflammation and the risk of secondary bacterial infection

Recent findings challenge the traditional view that resolving inflammation simply restores tissue to homeostasis, observing instead another wave of leukocyte infiltration into tissues

suggesting a prolonged phase of immune activity, which shapes subsequent bacterial infections (193-203).

How subsequent bacterial infections are shaped seems to depend on the type and severity of the experimental model applied, as well as the specific cell types investigated (193-203). Following mild, and self-limiting bacterial respiratory infection with *S. pneumoniae*, long-lasting remodeling of the AM population confers enhanced lung protection against subsequent bacterial infections (194, 195). Consistently, one month after recovering from influenza, mice show enhanced protection against *S. pneumoniae* due to a specific population of recruited monocyte-derived macrophages (MDMs) that produce elevated levels of interleukin-6. These influenza-induced MDMs have surface characteristics similar to tissue-resident AMs but possess distinctive functional, transcriptional, and epigenetic profiles (196). In contrast, shortly after *S. pneumoniae*-induced lung inflammation resolves, there is a notable influx of antigen-specific lymphocytes with memory and tissue-resident profiles, alongside macrophages with alveolar or interstitial characteristics. Transcriptomic analysis of these macrophages indicates an upregulation of genes involved in prostaglandin biosynthesis and T-cell chemotaxis and differentiation (197, 198).

In addition, following the resolution of ALI, murine AMs showed reduced phagocytic ability for several weeks (199, 200). This impaired state resulted from tissue-resident AMs undergoing an epigenetic shift toward tolerogenic training. Signal-regulatory protein α (SIRPα) was crucial in creating the microenvironment necessary for this tolerogenic training. In humans experiencing systemic inflammation, both AMs and circulating monocytes exhibited changes indicative of reprogramming even six months after the inflammation had subsided (199).

Efferocytosis, a hallmark feature of inflammation resolution, has also been strongly implicated in increasing susceptibility to secondary bacterial pneumonia (201). Mechanistically, efferocytosis-induced upregulation of PGE2 impairs phagocytic capacity of AMs (202).

Interestingly, primary viral lung injury can also increase the risk for secondary bacterial pneumonia by impairing AM's ability to conceal bacteria from the immune system. Macrophages detect, move towards, and efficiently engulf inhaled bacterial pathogens like *P. aeruginosa* and *S. aureus* by patrolling through the pores of Kohn, effectively concealing these bacteria from neutrophils. When AM's chemotaxis towards bacteria was disrupted, it resulted in excessive recruitment of neutrophils, causing undue inflammation and tissue damage. In

the context of disease, infection with influenza A virus hindered AM movement through the type 2 IFN signaling pathway, significantly increasing the risk of secondary bacterial co-infections of the lung (203).

In conclusion, the advantages of improved inflammation resolution might promote a weakened ability to combat bacterial pathogens, potentially shifting the balance from effective bacterial control to invasive infection (Fig.3.).

Ultimately, gaining insight into how the plasticity of AMs is shaped *in vivo* could pave the way for developing innovative macrophage-based therapies for ALI/ARDS. Therapeutically applied macrophages could resolve lung inflammation while maintaining their ability to defend against invading bacteria (204).

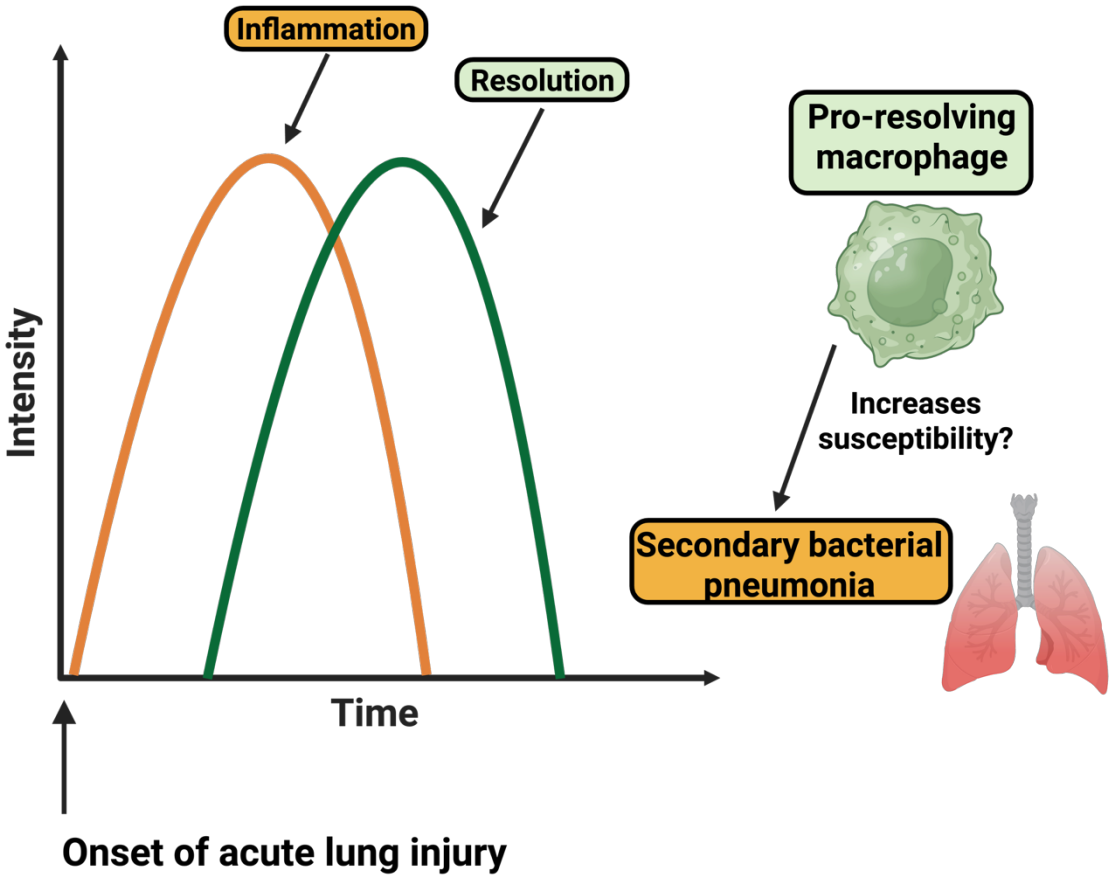

Figure 4. Resolution of ALI and the risk of secondary bacterial pneumonia

ALI-induced inflammation triggers its resolution. Pro-resolving AMs orchestrate resolution and repair to restore organ function. However, this pro-resolutory phenotype might compromise bactericidal properties and therefore increase susceptibility to secondary bacterial pneumonia.

*Created with BioRender.com; based on Rodríguez-Morales P, Franklin RA, 2023 (155).

Aims of this work

Secondary bacterial pneumonia is of major clinical importance associated with high morbidity and mortality (1-3). While respiratory viruses are leading causes of secondary bacterial pneumonia in a community-acquired setting (10-16), pulmonary aspiration of gastric content is one of the strongest independent risk factors for ventilator-associated pneumonia referring to an intensive care environment (21, 22). Alveolar macrophages are the most abundant immune cell type in the distal lung parenchyma and the first line of defense against invading pathogens. Therefore, AMs help orchestrate the initiation of inflammation but, seemingly contradictory, also promote resolution and repair (205). Thus, exploring microenvironmental cues that govern AM plasticity towards antibacterial and pro-resolving functions *in vivo* is of clinical importance but remains incompletely understood. We observed earlier that acid aspiration leads to uncontrolled bacterial outgrowth during secondary bacterial pneumonia (200). In this ALI model, administration of an anti-inflammatory compound restored bacterial control by AMs. Thus, inflammation or the resolution thereof affects antibacterial properties of AMs, but the mechanism and implications of this functional alteration remain unclear. Here, we set out to identify local environmental cues that determine the transcriptomic, immunometabolic, and functional phenotype of AMs during inflammation and resolution *in vivo* influencing the outcome during subsequent secondary bacterial infection. Ultimately, we aimed to infer putative therapeutic targets to improve the outcome of secondary bacterial pneumonia after resolution of ALI.

Results

AMs exhibit impaired bactericidal properties during resolution of sterile pneumonitis

To examine the functional responses of AMs during the course of ALI, we utilized a translational mouse model of pulmonary acid aspiration (200). This self-resolving model effectively replicates key features of ALI, such as PMN influx, pulmonary edema, and tissue injury (3, 206). The predominant macrophage population in this model comprises AMs, as there's only a minimal and protracted contribution from recruited inflammatory MDMs, which peak at low levels 96 hours post aspiration (gating strategy Fig. 5A; Fig. 5B). PMN influx reaches its maximum approximately 12 hours following hydrochloric acid (HCl) instillation and subsequently resolves (gating strategy Fig. 5A; Fig. 5C). To explore alterations in function over time, we administered HCl intratracheally (i.t.) at various intervals, from 12 hours to 8 days. Following ALI, we either secondarily infected mice with *P. aeruginosa* (PA) *in vivo* or harvested AMs for further analyses *ex vivo* (Fig. 5D). Bacterial burden *in vivo* was assessed at an early phase of secondary bacterial pneumonia (3 hours), immediately before de-novo PMN recruitment in sham treated animals, while a more rapid PMN influx was observed in animals 24 hours post acid aspiration (Fig. 5E). Despite the rapid PMN recruitment, bacterial outgrowth in bronchoalveolar lavage fluid (BALF) was greatest in mice that received acid 24 hours prior (Fig. 5F). At this stage, acid-induced pneumonitis is resolving, as indicated by a sharp decline in PMN numbers and pro-inflammatory cytokines (Fig. 5C; 21). To determine whether *in vivo* susceptibility to secondary bacterial pneumonia during inflammation resolution corresponds with AM function, we isolated AMs at the same intervals as *in vivo* experiments and evaluated their ability to clear bacteria *ex vivo*. As AMs are depleted during the course of inflammation (Fig. 5B), we normalized AM numbers for *ex vivo* experiments. Consistent with *in vivo* findings, AMs collected 24 hours after acid aspiration exhibited the greatest impairment in bacterial killing *ex vivo* (Fig. 5G).

Thus, our study suggests that depleted numbers and impaired function of AMs 24 hours post acid aspiration contribute to increased susceptibility to secondary bacterial pneumonia.

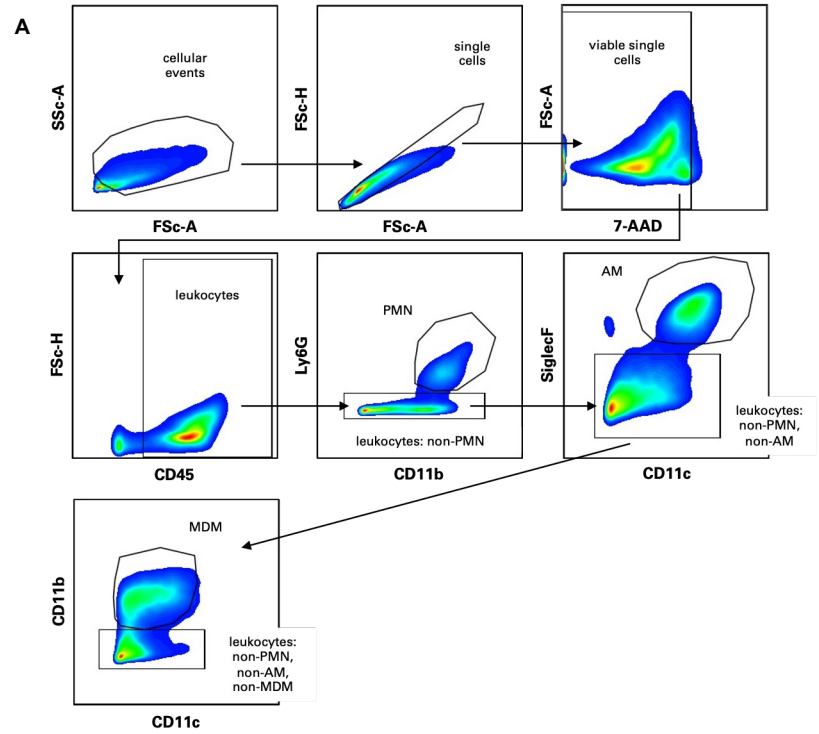
A
cellular events
SSc-A
FSc-A
single cells
FSc-H
FSc-A
viable single cells
FSc-A
7-AAD
leukocytes
FSc-H
CD45
PMN
Ly6G
leukocytes: non-PMN
CD11b
AM
SiglecF
leukocytes: non-PMN, non-AM
CD11c
MDM
CD11b
leukocytes: non-PMN, non-AM, non-MDM
CD11c

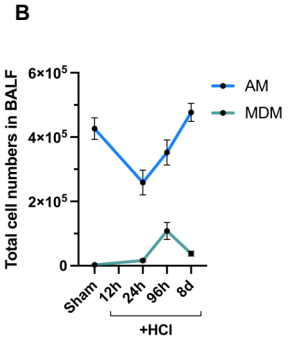
B
Total cell numbers in BALF
6×10^5
4×10^5
2×10^5
0
AM
MDM
Sham
12h
24h
96h
8d
+HCl

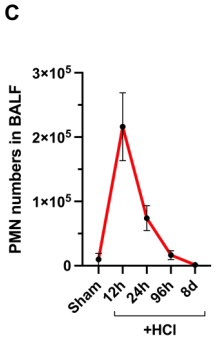
C
PMN numbers in BALF
3×10^5
2×10^5
1×10^5
0
Sham
12h
24h
96h
8d
+HCl

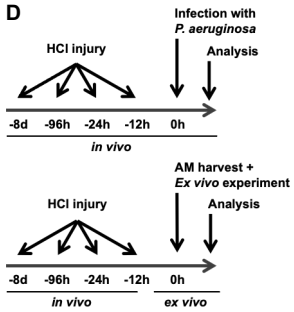
D
HCl injury
Infection with P. aeruginosa
Analysis
-8d
-96h
-24h
-12h
0h
in vivo
AM harvest + Ex vivo experiment
HCl injury
Analysis
-8d
-96h
-24h
-12h
0h
in vivo
ex vivo

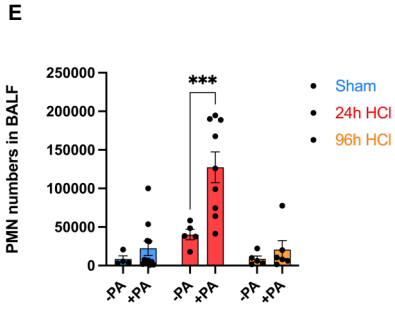
E
PMN numbers in BALF
250000
200000
150000
100000
50000
0
***
-PA
+PA
-PA
+PA
-PA
+PA
Sham
24h HCl
96h HCl

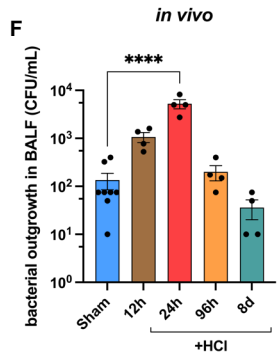
F
in vivo
bacterial outgrowth in BALF (CFU/mL)
****
10^4
10^3
10^2
10^1
10^0
Sham
12h
24h
96h
8d
+HCl

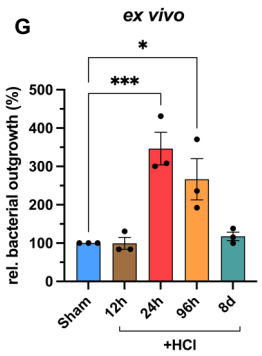
G
ex vivo
rel. bacterial outgrowth (%)
*
***
500
400
300
200
100
0
Sham
12h
24h
96h
8d
+HCl

Figure 5. Functional characteristics of AMs during acid aspiration and subsequent bacterial infection

(**A**) Gating strategy to identify AMs, MDMs, and PMNs.

(**B**) Numbers of AMs and MDMs in BALF over time during acid aspiration (n=7 or 8 mice per group, pooled from two or three independent experiments).

(**C**) Numbers of PMNs in BALF over time during acid aspiration (n=5 to 8 mice per group, pooled from two or three independent experiments).

(**D**) Experimental design for *in vivo* and *ex vivo* studies shown in panels (E) and (F). *Created with BioRender.com

(**E**) PMN numbers in BALF after acid aspiration (Sham versus 24-96h HCl) +/- PA (3h) in vivo (n=5-9 mice/group, pooled from two independent experiments).

(**F**) Bacterial load in BALF after various durations of acid aspiration followed by infection with Pseudomonas aeruginosa (PA) for 3 hours *in vivo* (n=4 mice per group, pooled from two independent experiments).

(**G**) Bacterial killing capacity (PA) of AMs after different durations of acid aspiration *ex vivo* (n=3 replicates per group, pooled from three to five mice per group, representative of two or three independent experiments).

*$P < 0.05$, **$P < 0.01$, ***$P < 0.001$, ****$P < 0.0001$* by one-way ANOVA with Dunnett's multiple comparisons test (**F** and **G**) or two-way ANOVA with Šídák's multiple comparisons test (**E**). Data are shown as the means ± SEM.

AMs boost mitochondrial respiration during resolution of sterile pneumonitis

We then conducted a transcriptome analysis on flow-sorted AMs post acid aspiration with and without secondary bacterial pneumonia, applying the same *in vivo* experimental setup (Fig. 5D). Notably, the most significantly altered pathways in the Kyoto Encyclopedia of Genes and Genomes (KEGG) analysis across all group comparisons were “metabolic pathways” (negative log*P*=38.71) followed by “OxPhos” (negative log*P*=14.5), particularly evident between AMs in mice aspirating acid 24 hours before secondary bacterial infection and those in mice that were solely infected with bacteria (Fig. 6, A and B). The pathways most significantly affected 24 hours after acid aspiration in response to bacteria indicate substantial metabolic reprogramming, increased cell cycle and proteasome transcripts, and reduced immune responses (Fig. 6C). This was evidenced by an analysis of key pro-inflammatory marker genes such as Tnf, Il6, Il1b, Cxcl2, and Toll-like receptors (Tlrs), which showed an attenuated response to bacteria in AMs 24 hours after acid aspiration (Fig. 6D). This pattern was similarly reflected in KEGG-pathway analysis of NF-κB, TNF, and mitogen-activated protein (MAP)-kinase signaling (Fig. 6, E and F). At later stages post acid instillation, a resurgence of pro-inflammatory response was observed (Fig. 6D).

Hence, transcription analysis of AMs implies reduced responsiveness to bacterial challenge 24 hours post acid aspiration while OxPhos is upregulated.

To examine if transcriptional changes translate into immunometabolic differences, we next performed *ex vivo* extracellular flux (XF) analyses. Basal and maximal oxygen consumption rate (OCR) were increased in response to bacterial stimulation in AMs from mice that underwent acid aspiration 24 hours prior compared to sham-treated and those aspirated 8 days before (Fig. 6H), linking transcriptional regulation to mitochondrial function.

Additionally, AMs retrieved from mice 24 hours after acid aspiration displayed a significantly reduced extracellular acidification rate (ECAR) when exposed to bacteria compared to sham-treated animals (Fig. 6I). Simultaneously, secretion of pro-inflammatory cytokines (IL-1β, IL-6, and TNF-α) was reduced in AMs during inflammation resolution compared to controls *ex vivo* (Fig. 6J), while anti-inflammatory IL-10 levels were highest after stimulation with PA in AMs of mice that received acid 24 hours earlier (Fig. 6K).

Therefore, AMs show a temporarily weakened response to bacteria, accompanied by increased oxygen consumption.

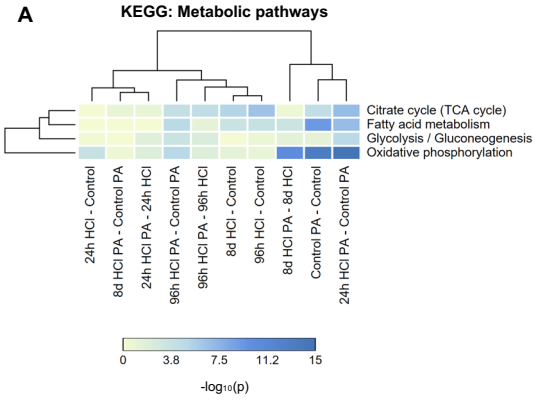

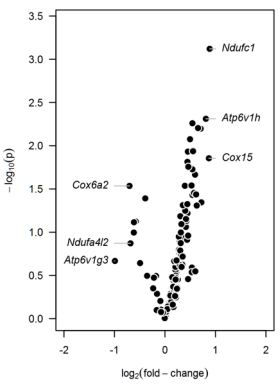

C

24h HCl+PA - Control+PA				
Gene set				
ID	Name	num. of genes	Sign. (-logP)	Direction
01100	Metabolic pathways	1263	38,71	Up
00190	Oxidative phosphorylation	115	14,50	
03050	Proteasome	44	13,59	
01200	Carbon metabolism	117	13,57	
04110	Cell cycle	123	13,55	
04010	MAPK signaling pathway	292	6,29	Down
04080	Neuroactive ligand-receptor interaction	280	5,68	
04658	Th1 and Th2 cell differentiation	85	5,37	
05140	Leishmaniasis	64	4,78	
05152	Tuberculosis	174	4,39	

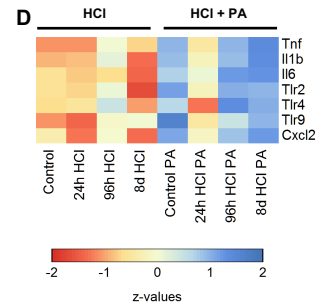

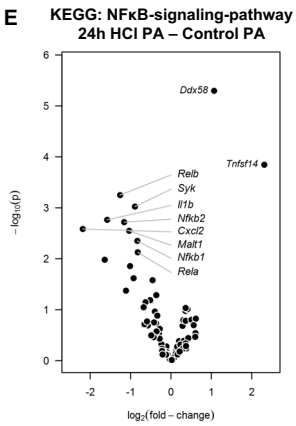

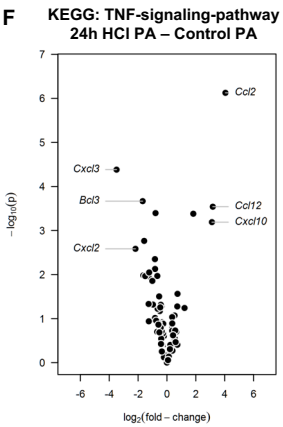

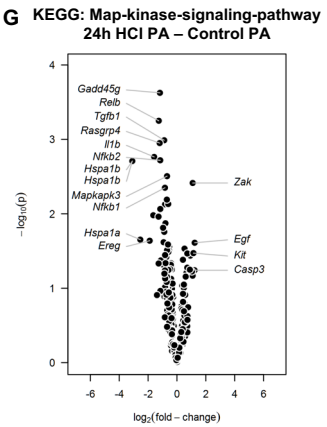

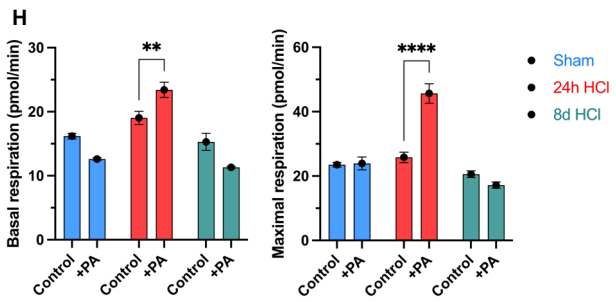

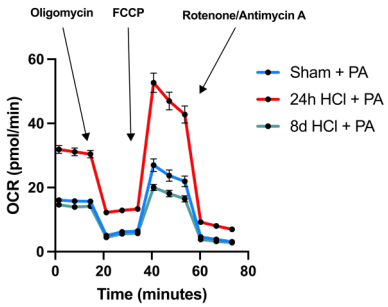

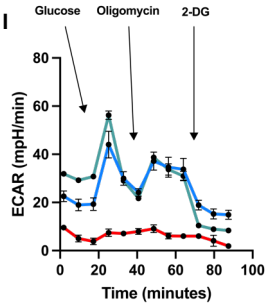

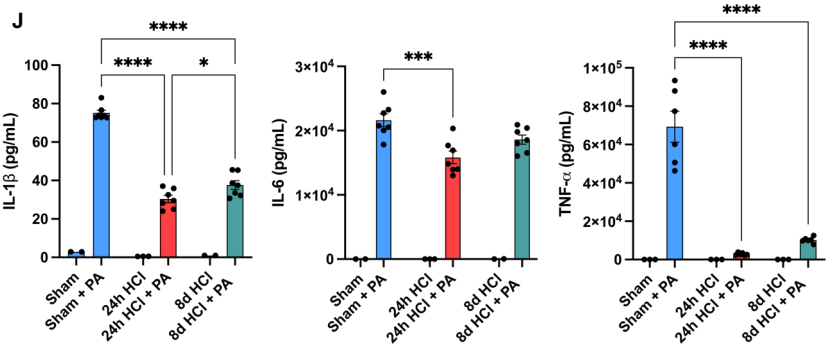

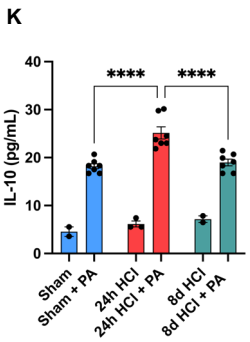

Figure 6. Transcriptional and immunometabolic profile of AMs during acid aspiration and subsequent bacterial infection

(**A** to **G**) Microarray of sorted AMs during acid aspiration (ranging from 24 hours to 8 days) with or without PA infection (3 hours) shown as KEGG metabolic pathway analysis (**A**), volcano plot depicting differentially regulated genes between AMs from mice 24 hours after acid aspiration followed by PA infection versus PA infection alone – OxPhos genes (**B**), NFκB- (**E**), TNF- (**F**), or Map-kinase-signaling pathway (**G**) -, most significantly altered KEGG-pathways (**C**), and heatmap of selected pro-inflammatory genes (**D**) (Microarray data from n=4 mice per group).
(**H**) OCR during a mitochondrial stress test of AMs after acid aspiration *ex vivo* in response to PA, showing basal respiration (left), maximal respiration (middle), and full OCR analysis (right) (n=3 to 6 replicates per group, pooled from three to five mice per group, representative of two independent experiments).
(**I**) ECAR during a glycolytic stress test of AMs after acid aspiration *ex vivo* in response to PA (n=6 to 16 replicates per group, pooled from five to eight mice per group, and two independent experiments). 2-DG=2-deoxyglucose.
(**J** and **K**) IL-1β (G: left), IL-6 (G: middle), TNF-□ (G: right), and IL-10 (H) secretion by AMs after acid aspiration (24h–8d HCl) in response to PA ex vivo (n=3-7 replicates/group, pooled from 3-6 mice/group and two independent experiments).
P < 0.05, **P < 0.01, ***P < 0.001, ****P < 0.0001* by two-way ANOVA with Šídák's multiple comparisons test (H**, **J** and **K**). Statistical significance in (**A** to **G**) is presented as negative log*P* value (**A**), or negative logP value versus $\log_2$(fold change) (**B**, **E** to **G**), or z-score (**D**). Data are shown as the means ± SEM.

AMs are impaired in mtROS-associated bacterial killing during resolution of inflammation

Mitochondria generate mtROS during respiration which are critical to mediate bactericidal properties in macrophages linking OxPhos with macrophage effector function (136, 138). Therefore, we evaluated AMs retrieved from acid-exposed versus sham-treated mice to produce mtROS in response to PA *ex vivo*. 24 hours after acid aspiration, AMs were unable to mount mtROS upon bacterial stimulation, while this capability was restored after 8 days (Fig. 7, A to C, using MitoSOX/flow cytometry (Fig. 7, A and B) or MitoNeoD/confocal microscopy (Fig. 7C) to quantify mtROS production). In contrast, the production of cROS remained unaffected in AMs from mice that experienced acid aspiration (Fig. 7D, using CM-H2DCFDA to quantify cROS production). The ETC generates a baseline level of mtROS during homeostasis (128-132). An increase of the MMP favors reverse electron transport and mtROS production while restricting forward electron transport, oxygen consumption, and ATP generation under certain conditions (131-134). Thus, an elevated MMP is recognized as a driving force for mtROS production and linked to mtROS generation in response to LPS (88).

AMs from mice 24 hours post acid aspiration displayed no increase in MMP upon bacterial stimulation *ex vivo*, whereas AMs of sham-treated mice or those from mice 8 days after aspiration responded by a rise in MMP (Fig. 7, E to G, using JC-1 (Fig. 7, E and F) or TMRM (Fig. 7G) to quantify MMP flow cytometrically). Highlighting the significance of mtROS in bacterial control, the mtROS scavenger MitoTEMPO (MitoT) reduced intracellular bacterial killing in AMs from sham-treated animals and those that received acid either 8 days or 12 hours before, but it did not affect the bacterial killing capacity of AMs 24 hours after acid aspiration *ex vivo* (Fig. 7H). MitoT eliminated the increased mtROS signal detected by MitoSOX in response to PA (Fig. 7I). Beyond contributing to bactericidal properties, mtROS have been shown to affect cytokine secretion (207, 208). *In vitro* scavenging of mtROS in AMs significantly reduced secretion of IL-1β and IL-6 in response to PA (Fig. 7J). However, the release of TNF-α and the anti-inflammatory cytokine IL-10 was unaffected in this context (Fig. 7, J and K). Similarly, we confirmed that AMs collected from mice after pulmonary acid aspiration were impaired in mtROS-dependent release of IL-1β and IL-6 during *ex vivo* bacterial challenge. MitoT reduced the levels of these cytokines only after sham treatment and at 8 days post aspiration (i.e., when mtROS was mounted upon bacterial encounter), but not at 24 hours after acid aspiration

(Fig. 7L). In contrast, the secretion of TNF-α (Fig. 7L) and IL-10 (Fig. 7M) remained unaffected by mtROS scavenging.

Hence, during resolution of inflammation, AMs display a defect in mtROS generation in response to bacteria, impacting both mtROS-dependent bacterial clearance and secretion of pro-inflammatory cytokines.

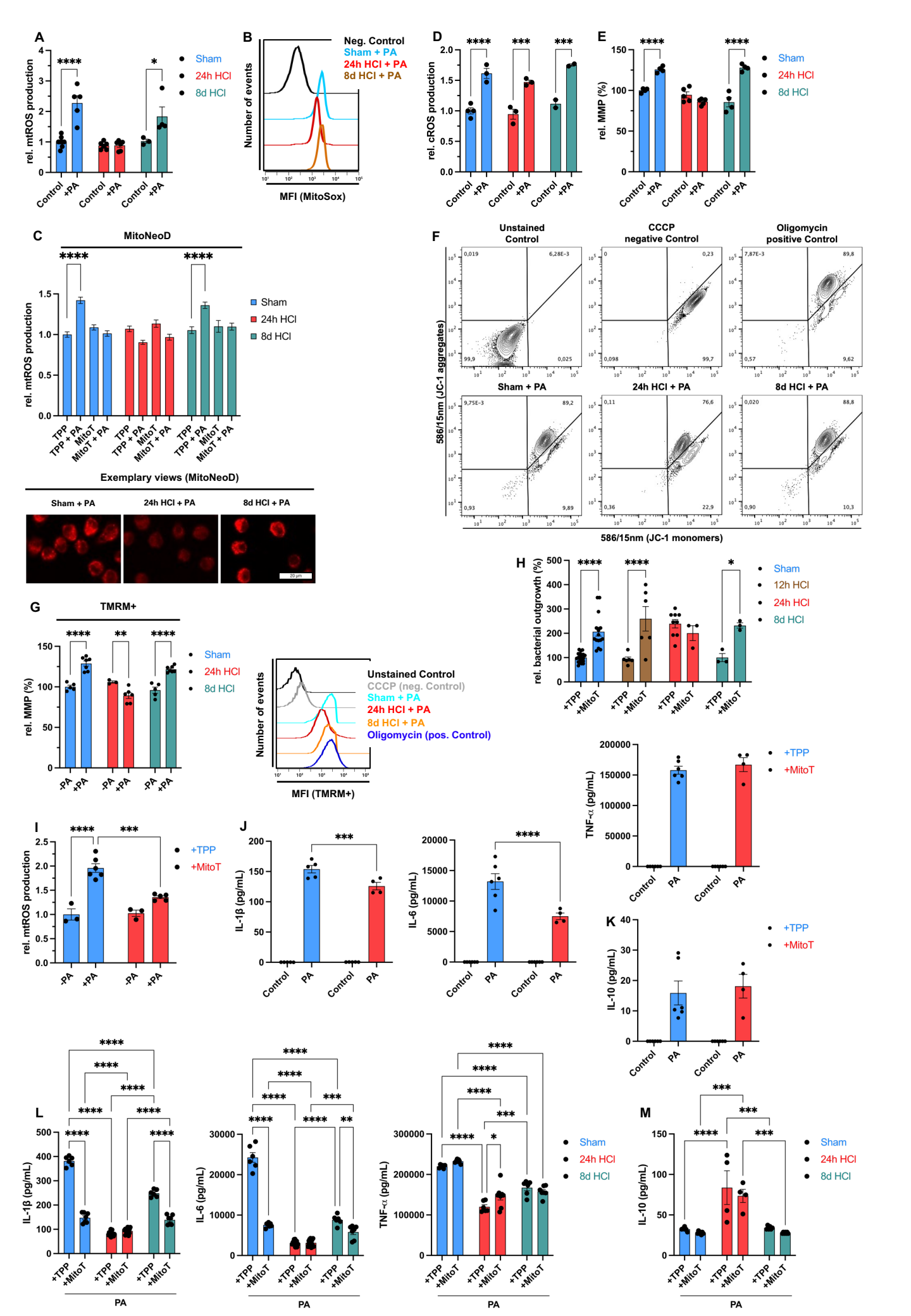
A
rel. mtROS production
Sham
24h HCl
8d HCl
Control
+PA
B
Neg. Control
Sham + PA
24h HCl + PA
8d HCl + PA
Number of events
MFI (MitoSox)
C
MitoNeoD
rel. mtROS production
TPP
TPP + PA
MitoT
MitoT + PA
Exemplary views (MitoNeoD)
Sham + PA
24h HCl + PA
8d HCl + PA
D
rel. cROS production
E
rel. MMP (%)
F
Unstained Control
CCCP negative Control
Oligomycin positive Control
Sham + PA
24h HCl + PA
8d HCl + PA
586/15nm (JC-1 aggregates)
586/15nm (JC-1 monomers)
G
TMRM+
rel. MMP (%)
Unstained Control
CCCP (neg. Control)
Sham + PA
24h HCl + PA
8d HCl + PA
Oligomycin (pos. Control)
MFI (TMRM+)
H
rel. bacterial outgrowth (%)
12h HCl
+TPP
+MitoT
I
rel. mtROS production
J
IL-1β (pg/mL)
IL-6 (pg/mL)
TNF-α (pg/mL)
K
IL-10 (pg/mL)
L
M

Fig. 7. AMs fail to mount mtROS in response to bacteria after acid aspiration

(**A** to **F**) Ex vivo analyses of AMs (mtROS, cROS, MMP) in response to PA retrieved at indicated time points after acid aspiration (Sham versus 12h-8d HCl) (n = 3 to 11 replicates per group, pooled from five to ten mice per group, pooled from two independent experiments (**C** and **F**) or representative of two or three independent experiments (**A** and **B**, **D** and **E**)):

(**A**) mtROS production as measured by flow cytometry using MitoSox

(**B**) Representative flow plot of (**A**)

(**C**) mtROS production as measured by confocal microscopy using MitoNeoD with exemplary views demonstrating MitoNeoD staining (red color)

(**D**) cROS production as measured by flow cytometry using CM-H2DCFDA

(**E** to **G**) MMP as measured by JC-1 (**E**) with a representative flow plot (**F**) and TMRM with a representative flow plot (**G**)

(**H**) Bacterial killing (PA) of AMs +/− MitoT (Control/carrier: TPP) retrieved at indicated time points after acid aspiration (Sham versus 12h-8d HCl) (n=3 to 21 replicates per group, pooled from 3 to 12 mice per group and five independent experiments). TPP=Triphenylphosphonium; CCCP=carbonyl cyanide 3-chlorophenylhydrazone.

(**I**) mtROS production by AMs +/- MitoT (Control/carrier: TPP) in response to PA (n=3-5 replicates/group, pooled from three mice/group and two independent experiments. TPP=Triphenylphosphonium.

(**J** and **K**) Cytokine release by AMs, IL-1β (**J**: left), IL-6 (**J**: middle), TNF-α (**J**: right), IL-10 (**K**), in response to PA +/− MitoT (Control/carrier: TPP) *ex vivo* retrieved at indicated time points after acid aspiration (Sham versus 24h-8d HCl) (n = 4 to 14 replicates per group, pooled from three to seven mice per group, representative of two independent experiments).

(**L** and **M**) Cytokine release by AMs +/- MitoT in response to PA secretion of AMs +/- MitoT (Control/carrier: TPP) (n=3-6 replicates/group, pooled from 3-5 mice/group, representative of two independent experiments): IL-1β (**L**: left), IL-6 (**L**: middle), TNF-α (**L**: right), and IL-10 (**M**).

P < 0.05, **P < 0.01, ***P < 0.001, and ****P < 0.0001* by two-way ANOVA (A**, **D** and **E**, **G** to **M**) and three-way ANOVA (**C**) with Šídák's or Tukey's multiple comparisons tests, respectively. Data are shown as the means ± SEM.

Efferocytosis of neutrophils leads to increased oxygen consumption and precludes mtROS release in response to bacteria in AMs

Next, we aimed to identify alveolar signals that render AMs unable to fend off bacteria while promoting OxPhos during resolution of acid-induced pneumonitis. Incubating AMs with BALF from mice post acid aspiration did not affect their bactericidal abilities (Fig. 8A), which led us to examine the cellular composition of BALF following acid aspiration.

We observed remarkable accumulation of apoptotic epithelial cells (the main component of $CD45^-$ cells) and PMNs, with both apoptotic cell types peaking around 12 to 24 hours following acid instillation (Fig. 8B). Given that AMs play a crucial role in clearing apoptotic cells during inflammation resolution, we hypothesized that efferocytosis could influence innate immune effector functions *in vivo*. To evaluate the potential effect of efferocytosis on mtROS production in AMs, apoptosis was induced in AECs and PMNs using staurosporine, achieving similar levels of apoptosis (Fig. 8C). Interestingly, over time, efferocytic uptake of AECs and PMNs by AMs was comparable (Fig. 8D). However, while AMs ingesting apoptotic AECs did not show changes in mtROS production, the uptake of apoptotic PMNs completely inhibited mtROS generation following bacterial stimulation with PA and *S. pneumoniae* (Spn) *in vitro* (Fig. 8, E and F). In line with this, efferocytosis of PMNs by AMs, unlike that of AECs, blocked the increase in MMP and consequently reduced the bactericidal activity against PA (Fig. 8, G and H). Consistent with our *ex vivo* findings, scavenging mtROS did not further decrease bactericidal properties of AMs after PMN efferocytosis *in vitro* (Fig. 8I). Notably, ingesting apoptotic PMNs did not affect the release of cROS upon encountering bacteria (Fig. 8J).

Given the differing numbers of apoptotic neutrophils and $CD45^-$ cells observed in BALF analysis (Fig. 8B), we tested varying ratios of apoptotic PMNs and AECs to AMs. Even at an apoptotic cell to efferocyte (AC:EC) ratio of one apoptotic PMN on every seven AMs, mtROS production decreased, whereas ten apoptotic AECs per AM did not affect mtROS generation when challenged with PA (Fig. 8K). Intracellular staining of AMs against neutrophil marker Ly6G and epithelial marker EpCAM showed increased signals for both cell types during inflammation resolution (Fig. 8L), indicating that AMs ingest both apoptotic PMNs and AECs *in vivo*.

Consistent with reduced mtROS production, cytokine release by AMs was completely (IL-1β) or partially (IL-6) diminished following PMN efferocytosis and a subsequent bacterial

challenge (Fig. 8M). Ingesting apoptotic AECs slightly lowered IL-6 levels, whereas the uptake of either apoptotic AECs or PMNs reduced TNF-α release in response to PA (Fig. 8M).

Interestingly, significant baseline IL-10 secretion was observed after efferocytosis of both AECs and PMNs by AMs, even without bacterial stimulation (Fig. 8N). Conversely, AMs, treated with PA, released IL-10 only after PMN efferocytosis (Fig. 8O). Moreover, ingesting apoptotic Jurkat cells or primary AECs (pAECs) did not affect mtROS production in response to bacteria (Fig. 8P) and did not hinder bacterial killing (Fig. 8Q).

Only the uptake of neutrophils reduced IL-1β release (Fig. 8R). Similarly, only efferocytosis of apoptotic neutrophils, and not Jurkat cells or pAECs, led to IL-10 secretion during bacterial challenge (Fig. 8S). Notably, efferocytosis in general (of all tested cell types) did not impact the phagocytosis of PA (Fig. 8T), and AMs that ingested apoptotic cargo maintained the same phagocytic capacity as those that did not (Fig. 8U).

Collectively, our findings indicate that the effects of efferocytosis on the functional phenotype of AMs are specific to the apoptotic cargo. Ingestion of PMNs, but not AECs or T-cells, suppressed mtROS release in AMs during bacterial challenge, ultimately impairing bacterial elimination and reducing the secretion of pro-inflammatory cytokines while enhancing IL-10 secretion.

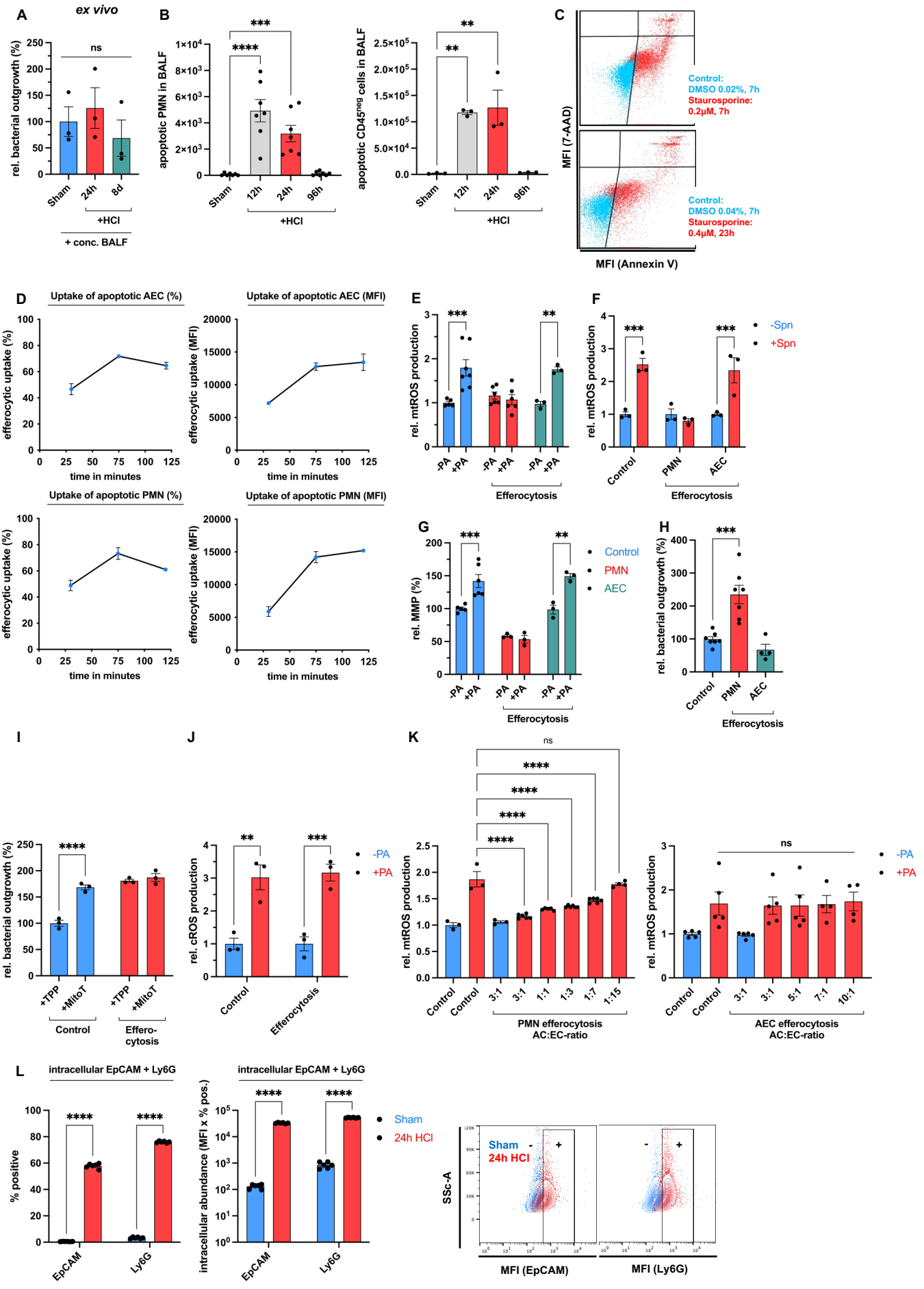
A
ex vivo
rel. bacterial outgrowth (%)
ns
Sham
24h
8d
+HCl
+ conc. BALF
B
apoptotic PMN in BALF
***
****
Sham
12h
24h
96h
+HCl
apoptotic CD45neg cells in BALF
**
**
C
MFI (7-AAD)
MFI (Annexin V)
Control:
DMSO 0.02%, 7h
Staurosporine:
0.2µM, 7h
Control:
DMSO 0.04%, 7h
Staurosporine:
0.4µM, 23h
D
Uptake of apoptotic AEC (%)
efferocytic uptake (%)
time in minutes
Uptake of apoptotic AEC (MFI)
efferocytic uptake (MFI)
time in minutes
Uptake of apoptotic PMN (%)
efferocytic uptake (%)
time in minutes
Uptake of apoptotic PMN (MFI)
efferocytic uptake (MFI)
time in minutes
E
rel. mtROS production
***
**
-PA
+PA
Efferocytosis
F
rel. mtROS production
***
***
-Spn
+Spn
Control
PMN
AEC
Efferocytosis
G
rel. MMP (%)
***
**
Control
PMN
AEC
Efferocytosis
H
rel. bacterial outgrowth (%)
***
Control
PMN
AEC
Efferocytosis
I
rel. bacterial outgrowth (%)
****
+TPP
+MitoT
Control
Effero-cytosis
J
rel. cROS production
**
***
-PA
+PA
Control
Efferocytosis
K
rel. mtROS production
ns
****
****
****
****
Control
Control
3:1
3:1
1:1
1:3
1:7
1:15
PMN efferocytosis
AC:EC-ratio
rel. mtROS production
ns
-PA
+PA
Control
Control
3:1
3:1
5:1
7:1
10:1
AEC efferocytosis
AC:EC-ratio
L
intracellular EpCAM + Ly6G
% positive
****
****
EpCAM
Ly6G
intracellular EpCAM + Ly6G
intracellular abundance (MFI x % pos.)
****
****
Sham
24h HCl
EpCAM
Ly6G
SSc-A
Sham
24h HCl
MFI (EpCAM)
MFI (Ly6G)

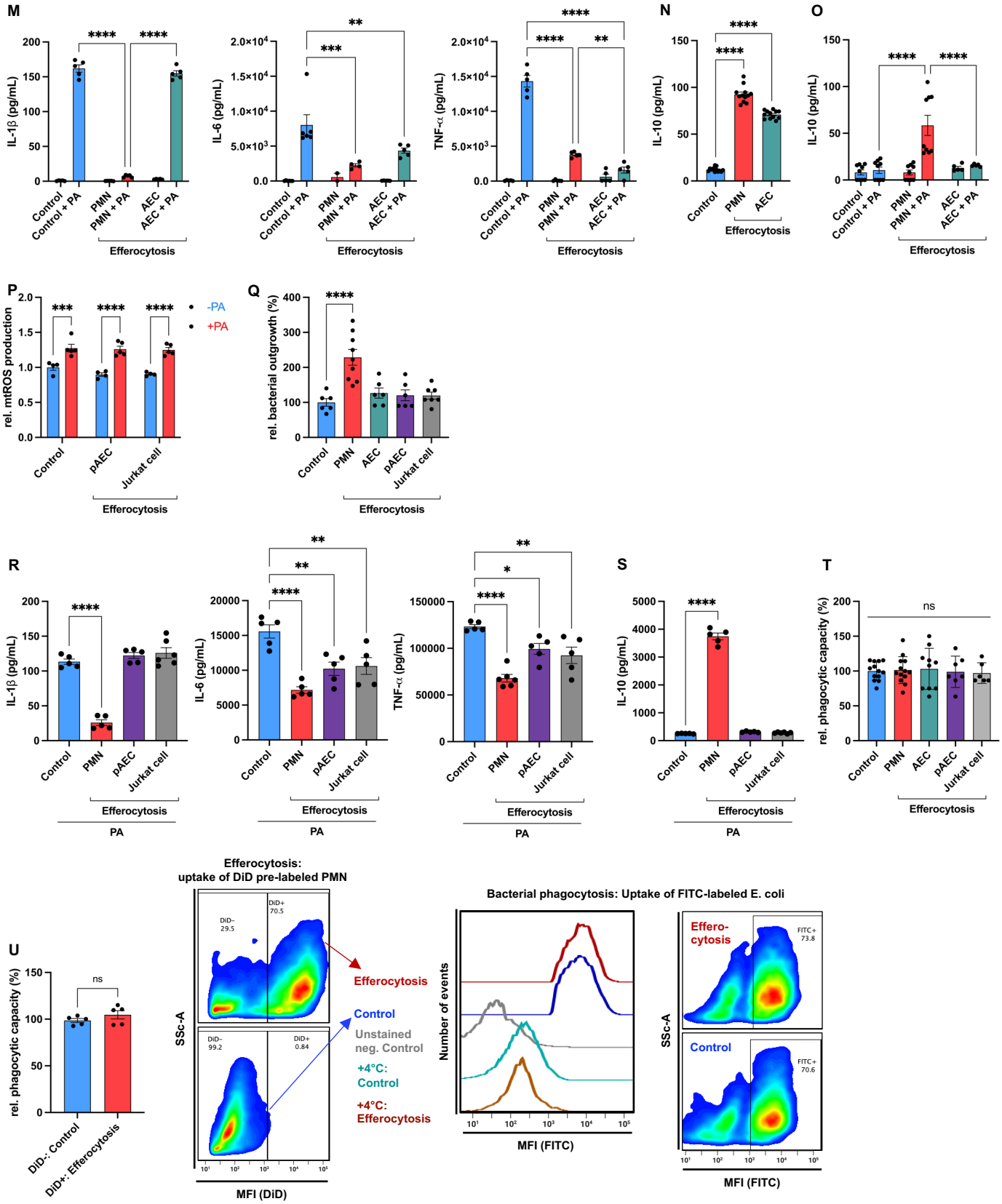
M
IL-1β (pg/mL)
IL-6 (pg/mL)
TNF-α (pg/mL)
Control
Control + PA
PMN
PMN + PA
AEC
AEC + PA
Efferocytosis
N
IL-10 (pg/mL)
O
P
rel. mtROS production
-PA
+PA
pAEC
Jurkat cell
Q
rel. bacterial outgrowth (%)
R
S
T
rel. phagocytic capacity (%)
ns
PA
U
DiD−: Control
DiD+: Efferocytosis
Efferocytosis:
uptake of DiD pre-labeled PMN
DiD− 29.5
DiD+ 70.5
DiD− 99.2
DiD+ 0.84
SSc-A
MFI (DiD)
Efferocytosis
Control
Unstained
neg. Control
+4°C:
Control
+4°C:
Efferocytosis
Bacterial phagocytosis: Uptake of FITC-labeled E. coli
Number of events
MFI (FITC)
Effero-
cytosis
FITC+
73.8
FITC+
70.6

Fig. 8. Cell type–specific efferocytosis of PMNs precludes mtROS generation in response to bacteria in AMs

(**A**) Bacterial killing capacity (PA) of AMs treated for 16h with concentrated BALF collected from mice that underwent acid aspiration (Sham versus 24h-8d HCl) (n=3 replicates/group, pooled from four mice/group and two independent experiments).

(**B**) Number of apoptotic PMNs (left) and $CD45^-$ cells (right) in BALF after different time points of acid aspiration (n = 3 to 7 mice per group, pooled from two independent experiments).

(**C**) Quadrant analysis of annexin V+ and propidium iodide- apoptotic PMNs (top) and AECs (bottom) after incubation with staurosporine.

(**D**) Efferocytic capacity of AMs to clear calcein pre-labeled apoptotic AECs or PMNs expressed as "calcein+ macrophages (%)" or "MFI of calcein" (n=2 replicates/time point, pooled from two mice/group and two independent experiments).

(**E**) mtROS production of AMs after efferocytosis of PMNs or AECs in response to PA (n = 3 to 7 replicates per group, pooled from three to five mice per group and two independent experiments).

(**F**) mtROS production by AMs after clearance of apoptotic PMNs or AECs in response to S. pneumoniae (Spn) (MOI=100, 6-8h) (n=3 replicates/group, pooled from four mice/group and two independent experiments).

(**G**) MMP measurement in AMs after efferocytosis of PMNs or AECs in response to PA (n = 3 to 6 replicates per group, pooled from three to five mice per group and two independent experiments).

(**H**) Bacterial killing capacity (PA) of AMs after efferocytosis of PMNs or AECs (n = 4 to 7 replicates per group, pooled from three to five mice per group and two independent experiments).

(**I**) Bacterial killing capacity (PA) of AMs after efferocytosis of PMNs compared with control (no efferocytosis) +/− MitoT (n = 3 replicates per group, pooled from four mice per group, representative of three independent experiments).

(**J**) Assessment of cROS production after efferocytosis of apoptotic PMNs in response to PA (n=3 replicates/group, pooled from four mice/group and two independent experiments).

(**K**) mtROS production of AMs after clearance of apoptotic PMNs (left) or AECs (right) with varying AC:EC ratios (n = 3 to 6 replicates per group, pooled from three to five mice per group and two independent experiments). ns, not significant.

(**L**) Intracellular staining against EpCAM and Ly6G in AMs harvested 24 hours after acid aspiration determined by flow cytometry (n = 6 mice per group, pooled from two independent experiments).

(**M** and **O**) IL-1β (**M**: left), IL-6 (**M**: middle), TNF-α (**M**: right), and IL-10 (**O**) secretion of AMs after efferocytosis of apoptotic PMNs or AECs in response to PA (n=3-9 replicates/group, pooled from 3-7 mice/group and two independent experiments).

(**N**) IL-10 secretion of AMs after efferocytosis of apoptotic PMNs or AECs without bacterial stimulation (n=10-12 replicates/group, pooled from six mice/group and two independent experiments).

(**P**) mtROS production by AMs after clearance of apoptotic pAECs or Jurkat cells in response to PA (n=4-6 replicates/group, pooled from four mice/group and two independent experiments).

(**Q**) Bacterial killing capacity (PA) of AMs after clearance of apoptotic PMNs, AECs and pAECs, or Jurkat cells (n=6-9 replicates/group, pooled from six mice/group and two to four independent experiments).
(**R** and **S**) IL-1β (**R**: left), IL-6 (**R**: middle), TNF-α (**R**: right), and IL-10 (**S**) secretion of AMs after efferocytosis of apoptotic PMNs, pAECs, or Jurkat cells in response to PA (n=5-6 replicates/group, pooled from 5 mice/group and two independent experiments).
(**T**) Relative phagocytic capacity of AMs (PA, MOI=100, 1h) following clearance of apoptotic PMNs, AECs and pAECs, or Jurkat cells (n=6-13 replicates/group, pooled from 4-7 mice/group and two independent experiments).
(**U**) Relative phagocytic capacity of AMs as determined by uptake of FITC-labeled *E. coli* following clearance of DiD pre-labeled apoptotic PMNs (n=5 replicates/group, pooled from 4 mice/group and two independent experiments).
P < 0.05, **P < 0.01, ***P < 0.001, and ****P < 0.0001* by Student's t-test (U**), one-way ANOVA with Tukey's (**B**, **H**, **K**, **N**, **Q** to **T**) and Dunnett´s multiple comparisons tests (**A**), or two-way ANOVA with Šídák's multiple comparisons test (**E** to **G**, **I** and **J**, **L** and **M**, **O** and **P**). Data are shown as the means ± SEM.

Neutrophil-derived MPO mediates immunometabolic alterations upon efferocytosis in AMs in response to bacteria

We next aimed to decipher how apoptotic PMNs induce efferocytosis-induced immunometabolic changes in AMs in a cell-type-specific manner. Given that major constituents of PMN granules are enzymes that play key roles in immunity and antimicrobial functions, we investigated NGAL, elastase (ELA-2), and MPO for their effects on mtROS production during bacterial stimulation in AMs. While AMs treated with ELA-2 and NGAL retained mtROS production capability, pre-incubation with MPO completely suppressed mtROS production in response to PA (Fig. 9A). Inhibition of MPO's enzymatic function with 4-Aminobenzoic acid hydrazide reversed this effect (Fig. 9B). Notably, the MPO concentration used (0.5µM) did not compromise AM viability (Fig. 9C). Furthermore, mitochondrial content remained unchanged by MPO treatment in vitro (Fig. 9D) and 24 hours post acid aspiration *ex vivo* (Fig. 9E). To investigate MPO's effect during efferocytosis, we incubated AMs with apoptotic PMNs from either wildtype (WT) or *Mpo*$^{-/-}$ animals. MPO deficiency reinstated AMs' ability to produce mtROS (Fig. 9F) and increased MMP following efferocytosis in response to bacteria (Fig. 9G). Consequently, the bactericidal capacity of AMs significantly improved after exposure to PMNs lacking MPO compared to WT PMNs (Fig. 9H). MPO did not affect bacterial internalization by AMs (Fig. 9I). Cytokine secretion following efferocytosis of *Mpo*$^{-/-}$ or WT PMN supported previous results on mtROS reliance: IL-1β was entirely, and IL-6 partially reduced, whereas TNF-α and IL-10 remained unaffected by pre-incubation with MPO when challenged with bacteria (Fig. 9, J and K). Intriguingly, incubation with cell-free supernatant alone mirrored mtROS generation in an MPO-dependent manner, akin to whole apoptotic cell incubation (Fig. 9L). MPO had a dose-dependent dominant effect on mtROS production even in the presence of apoptotic AECs (Fig. 9M) and IL-1β secretion (Fig. 9N). Similarly, MPO reduced bacterial control even with 10 AECs per AM (Fig. 9O). Intracellular AM staining during resolution of acid aspiration indicated over 90% of AMs were MPO^{+} (Fig. 9, P and Q). Extracellular flux analysis of AMs ingesting Mpo$^{-/-}$ PMNs showed lower basal and maximal respiration compared to those with WT PMNs during bacterial challenge, reaffirming that enhanced OxPhos correlates with diminished antibacterial response (Fig. 9R). MPO alone elevated maximal respiration while augmenting basal and maximal OCR upon bacterial stimulation (Fig. 9S).

Collectively, PMN-derived MPO, released during efferocytosis, suppresses mtROS production and increases oxygen consumption in response to bacteria in AMs.

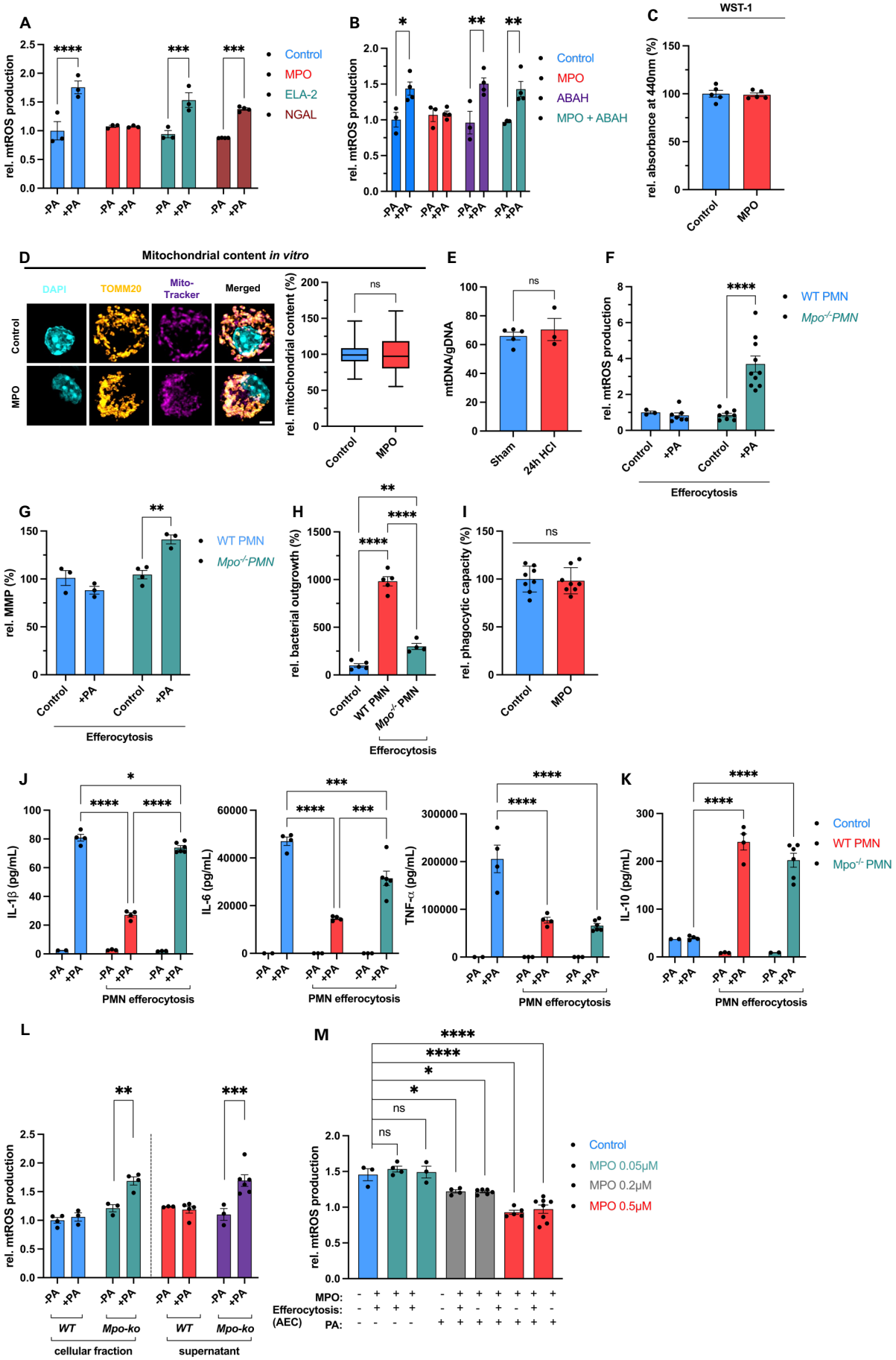
A
rel. mtROS production
Control
MPO
ELA-2
NGAL
-PA
+PA
B
rel. mtROS production
Control
MPO
ABAH
MPO + ABAH
C
WST-1
rel. absorbance at 440nm (%)
Control
MPO
D
Mitochondrial content in vitro
DAPI
TOMM20
Mito-Tracker
Merged
Control
MPO
rel. mitochondrial content (%)
ns
E
mtDNA/gDNA
ns
Sham
24h HCl
F
rel. mtROS production
WT PMN
Mpo-/- PMN
Control
+PA
Efferocytosis
G
rel. MMP (%)
WT PMN
Mpo-/- PMN
Efferocytosis
H
rel. bacterial outgrowth (%)
Control
WT PMN
Mpo-/- PMN
Efferocytosis
I
rel. phagocytic capacity (%)
ns
Control
MPO
J
IL-1β (pg/mL)
IL-6 (pg/mL)
TNF-α (pg/mL)
PMN efferocytosis
K
IL-10 (pg/mL)
Control
WT PMN
Mpo-/- PMN
PMN efferocytosis
L
rel. mtROS production
WT
Mpo-ko
cellular fraction
supernatant
M
rel. mtROS production
Control
MPO 0.05µM
MPO 0.2µM
MPO 0.5µM
MPO:
Efferocytosis:
(AEC)
PA:

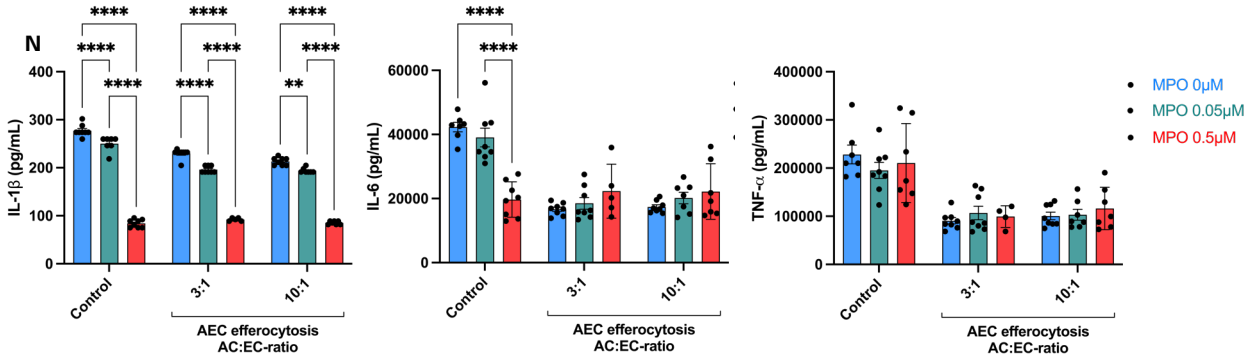
N
IL-1β (pg/mL)
IL-6 (pg/mL)
TNF-α (pg/mL)
MPO 0μM
MPO 0.05μM
MPO 0.5μM
Control
3:1
10:1
AEC efferocytosis
AC:EC-ratio

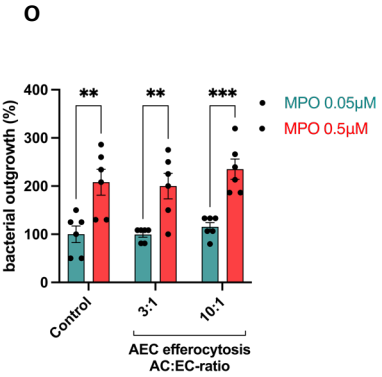
O
bacterial outgrowth (%)
MPO 0.05μM
MPO 0.5μM
Control
3:1
10:1
AEC efferocytosis
AC:EC-ratio

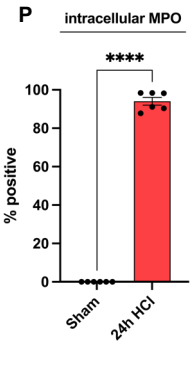
P
intracellular MPO
% positive
Sham
24h HCl

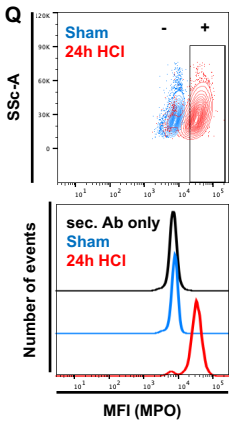
Q
Sham
24h HCl
SSc-A
sec. Ab only
Number of events
MFI (MPO)

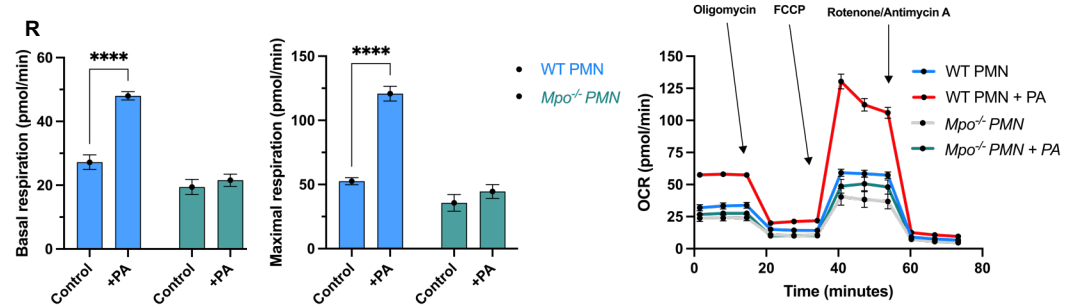
R
Basal respiration (pmol/min)
Maximal respiration (pmol/min)
WT PMN
Mpo-/- PMN
Control
+PA
Oligomycin
FCCP
Rotenone/Antimycin A
OCR (pmol/min)
Time (minutes)
WT PMN + PA
Mpo-/- PMN + PA

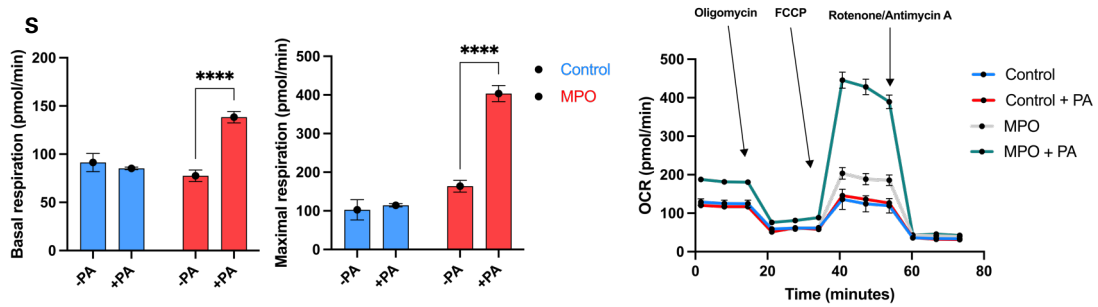
S
Basal respiration (pmol/min)
Maximal respiration (pmol/min)
Control
MPO
-PA
+PA
Oligomycin
FCCP
Rotenone/Antimycin A
OCR (pmol/min)
Time (minutes)
Control + PA
MPO + PA

Fig. 9. PMN-derived MPO mediates alterations of AM functions in response to bacteria

(**A**) mtROS measurement in AMs +/− MPO, ELA-2, or NGAL in response to PA (n = 3 or 4 replicates per group, pooled from three mice per group and two independent experiments).

(**B**) mtROS production by AMs after pre-treatment with MPO +/- 4-Aminobenzoic acid hydrazide (ABAH) in response to PA (n=3-4 replicates/group, pooled from three mice/group and two independent experiments).

(**C**) Assessment of cell viability of AMs +/- MPO 0.5□M using the WST-1 assay (n=5 replicates/group, pooled from three mice/group and two independent experiments).

(**D**) Confocal microscopy of AMs +/− MPO; MFI quantification of anti-TOMM20 normalized to control (scale bars, 2 μM; n = 4 mice per group, pooled from two independent experiments). DAPI, 4',6-diamidino-2-phenylindole.

(**E**) Mitochondrial content 24h after acid aspiration compared to sham treatment determined by the ratio of mitochondrial to genomic DNA (mtDNA/gDNA) as measured by quantitative PCR (n=3-5 replicates/group, pooled from 3-4 mice/group and two independent experiments).

(**F**) mtROS measurement in AMs after efferocytosis of WT or *Mpo*$^{-/-}$ PMNs in response to PA (n = 3 to 10 replicates per group, pooled from three to eight mice per group and two independent experiments).

(**G**) MMP measurement in AMs after efferocytosis of WT or *Mpo*$^{-/-}$ PMNs in response to PA (n = 3 or 4 replicates per group, pooled from three or four mice per group and two independent experiments).

(**H**) Bacterial killing capacity (PA) of AMs after efferocytosis of WT or *Mpo*$^{-/-}$ PMNs (n = 4 or 5 replicates per group, pooled from four mice per group, representative of three independent experiments).

(**I**) Relative phagocytic capacity of AMs (PA, MOI=100, 1h) after treatment with MPO (n=8 replicates/group, pooled from 4 mice/group and two independent experiments).

(**J** to **K**) IL-1β (**J**: left), IL-6 (**J**: middle), and TNF-α (**J**: right), and IL-10 (**K**) secretion of AMs after efferocytosis of apoptotic PMNs of wild-type (WT) or MPO-deficient (Mpo-/-) mice in response to PA (n=2-6 replicates/group, pooled from 2-4 mice/group and two independent experiments).

(**L**) mtROS production by AMs after preincubation with different fractions of an apoptotic cell solution (apoptotic cell pellet versus supernatant) in response to PA (n = 3 to 6 replicates per group, pooled from two to four mice per group and two independent experiments).

(**M**) mtROS production by AMs after pre-incubation with apoptotic AECs in presence of varying doses of MPO and response to PA (n=3-6 replicates/group, pooled from 2-4 mice/group and two independent experiments).

(**N**) IL-1β (left), IL-6 (middle), and TNF-α (right) secretion of AMs following clearance of apoptotic AECs with varying AC to EC ratios in presence of varying doses of MPO and subsequent stimulation with PA (n=5-8 replicates/group, pooled from 5-6 mice/group and two independent experiments).

(**O**) Bacterial killing capacity (PA) of AMs upon clearance of apoptotic AECs with varying AC to EC ratios in presence of varying doses of MPO (n=6 replicates/group, pooled from 4 mice/group and two independent experiments).

(**P** and **Q**) Intracellular staining of MPO in AMs 24h after acid aspiration (**G**) with representative flow plots (**H**) (n = 6 mice per group, pooled from two independent experiments).

(**R**) OCR of AMs after efferocytosis of WT or *Mpo*$^{-/-}$ PMNs in response to PA (n = 3 to 6 replicates per group, pooled from three to five mice per group and two independent experiments).

(**S**) OCR during Mito Stress Test of AMs after treatment with MPO in response to PA; basal respiration (left), maximal respiration (middle) and full analysis for OCR (right) (n=3-20 replicates/group, pooled from 2-10 mice/group and two independent experiments).

P < 0.05, **P < 0.01, ***P < 0.001, and ****P < 0.0001* by Student's t test (C** and **D**, **E** and **I**, **P**), one-way ANOVA with Tukey's multiple comparisons test (**H**, **M**), or two-way ANOVA (**A** and **B**, **F** and **G**, **J** and **K**, **N** and **O**, **R** and **S**) and three-way ANOVA (**L**) with Šídák's multiple comparisons test. Data are shown as the means ± SEM.

Neutrophil-derived MPO impairs antibacterial defense *in vivo*

To assess the relevance of our findings *in vivo*, we introduced apoptotic PMNs i.t. and subsequently infected mice with PA (Fig. 10A). Aligning with our *in vitro* findings, MPO deficiency in PMNs improved bacterial clearance compared to WT PMNs *in vivo* (Fig. 10B). Notably, PMN efferocytosis partially reduced bacterial killing *in vitro* and clearance *in vivo*, independent of MPO (Fig. 9H or Fig. 10B, respectively). It is likely additional mechanisms such as prostaglandin E2-mediated inhibition of bacterial killing also play a role (197, 198, 202). To determine if MPO's effect on bacterial control was pathogen- or model specific, we tested *K. pneumoniae* and *S. pneumoniae* in this experimental setup. MPO pre-incubation reduced elimination of both pathogens in vitro (Fig. 10C). Next, we introduced a murine *influenza A virus* pneumonia model. Assessment of broncho-alveolar leukocyte composition over time showed a neutrophil and MDM peak on day 5 or day 7, respectively (Fig. 10D). Consistent with the acid aspiration model, tissue-resident AMs regained mtROS production capacity in response to bacteria after 14 days (Fig. 10, E and F). To conclude, PMN-derived MPO impairs bactericidal properties of AMs *in vivo*.

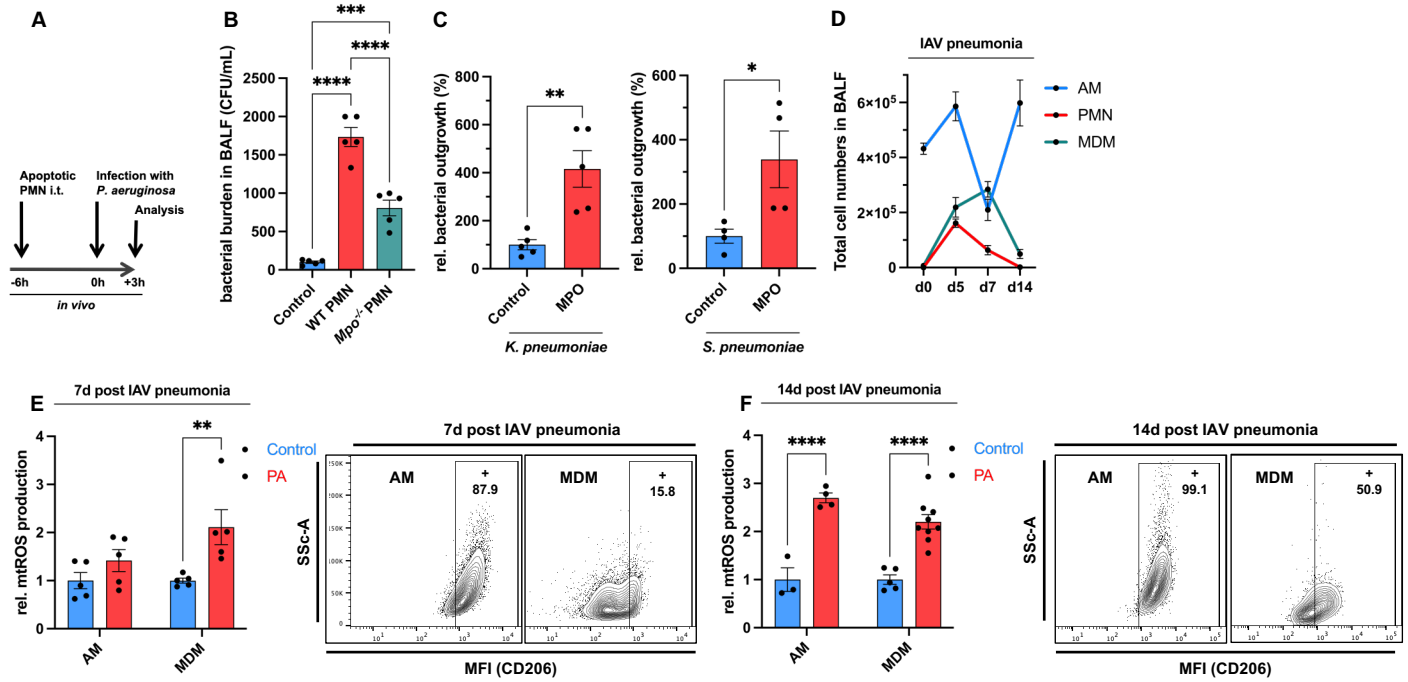
A
Apoptotic PMN i.t.
Infection with P. aeruginosa
Analysis
-6h
0h
+3h
in vivo
B
bacterial burden in BALF (CFU/mL)
Control
WT PMN
Mpo-/- PMN
C
rel. bacterial outgrowth (%)
Control
MPO
K. pneumoniae
S. pneumoniae
D
IAV pneumonia
Total cell numbers in BALF
AM
PMN
MDM
d0
d5
d7
d14
E
7d post IAV pneumonia
rel. mtROS production
Control
PA
AM
MDM
SSc-A
MFI (CD206)
87.9
15.8
F
14d post IAV pneumonia
99.1
50.9

Fig. 10. Neutrophil-derived MPO impairs antibacterial defense *in vivo*

(**A**) Experimental scheme for (N). i.t.=Intratracheally. *Created with BioRender.com

(**B**) Bacterial outgrowth in BALF after instillation of apoptotic WT or *Mpo*$^{-/-}$ PMNs and subsequent infection with PA (n = 5 mice per group, representative of two independent experiments).

(**C**) Bacterial killing capacity (left: K. pneumoniae; right: S. pneumoniae) of AMs +/- pre-treatment with MPO (n=4-5 replicates/group, pooled from four mice/group, representative of two experiments).

(**D**) Total cell number of AMs, PMNs, and MDMs in BALF during influenza A virus (IAV) pneumonia (n=5-6 mice/group, pooled from two independent experiments).

(**E** and **F**) mtROS measurement in AMs and MDMs harvested 7d (O) and 14d (P) after IAV infection in response to PA *ex vivo* (left); exemplary contour plot depicting CD206 expression in AMs and MDMs (right) (n = 3 to 9 mice per group, pooled from two independent experiments).

P < 0.05, **P < 0.01, ***P < 0.001, and ****P < 0.0001* by Student's t test (C**), one-way ANOVA with Tukey's comparisons test (**B**), or two-way ANOVA (**E** and **F**) with Šídák's multiple comparisons test. Data are shown as the means ± SEM.

CD206-dependent receptor-mediated uptake of MPO suppresses mtROS production in AMs in response to bacteria

Previously, the mannose receptor CD206 was identified as mediating MPO uptake by macrophages (209, 210). Indeed, mannose incubation reduced MPO uptake in AM cytosol (Fig. 11, A to C) and restored mtROS production (Fig. 11D). Importantly, mannose saturation didn't entirely prevent mtROS inhibition in the presence of whole apoptotic cells (Fig. 11, E and F). However, inhibition of bacteria-induced mtROS generation depended on MPO's enzymatic activity, regardless of whether MPO was internalized via CD206 or through neutrophil efferocytosis (Fig. 11, E and F). Correlated with CD206 expression levels, $CD206^{+}$ AMs did not produce mtROS in response to bacteria, whereas $CD206^{-}$ MDMs did (Fig. 10, E and F).

In conclusion, efferocytosis and the CD206 receptor mediate the uptake of PMN-derived MPO into AMs to suppresses mtROS production in response to bacteria.

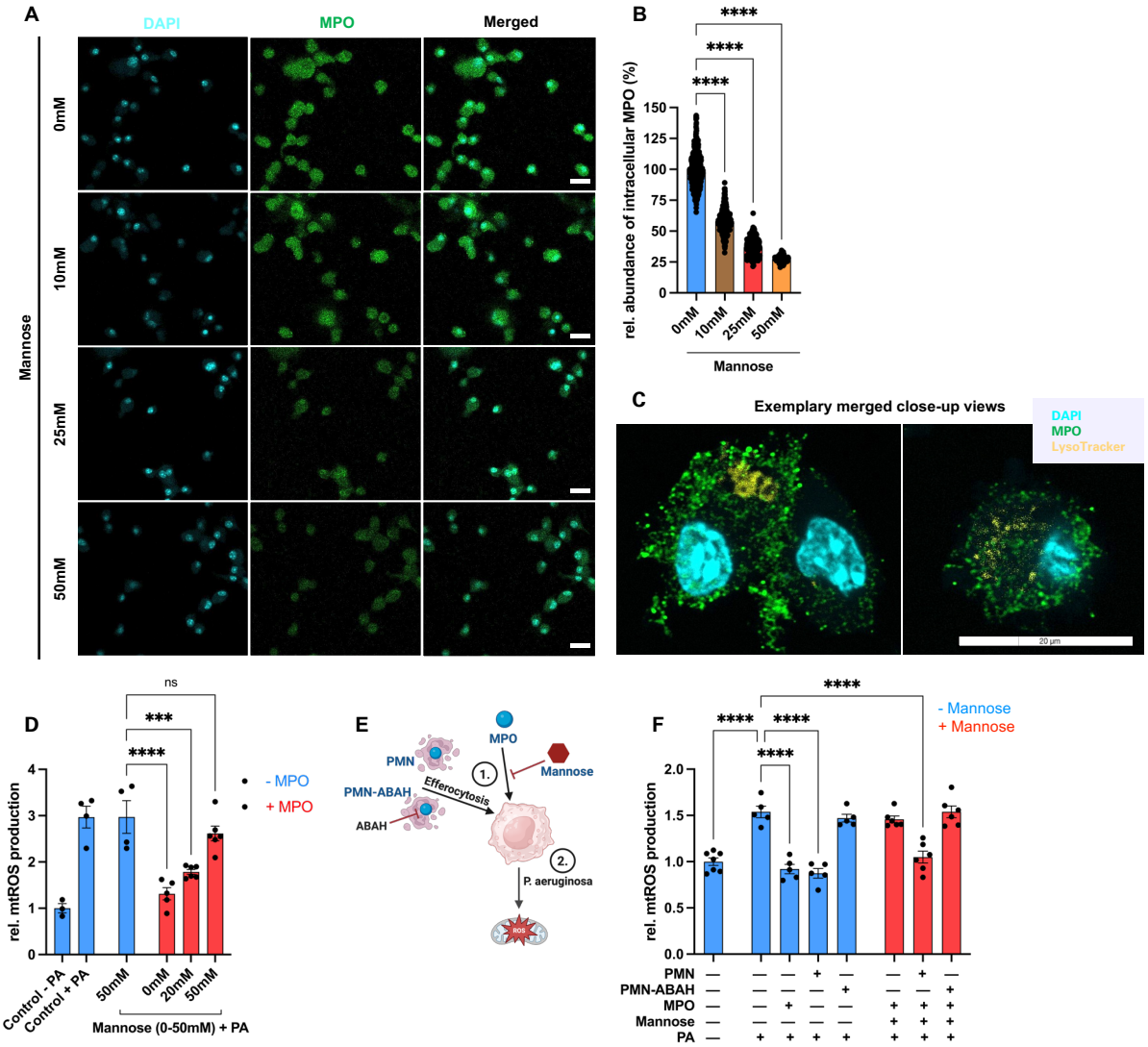
A
DAPI
MPO
Merged
Mannose
0mM
10mM
25mM
50mM
B
rel. abundance of intracellular MPO (%)
****
****
****
0mM
10mM
25mM
50mM
Mannose
C
Exemplary merged close-up views
DAPI
MPO
LysoTracker
20 µm
D
ns
***
****
rel. mtROS production
- MPO
+ MPO
Control - PA
Control + PA
50mM
0mM
20mM
50mM
Mannose (0-50mM) + PA
E
PMN
PMN-ABAH
ABAH
Efferocytosis
MPO
Mannose
1.
2.
P. aeruginosa
ROS
F
****
****
****
****
- Mannose
+ Mannose
rel. mtROS production
PMN
PMN-ABAH
MPO
Mannose
PA

Fig. 11. CD206-dependent receptor-mediated uptake of MPO

(**A** and **B**) Confocal microscopy of AMs treated with MPO +/− mannose, whereby nuclei and MPO were stained with DAPI (blue) or an anti-MPO antibody (green), respectively (**A**); MFI quantification of anti-MPO normalized to MPO without mannose (**B**) (scale bars, 20μM; n = 3 to 5 replicates per group, pooled from four mice per group and two independent experiments).

(**C**) Exemplary confocal microscopy close-up views of AMs after incubation with MPO for 1h; nuclei, MPO, and lysosomes were stained with DAPI (blue), an anti-MPO antibody (green), or lysotracker (yellow), respectively.

(**D**) mtROS measurement in AMs +/− MPO in the presence of mannose in response to PA (n = 3 to 6 replicates per group, pooled from three to five mice per group and two independent experiments).

(**E**) Experimental scheme of (L). *Created with BioRender.com.

(**F**) Apoptotic PMNs +/− 4-aminobenzoic acid hydrazide (ABAH) before coincubation with AMs +/− MPO and AMs +/− mannose before stimulation with PA to quantify mtROS production (n = 5 to 7 replicates per group, pooled from four or five mice per group and two independent experiments).

P < 0.05, **P < 0.01, ***P < 0.001, and ****P < 0.0001* by one-way ANOVA with Tukey's multiple comparisons tests (B**, **D**, **F**). Data are shown as the means ± SEM.

Figure S4. PMN-derived MPO mediates alterations of mitochondrial signaling in AMs

MPO-induced impairment of antibacterial defense is mediated by UCP2

Clearing apoptotic PMNs rendered AMs unable to increase their MMP and consecutively produce mtROS in response to bacteria, while enhancing mitochondrial respiration. Uncoupling proteins have been shown to dissipate the proton gradient across the inner mitochondrial membrane, leading to reduced MMP and mtROS production (133, 211). To determine if UCP2, expressed in lung and AMs (212, 213), plays a role in MPO-induced mitochondrial reprogramming, we used the UCP2 inhibitor genipin (GNP). Following MPO pre-treatment, GNP restored mtROS production in AMs stimulated with PA and *K. pneumoniae* (KP) in vitro (Fig. 12, A and B). GNP also reinstated mtROS generation in AMs isolated 24h after acid aspiration when challenged with bacteria *ex vivo* (Fig. 12C). We then used *Ucp2*$^{-/-}$ AMs, exposed them to apoptotic WT PMNs for efferocytosis *in vitro*, and found that they still responded with mtROS production upon bacterial challenge (Fig. 12D). In *Ucp2*$^{-/-}$ AMs, MPO pre-treatment did not prevent an increase in MMP in response to bacteria (Fig. 12E) and did not hinder bacterial killing *in vitro* (Fig. 12F). Furthermore, OCR did not increase after MPO pre-treatment when UCP2-deficient AMs were exposed to bacteria (Fig. 12G). Inhibiting UCP2 with GNP restored IL-1β and IL-6 release but not TNFα in MPO-pretreated AMs of WT mice *in vitro* (Fig. 12H). IL-10 secretion also remained unaffected (Fig. 12I). Thus, MPO-induced impairment of mtROS production in bacteria-challenged AMs is dependent on UCP2 function. We hypothesized that MPO might alter UCP2 levels in AMs. Although we did not observe transcriptional upregulation of UCP2 during acid-induced inflammation *in vivo* or efferocytosis *in vitro* (Fig. 12J), UCP2 protein levels were elevated in AMs harvested 24h after acid aspiration compared to sham-treated animals (Fig. 12K). Consistent with this finding, *in vitro* stimulation of AMs with MPO increased UCP2 expression (Fig. 12L). This upregulation relied on MPO's enzymatic activity, as its inhibition and ROS scavenging with antioxidants normalized UCP2 levels (Fig. 12M). To validate our findings *in vivo*, we treated mice 24h after acid aspiration with GNP or a carrier control i.t. and subsequently infected them with PA (Fig. 12N). Consistent with our *ex vivo* and *in vitro* data, mice that received GNP exhibited lower bacterial counts in BALF compared to controls (Fig. 12O). Notably, GNP did not affect bacterial growth *in vitro* or in mice infected with PA *in vivo* (Fig. 12P). Additionally, GNP did not impair phagocytosis or bacterial killing by AMs (Fig. 12, F and Q).

Collectively, these findings indicate that PMN-derived MPO elevates UCP2 expression in AMs, increasing oxygen consumption during bacterial stimulation while suppressing mtROS production, bacterial eradication, and cytokine secretion.

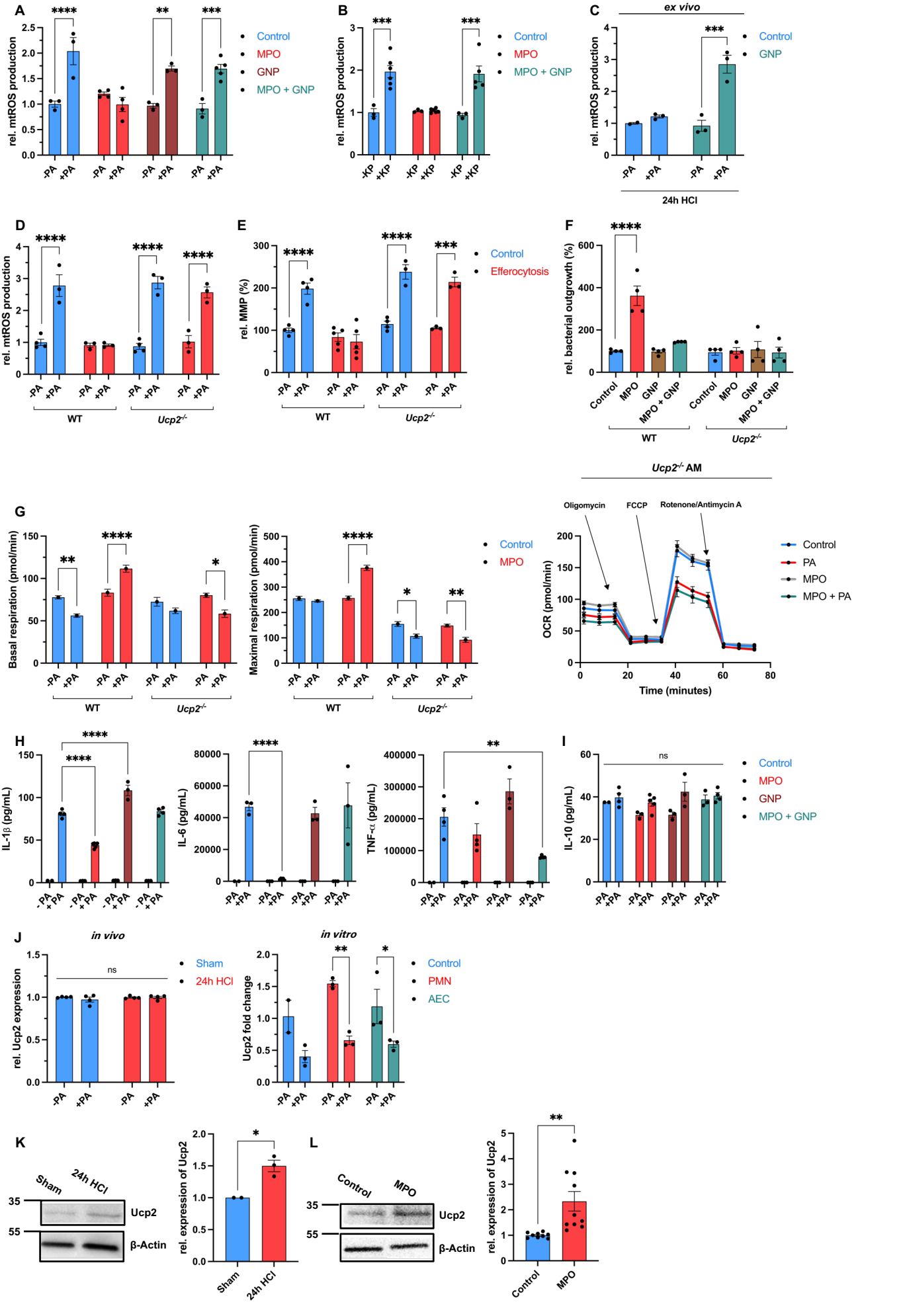
A
rel. mtROS production
Control
MPO
GNP
MPO + GNP
-PA
+PA
B
rel. mtROS production
-KP
+KP
C
ex vivo
rel. mtROS production
24h HCl
D
rel. mtROS production
WT
Ucp2-/-
E
rel. MMP (%)
Efferocytosis
F
rel. bacterial outgrowth (%)
G
Basal respiration (pmol/min)
Maximal respiration (pmol/min)
Ucp2-/- AM
Oligomycin
FCCP
Rotenone/Antimycin A
OCR (pmol/min)
Time (minutes)
PA
MPO + PA
H
IL-1β (pg/mL)
IL-6 (pg/mL)
TNF-α (pg/mL)
I
IL-10 (pg/mL)
ns
J
in vivo
in vitro
rel. Ucp2 expression
Ucp2 fold change
Sham
24h HCl
PMN
AEC
K
Sham
24h HCl
Ucp2
β-Actin
rel. expression of Ucp2
L
Control
MPO

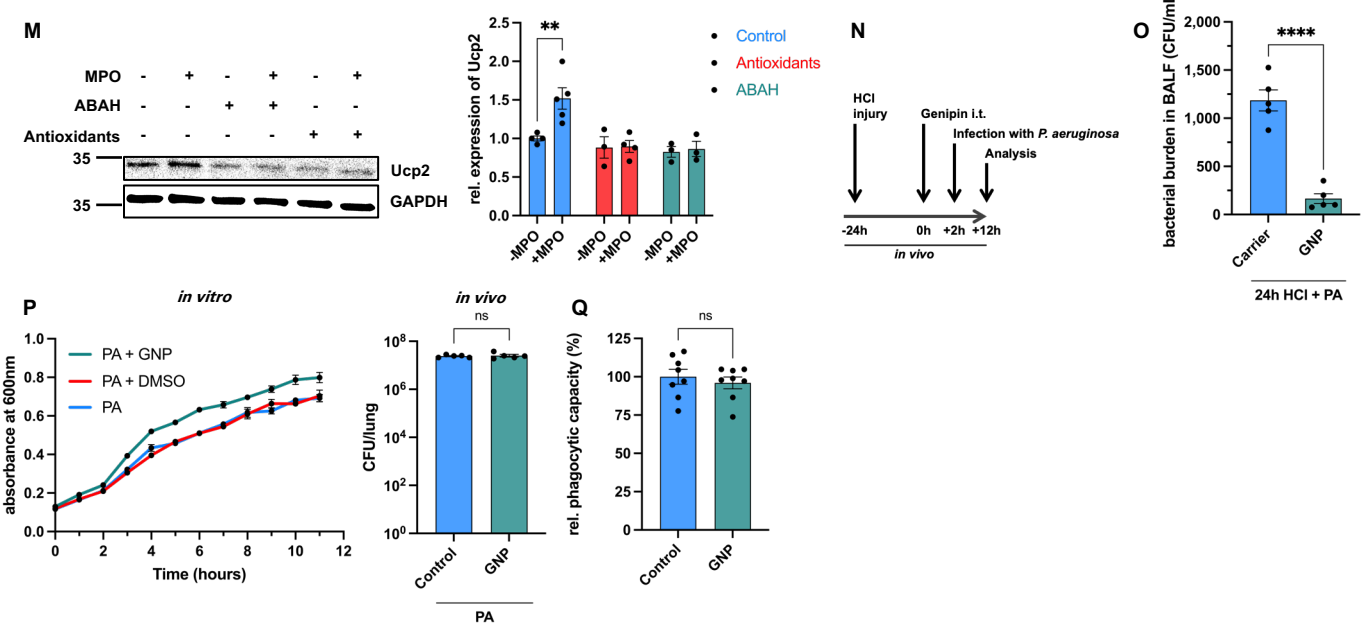
M
MPO - + - + - +
ABAH - - + + - -
Antioxidants - - - - + +
35
Ucp2
35
GAPDH
rel. expression of Ucp2
**
-MPO +MPO -MPO +MPO -MPO +MPO
Control
Antioxidants
ABAH
N
HCl injury
Genipin i.t.
Infection with P. aeruginosa
Analysis
-24h 0h +2h +12h
in vivo
O
bacterial burden in BALF (CFU/mL)
****
Carrier GNP
24h HCl + PA
P
in vitro
PA + GNP
PA + DMSO
PA
absorbance at 600nm
Time (hours)
in vivo
ns
CFU/lung
Control GNP
PA
Q
ns
rel. phagocytic capacity (%)
Control GNP

Fig. 12. MPO stabilizes UCP2 to preclude mtROS generation in AMs during bacterial challenge

(**A**) mtROS production in AMs pretreated with MPO +/− GNP in response to PA (n = 3 to 5 replicates per group, pooled from three or four mice per group and two independent experiments).

(**B**) mtROS production in AMs after pre-treatment with MPO +/- genipin (GNP) in response to K. pneumoniae (KP) (n=3-6 replicates/group, pooled from 3-5 mice/group and two independent experiments).

(**C**) Ex vivo mtROS measurement in AMs 24h after acid aspiration +/− GNP in response to PA (n = 3 replicates per group, pooled from five mice per group and two independent experiments).

(**D**) mtROS measurement in WT or *Ucp2*$^{-/-}$ AMs after efferocytosis of apoptotic PMNs in response to PA (n = 3 or 4 replicates per group, pooled from three mice per group and two independent experiments).

(**E**) MMP measurement of WT or *Ucp2*$^{-/-}$ AMs after efferocytosis of PMNs in response to PA (n = 3 to 5 replicates per group, pooled from three or four mice per group and two independent experiments).

(**F**) Bacterial killing capacity (PA) of WT or *Ucp2*$^{-/-}$ AMs +/− MPO +/− GNP (n = 4 to 8 replicates per group, pooled from three to six mice per group and two independent experiments).

(**G**) OCR of WT and *Ucp2*$^{-/-}$ AMs +/− MPO in response to PA (n = 4 to 10 replicates per group, pooled from four to seven mice per group and two independent experiments).

(**H** and **I**) Release of IL-1β (**H**: left), IL-6 (**H**: middle), TNF-α (**H**: right), and IL-10 (**I**) in response to PA after pre-treatment with MPO +/- GNP (n=3-5 replicates/group, pooled from 3-4 mice/group and two independent experiments).

(**J**) Transcriptional regulation of UCP2 at different time points after acid aspiration + PA for 3h *in vivo* (data obtained from Microarray analysis) (left) and after efferocytosis of apoptotic PMNs or AECs + PA *in vitro* (qPCR) (right) (right: n=3 replicates/group, pooled from 5 mice/group and two independent experiments).

(**K**) Western blot of UCP2 and β-actin in AMs 24h after acid aspiration compared to sham treatment (n = 3 replicates per group, pooled from 15 to 20 mice per group and two independent experiments).

(**L**) Western blot of UCP2 and β-actin in AMs +/− MPO (n = 10 replicates per group, pooled from 30 mice per group and three independent experiments).

(**M**) Western blot of UCP2 and GAPDH in AMs treated with MPO in presence of ABAH or antioxidants (N-acetyl-L-cystein and α-D-Tocopherolsuccinate) (n=3-5 replicates/group, pooled from 10-15 mice/group and two independent experiments).

(**N**) Experimental scheme for (L).

(**O**) Bacterial burden in BALF 24 hours after acid aspiration and successive intratracheal instillation of GNP followed by in vivo infection with PA (n = 5 mice per group, pooled from two independent experiments).

(**E**) Bacterial growth curves of PA in presence of GNP, control (DMSO), or untreated (left); Bacterial burden in lung after intratracheal instillation of GNP 300μM for 2h compared to control (DMSO) and subsequent infection with PA for 12h *in vivo* (right) (left: n=3 replicates/group; right: n=5 mice/group).

(**F**) Relative phagocytic capacity of AMs (incubation with PA for 1h) after treatment with GNP (n=8 replicates/group, pooled from 5 mice/group and two independent experiments).

*P < 0.05, **P < 0.01, ***P < 0.001, and ****P < 0.0001 by Student's t test (**K** and **L**, **O** to **Q**), two-way ANOVA (**A** to **C**, **H** to **J, M**), or three-way ANOVA with Šídák's multiple comparisons test (**D** to **G**). Data are shown as the means ± SEM.

MPO-induced UCP2 expression drives canonical glutaminolysis to impair antibacterial defense in AMs

Emerging evidence highlights UCP2's role as a metabolic hub that governs the relative contribution of substrates oxidized by mitochondria, with its metabolic activity leading to a reduction in mtROS generation rather than pure uncoupling (214-217). UCP2 promotes the oxidation of fatty acids and glutamine while reducing the oxidation of glucose-derived pyruvate (Fig. 13A). Given that MPO pre-treatment increased the OCR via UCP2 in response to bacteria, we investigated whether specific fueling of the tricarboxylic acid (TCA) cycle might be involved. Analyzing maximum mitochondrial respiration in presence of pathway-specific inhibitors (substrate oxidation stress test) demonstrated a relative increase in glutaminolysis and, conversely, a relative decrease in glycolysis in AMs treated with PA plus MPO compared to PA alone, while fatty acid oxidation remained unaltered (Fig. 13B). Inhibition of glutaminolysis using BPTES, a glutaminase-1 inhibitor, completely blocked the increase in maximal respiration due to MPO in presence of bacteria *in vitro* (Fig. 13C). Furthermore, wildtype AMs that were pre-treated with MPO and stimulated with bacteria showed heightened glutamine consumption and increased intracellular levels of glutamate, whereas intracellular levels of glutamine were unchanged compared to the control (Fig. 13D). Additionally, MPO pre-treated AMs exhibited reduced lactate release and glucose consumption in the presence of bacteria (Fig. 13, E and F). These MPO-mediated metabolic changes were absent in UCP2-deficient AMs (Fig. 13, D to F). Accordingly, inhibition of glutaminolysis reversed the MPO-mediated mtROS production impairment during bacterial exposure (Fig. 13G). Similarly, the inhibitory effect of PMN efferocytosis on the release of the mtROS-dependent cytokine IL-1β in response to bacteria was partially reversed after glutaminolysis inhibition (Fig. 13H), whereas IL-10 secretion was reduced (Fig. 13I). Canonical glutaminolysis depends on the enzymatic activity of glutamate dehydrogenase (GLUD1), which converts glutamate into αKG to fuel the TCA cycle. Treating AMs with the GLUD1-inhibitor epigallocatechin gallate (EGCG) after pre-treatment with MPO restored mtROS production (Fig. 13J) and the increase in MMP (Fig. 13K) in response to PA. Dimethyl-α-KG (DM-αKG) is a cell-permeable αKG analog. Treating AMs with GNP plus DM-αKG reversed the MPO-mediated suppression of mtROS secretion (Fig. 13L), allowed an increase in MMP in response to bacteria (Fig. 13M), and normalized the ability to kill bacteria (Fig. 13N).

In summary, MPO-induced UCP2 expression enhances the efficient oxidation of glutamine via canonical glutaminolysis when bacteria are present, resulting in AMs being unable to boost their mtROS production, which hinders bacterial killing and affects mtROS-dependent cytokine release.

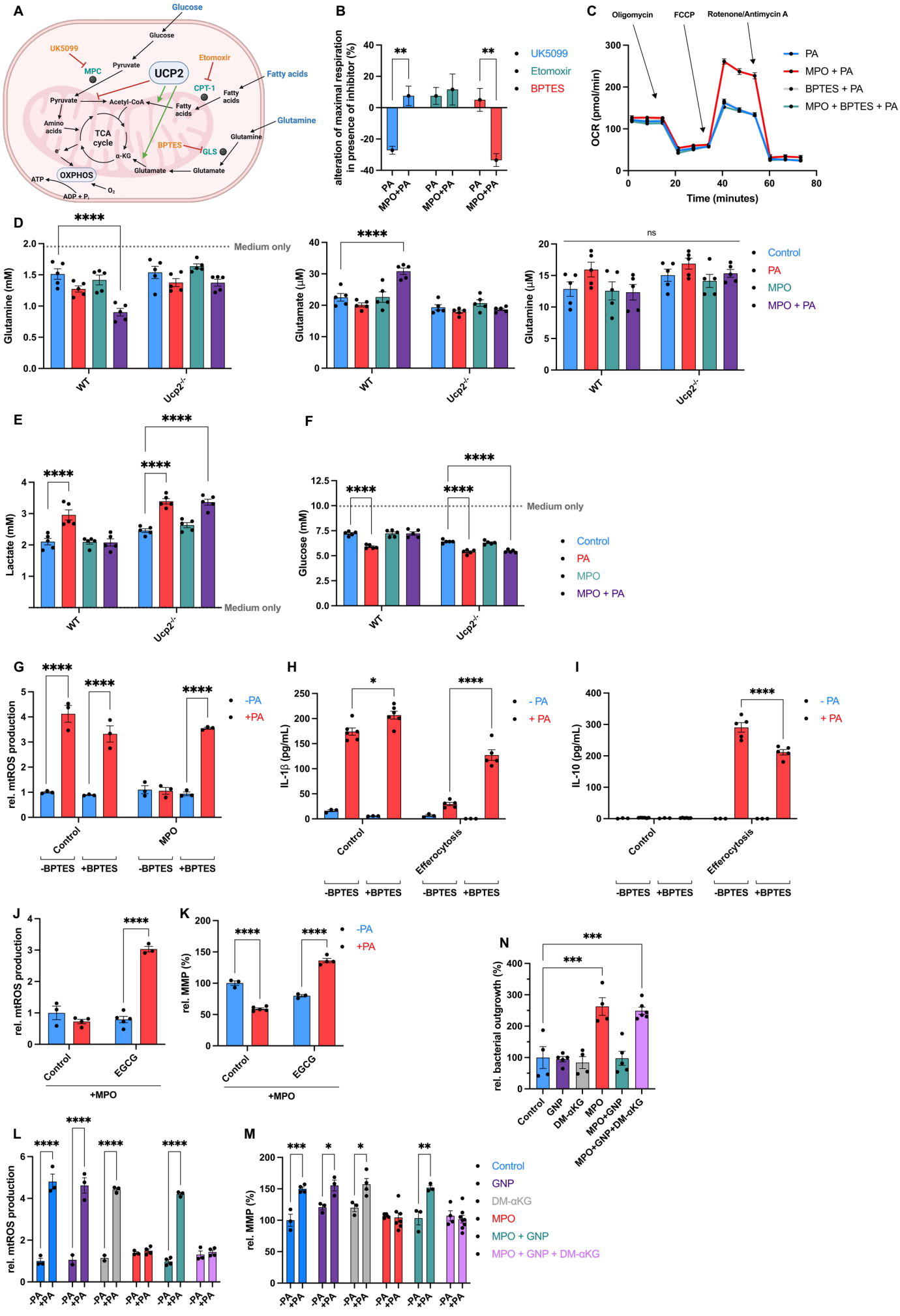
A
Glucose
Glucose
UK5099
MPC
Pyruvate
UCP2
Etomoxir
CPT-1
Fatty acids
Pyruvate
Acetyl-CoA
Fatty acids
Fatty acids
Amino acids
TCA cycle
Glutamine
Glutamine
e-
α-KG
BPTES
GLS
Glutamate
Glutamate
OXPHOS
ATP
O2
ADP + Pi
B
alteration of maximal respiration in presence of inhibitor (%)
**
**
PA
MPO+PA
PA
MPO+PA
PA
MPO+PA
UK5099
Etomoxir
BPTES
C
Oligomycin
FCCP
Rotenone/Antimycin A
OCR (pmol/min)
Time (minutes)
PA
MPO + PA
BPTES + PA
MPO + BPTES + PA
D
Glutamine (mM)
Medium only
Glutamate (µM)
Glutamine (µM)
ns
WT
Ucp2-/-
Control
PA
MPO
MPO + PA
E
Lactate (mM)
Medium only
F
Glucose (mM)
Medium only
G
rel. mtROS production
-PA
+PA
Control
MPO
-BPTES
+BPTES
-BPTES
+BPTES
H
IL-1β (pg/mL)
- PA
+ PA
Control
Efferocytosis
-BPTES
+BPTES
-BPTES
+BPTES
I
IL-10 (pg/mL)
- PA
+ PA
Control
Efferocytosis
-BPTES
+BPTES
-BPTES
+BPTES
J
rel. mtROS production
Control
EGCG
+MPO
K
rel. MMP (%)
-PA
+PA
Control
EGCG
+MPO
N
rel. bacterial outgrowth (%)
Control
GNP
DM-αKG
MPO
MPO+GNP
MPO+GNP+DM-αKG
L
rel. mtROS production
-PA
+PA
M
rel. MMP (%)
-PA
+PA
Control
GNP
DM-αKG
MPO
MPO + GNP
MPO + GNP + DM-αKG

Fig. 13. UCP2 promotes canonical glutaminolysis to compromise bacterial defense in AMs

(**A**) Diagram of UCP2-mediated rewiring of mitochondrial metabolism. Pathway-specific inhibitors are highlighted in orange; corresponding enzymes are highlighted in green (MPC= mitochondrial pyruvate carrier; CPT-1=carnitine palmitoyltransferase 1; GLS=glutaminase); pathway substrates are highlighted in blue. *Created with BioRender.com

(**B**) Substrate oxidation stress test (extracellular flux (XF) assay): Data are displayed as alteration of maximal respiration in the presence of pathway inhibitors, namely UK5099 for glycolysis, etomoxir for fatty acid oxidation, and BPTES for glutaminolysis compared with respective uninhibited control in AMs +/− MPO and in response to PA (n = 7 to 9 replicates per group, pooled from six to eight mice per group and two independent experiments).

(**C**) OCR of AMs +/− MPO followed by BPTES in response to PA (n = 5 replicates per group, pooled from four mice per group and two independent experiments).

(**D**) Luminometric assessment of glutamine consumption by and intracellular concentration of glutamate and glutamine in WT or *Ucp2*$^{-/-}$ AMs +/− MPO in response to PA (n = 5 replicates per group, pooled from four mice per group and two independent experiments).

(**E** and **F**) Luminometric assessment of Lactate secretion (**A**) and glucose consumption (**B**) by AMs from WT or *Ucp2*$^{-/-}$ mice after pre-treatment with MPO in response to PA (n=5 replicates/group, pooled from 4 mice/group and two independent experiments).

(**G**) mtROS measurement in AMs +/− MPO +/− BPTES in response to PA (n = 3 replicates per group, pooled from three mice per group and two independent experiments).

(**H** and **I**) IL-1β (**H**) and IL-10 (**I**) secretion of AMs after efferocytosis of apoptotic PMNs +/- BPTES in response to PA (n=3-6 replicates/group, pooled from 3-5 mice/group and two independent experiments).

(**J** and **K**) mtROS production by (**J**) and MMP of (**K**) AMs after pre-treatment with MPO +/- EGCG in response to PA (n=3-5 replicates/group, pooled from 3-4 mice/group and two independent experiments).

(**L**) mtROS measurement in AMs +/− MPO +/− GNP and, concomitantly, +/− DM-α-KG (αKG) in response to PA (n = 3 or 4 replicates per group, pooled from four mice per group and two independent experiments).

(**M**) MMP measurement in AMs +/− MPO +/− GNP and, concomitantly, +/− αKG in response to PA (n = 3 to 7 replicates per group, pooled from four to seven mice per group and two independent experiments).

(**N**) Bacterial killing capacity (PA) of AMs +/− MPO +/− GNP and, concomitantly, +/− αKG in response to PA (n = 3 to 6 replicates per group, pooled from four to six mice per group and two independent experiments).

*P < 0.05, **P < 0.01, ***P < 0.001, and ****P < 0.0001 by one-way ANOVA with Tukey's multiple comparisons test (**N**) or two-way ANOVA (**B**, **J** and **M**) and three-way ANOVA (**D** to **I**) with Šídák's multiple comparisons test. Data are shown as the means ± SEM.

MPO primes hAMs through UCP2 to blunt bacterial response

Next, we investigated whether MPO-induced immunometabolic alterations are restricted to murine AMs or also apply to hAMs isolated from BALF of patients with uninflamed lungs. Like murine macrophages, hAMs failed to produce mtROS in response to bacteria after MPO pre-stimulation. Moreover, GNP prevented MPO-mediated impairment of mtROS generation, whereas αKG restored MPO-mediated effects in the presence of GNP (Fig. 14A). Furthermore, human IL-1β secretion was reduced in response to bacteria after MPO pre-treatment, whereas human IL-6 was not affected (Fig. 14B). In line with our findings in murine macrophages, MPO did not influence TNF-α (Fig. 14B) or IL-10 release (Fig. 14C), but efferocytosis of neutrophils clearly induced IL-10 secretion in hAMs secondary to stimulation with PA (Fig. 14C).
Thus, MPO is a conserved signal in AMs across species that blunts antibacterial responses via UCP2.

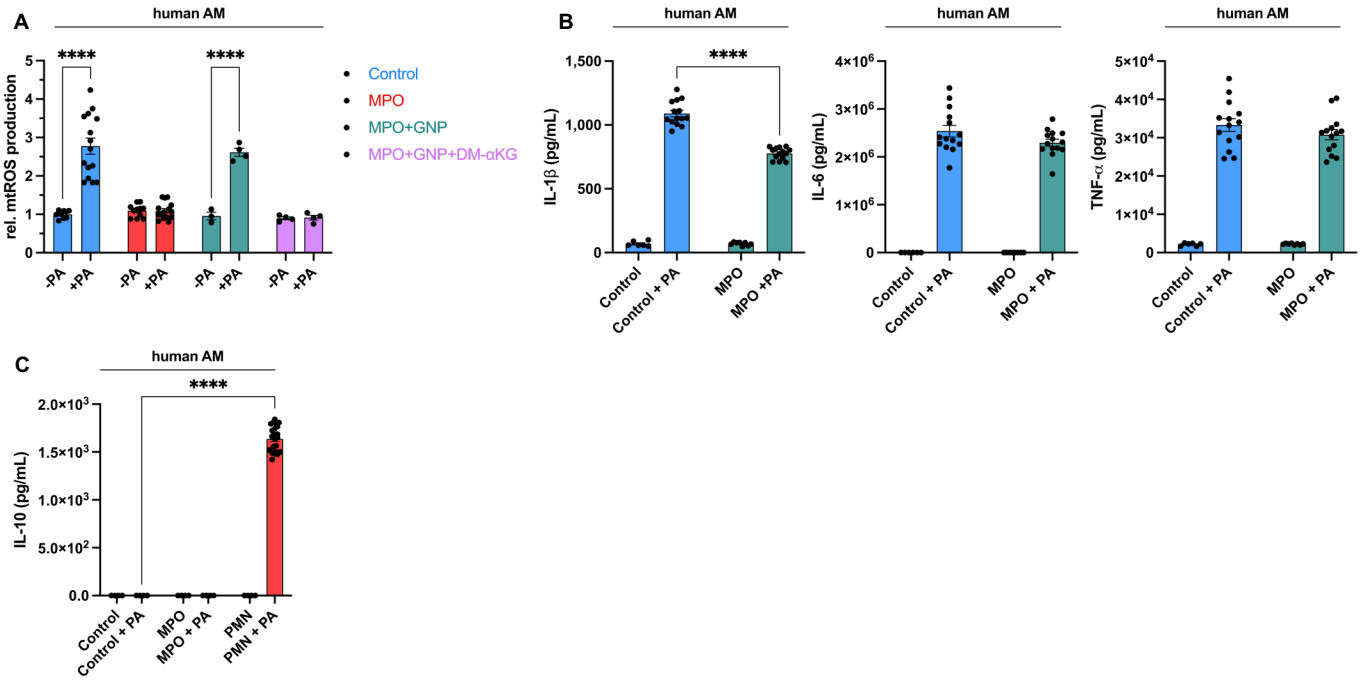
A
human AM
rel. mtROS production
****
****
-PA
+PA
Control
MPO
MPO+GNP
MPO+GNP+DM-αKG
B
human AM
IL-1β (pg/mL)
IL-6 (pg/mL)
TNF-α (pg/mL)
Control
Control + PA
MPO
MPO +PA
MPO + PA

C
human AM
IL-10 (pg/mL)
****
Control
Control + PA
MPO
MPO + PA
PMN
PMN + PA

Fig. 14. MPO impairs bactericidal properties via UCP2 in hAMs

(A) mtROS measurement in hAMs +/− MPO +/− GNP and, concomitantly, +/− αKG in response to PA (n = 3 to 15 replicates per group, pooled from four patients and four independent experiments).

(B) Secretion of IL-1β (top left), IL-6 (top right), and TNF-α (bottom) of hAMs after pre-treatment with MPO in response to PA (n=6-14 replicates/group, pooled from four patients and three independent experiments).

(C) Secretion of IL-10 of hAMs after pre-treatment with MPO or apoptotic PMN in response to PA for 6-8 hours (n=4-24 replicates/group, pooled from four patients and three independent experiments).

*P < 0.05, **P < 0.01, ***P < 0.001, ****P < 0.0001 by two-way ANOVA with Šídák's multiple comparisons test (A to C). Data are shown as the means ± s.e.m.

MPO promotes continued efferocytosis through UCP2 while restricting bacterial control *in vivo* and across species

Efferocytosis enhances the continued uptake of apoptotic cells, a process known as "continued or continual efferocytosis" (176-178). In support of this, we observed that AMs showed an increased ability to ingest apoptotic PMNs during the resolution phase of inflammation, particularly 24h after acid instillation (Fig. 15A). Since UCP2 is known to lower MMP to promote the ongoing clearance of apoptotic cells in macrophages (177), we assessed the effect of cell type-specific efferocytosis within the framework of an altered MMP due to bacterial stimulation (Fig. 15B). As anticipated, efferocytosis of both PMNs and AECs enhanced the ingestion of apoptotic PMNs during a subsequent round of efferocytosis in AMs (Fig. 15C, as depicted by the blue bars). Interestingly, stimulation with bacteria following the initial round of efferocytosis with AECs, and in control AMs that did not undergo efferocytosis, reduced the uptake of apoptotic PMNs in the subsequent or initial round, respectively (Fig. 16C, left and right red bars). In stark contrast, PMN efferocytosis triggered a self-perpetuating cycle of continued efferocytosis despite bacterial presence, as indicated by a persistent level of efferocytosis in the second round (Fig. 15C, middle red bar). These findings were validated through confocal microscopy (Fig. 15, D and E). Given that MPO increases UCP2 expression, we hypothesized that MPO could promote continued efferocytosis. Indeed, MPO alone replicated the effects of PMN efferocytosis in the presence of bacteria during the second round of apoptotic cell uptake (Fig. 15F). Notably, *Ucp2*$^{-/-}$ AMs did not exhibit enhanced efferocytosis in response to MPO (Fig. 15G). Human AMs increased their ingestion of apoptotic PMNs following MPO treatment (Fig. 15H). To validate our results *in vivo*, we conducted acid aspiration followed by a secondary bacterial pneumonia with PA for 10h, with or without i.t. pre-treatment with GNP (Fig. 15I). Consistent with our *in vitro* and *ex vivo* data, GNP pre-treatment led to an increase in the number of apoptotic cells per lung surface area compared to control (Fig. 15J). To examine the impact of these findings on disease outcomes in clinically relevant models, we performed second-hit models using acid aspiration or IAV infection as the primary insult, followed by secondary bacterial pneumonia during inflammation resolution with PA or Spn, respectively (Fig. 15, I and L). GNP pre-treatment restored bacterial control during secondary PA infection following acid aspiration and improved survival in the same model (Fig. 12N and Fig. 15K). Similarly, GNP pre-treatment

significantly reduced bacterial load when mice were superinfected with Spn during IAV pneumonia (Fig. 15M), consequently enhancing survival in this model (Fig. 15N).

These results underscore the vital role of tissue-resident AMs in bacterial control to prevent invasive infections. In conclusion, neutrophil-derived MPO facilitates the continued clearance of apoptotic cells across species while restricting bacterial control in vivo through a UCP2-regulated immunometabolic reprogramming.

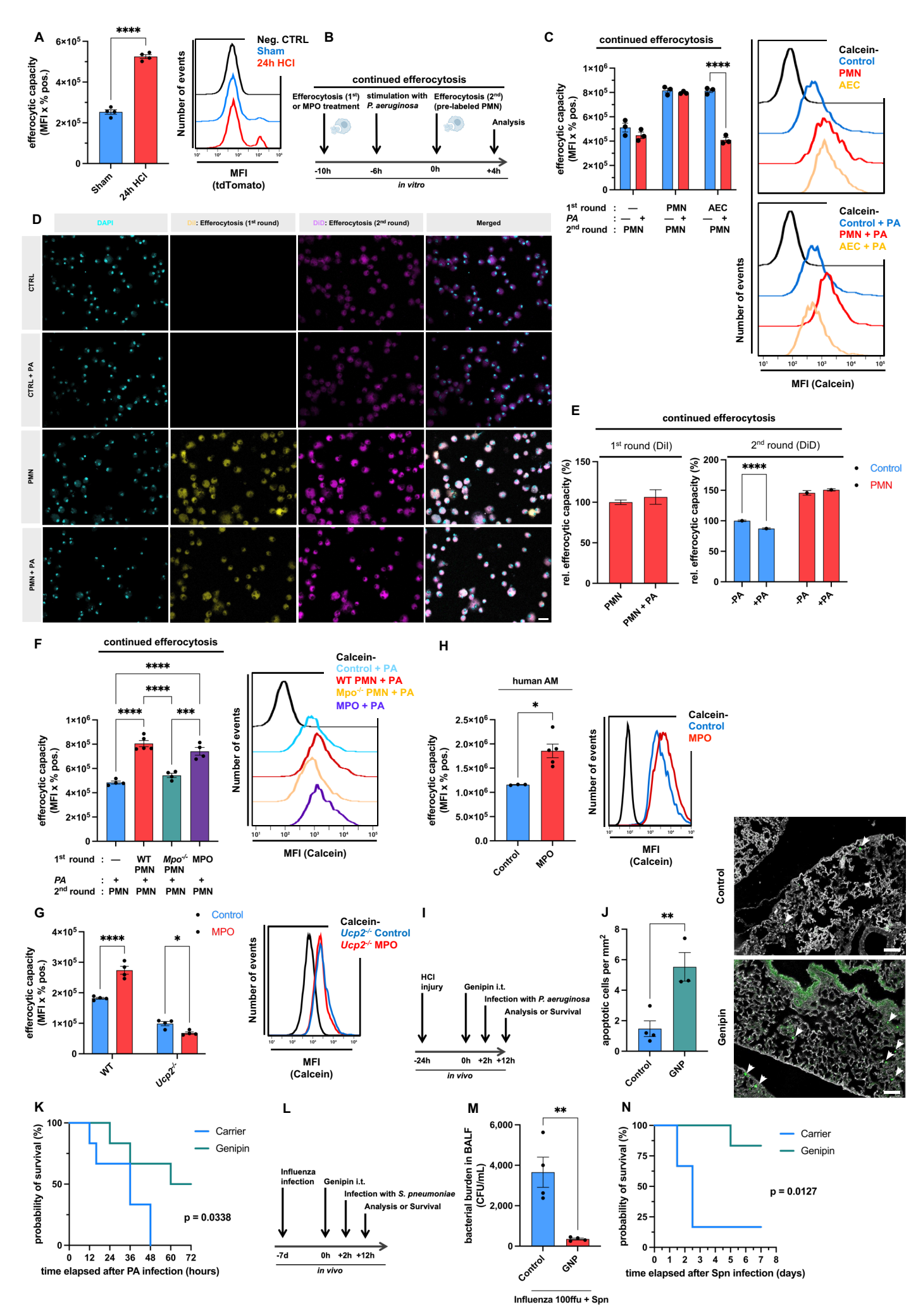
A
efferocytic capacity (MFI x % pos.)
Sham
24h HCl
Number of events
Neg. CTRL
Sham
24h HCl
MFI (tdTomato)
B
continued efferocytosis
Efferocytosis (1st) or MPO treatment
stimulation with P. aeruginosa
Efferocytosis (2nd) (pre-labeled PMN)
Analysis
-10h
-6h
0h
+4h
in vitro
C
continued efferocytosis
efferocytic capacity (MFI x % pos.)
1st round
PA
2nd round
PMN
AEC
Calcein-
Control
PMN
AEC
Control + PA
PMN + PA
AEC + PA
Number of events
MFI (Calcein)
D
DAPI
DiI: Efferocytosis (1st round)
DiD: Efferocytosis (2nd round)
Merged
CTRL
CTRL + PA
PMN
PMN + PA
E
continued efferocytosis
1st round (DiI)
2nd round (DiD)
rel. efferocytic capacity (%)
Control
PMN
-PA
+PA
F
continued efferocytosis
efferocytic capacity (MFI x % pos.)
1st round
PA
2nd round
WT PMN
Mpo-/- PMN
MPO
Calcein-
Control + PA
WT PMN + PA
Mpo-/- PMN + PA
MPO + PA
Number of events
MFI (Calcein)
H
human AM
efferocytic capacity (MFI x % pos.)
Control
MPO
Calcein-
Control
MPO
Number of events
MFI (Calcein)
G
Control
MPO
efferocytic capacity (MFI x % pos.)
WT
Ucp2-/-
Calcein-
Ucp2-/- Control
Ucp2-/- MPO
Number of events
MFI (Calcein)
I
HCl injury
Genipin i.t.
Infection with P. aeruginosa
Analysis or Survival
-24h
0h
+2h
+12h
in vivo
J
apoptotic cells per mm2
Control
GNP
Control
Genipin
K
probability of survival (%)
Carrier
Genipin
p = 0.0338
time elapsed after PA infection (hours)
L
Influenza infection
Genipin i.t.
Infection with S. pneumoniae
Analysis or Survival
-7d
0h
+2h
+12h
in vivo
M
bacterial burden in BALF (CFU/mL)
Control
GNP
Influenza 100ffu + Spn
N
probability of survival (%)
Carrier
Genipin
p = 0.0127
time elapsed after Spn infection (days)

Fig. 15. MPO promotes continual efferocytosis via UCP2 while impairing bacterial control in vivo and across species

(**A**) *Ex vivo* flow-cytometric analysis of efferocytosis of tdTomato-labeled apoptotic PMNs by AMs 24 hours after acid aspiration with a representative flow panel (n = 4 replicates per group, pooled from four to six mice per group and two independent experiments).

(**B**) Experimental scheme for (C to F). *Created with BioRender.com

(**C**) AMs were incubated with apoptotic PMNs or AECs compared with control (first round) without (blue bars) or with (red bars) PA before AMs of all conditions were incubated with stained apoptotic PMNs (calcein) to determine the efferocytic capacity by flow cytometry with a representative flow panel (n = 3 replicates per group, pooled from four mice per group and two independent experiments).

(**D** and **E**) Efferocytic uptake of AMs *in vitro* determined by confocal microscopy. AMs were co-incubated with pre-labeled apoptotic PMNs (DiI; efferocytosis 1st round) compared to control (no efferocytosis) and subsequently stimulated with PA (+PA) in comparison to no stimulation (-PA) before all conditions received pre-labeled apoptotic PMNs (DiD; efferocytosis 2nd round) to quantify efferocytic uptake (n=5 mice/group, pooled from two independent experiments):

(**D**) Exemplary graphical depiction:

Nuclei=DAPI, apoptotic pre-labeled PMNs=DiI (1st round) and DiD (2nd round).

(**E**) Statistical quantification of continued efferocytosis:

Efferocytic capacity during 1^{st} and 2^{nd} round of efferocytosis

(**F**) AMs were incubated with WT or *Mpo*$^{-/-}$ PMNs compared with control +/− MPO and subsequently stimulated with PA, followed by incubation with stained apoptotic PMNs (calcein) to determine the efferocytic capacity by flow cytometry with a representative flow panel (n = 3 to 7 replicates per group, pooled from four to eight mice per group and two independent experiments).

(**G**) WT or *Ucp2*$^{-/-}$ AMs +/− MPO were subsequently incubated with stained apoptotic PMNs (calcein) to determine the efferocytic capacity by flow cytometry with a representative flow panel (n = 4 replicates per group, pooled from five mice per group and two independent experiments).

(**H**) Human AMs +/− MPO before incubating all samples with stained apoptotic human PMNs (calcein) to determine the efferocytic capacity with a representative flow panel (n = 3 to 5 replicates per group, pooled analysis from four patients and four independent experiments).

(**I**) Experimental scheme for (J) and (K). *Created with BioRender.com

(**J**) Left: quantification of TUNEL (terminal deoxynucleotidyltransferase–mediated deoxyuridine triphosphate nick end labeling)–positive apoptotic cells; right: TUNEL-positive apoptotic cells (white arrowheads). Representative images are depicted (scale bars, 50 μM; n = 3 or 4 mice per group, pooled from two independent experiments).

(**K**) Survival analysis after treatment as depicted in (I) (n = 6 mice per group, pooled from two independent experiments).

(**L**) Experimental scheme for (M) and (N). *Created with BioRender.com

(**M**) Bacterial outgrowth in BALF 7 days after influenza infection followed by treatment with GNP intratracheally and subsequent bacterial infection with S. pneumoniae (Spn) (n = 4 mice per group, pooled from two independent experiments).

(**N**) Survival analysis after treatment as depicted in (L) (n = 6 mice per group, pooled from two independent experiments).

*P < 0.05, **P < 0.01, ***P < 0.001, and ****P < 0.0001 by Student's t test (**A**, **E** (left), **H**, **J**, **M**), one-way ANOVA with Dunnett's multiple comparisons test (**F**), or two-way ANOVA with Šídák's multiple comparisons test (**C**, **E** (right), **G**). Survival distributions were followed up by a log-rank test (Mantel-Cox test) (**K** and **N**). Data are shown as the means ± SEM.

Discussion

Macrophages are essential in managing inflammation and its resolution by swiftly adapting to different functional phenotypes. However, the *in vivo* mechanisms that regulate potentially diverging macrophage functions, such as antibacterial defense versus resolution and repair, remain incompletely understood. In our study, through an unbiased *in vivo* approach, we discovered that neutrophil efferocytosis shifts AMs towards a pro-resolution phenotype by reprogramming mitochondrial metabolism in an UCP2-dependent manner, albeit at the cost of reduced bacterial control. UCP2 has been shown to exert mild uncoupling effects by increasing proton conductance across the inner mitochondrial membrane of the respiratory chain upon specific activation, thereby reducing mitochondrial reactive oxygen species (mtROS) release (133, 148, 211). However, emerging evidence underscores UCP2's role as a metabolic carrier (214-217). Specifically, UCP2 has been shown to export C4-metabolites from the mitochondria, thereby limiting the oxidation of glucose-derived acetyl-CoA while promoting fatty acid oxidation and glutaminolysis (217). By exporting C4-compounds, UCP2 decreases redox pressure on the ETC, subsequently reducing mtROS release (217). In our study, increased UCP2 expression in macrophages due to MPO activity prevents hyperpolarization of the MMP and subsequent mtROS generation in response to bacterial challenges. This effect can be counteracted by inhibiting canonical glutaminolysis. Furthermore, a mitochondrial substrate oxidation stress test and UCP2-dependent increases in glutamine consumption following MPO stimulation during bacterial challenge highlighted the role of UCP2-promoted glutaminolysis in AMs. Therefore, we propose that metabolic regulation mediated by UCP2 is crucial in this context. The increased expression of UCP2 induced by myeloperoxidase (MPO) *in vitro* or during the resolution of ALI *ex vivo* was not correlated with increased UCP2 transcript levels, consistent with prior findings (212, 213, 218). This aligns with observations that UCP2 has an unusually short half-life (218) and is subject to translational regulation by glutamine, facilitating its rapid upregulation (216). Thus, it is plausible that the increased uptake of glutamine, driven by bacterial presence following MPO stimulation, enhances UCP2 expression. Additionally, we observed that MPO's enzymatic activity is essential for elevating UCP2 protein levels, while this upregulation can be prevented by antioxidants. This suggests that the ROS-induced oxidation of UCP2, or its indirect

upregulation as a cellular response to oxidative stress, plays a crucial role in this process. However, the specific mechanisms controlling UCP2 expression, degradation, or potential post-translational modifications—particularly by MPO, such as oxidation of cysteine residues—need further investigation. It is well established that the uptake of ACs inhibits pro-inflammatory signaling in macrophages (174, 175). Our findings indicated that cytokine transcriptional regulation and secretion observed *in vivo* and *ex vivo* were largely mirrored by efferocytosis *in vitro*. While the ingestion of apoptotic cells (AECs, Jurkat cells, and PMNs) generally reduced TNF-α production, the clearance of apoptotic PMNs specifically inhibited the secretion of IL-1β and IL-6 in response to bacterial stimuli. Previously, it was reported that electron flux through the ETC and mtROS production trigger IL-1β release via inflammasome activation (142, 207) and activate MAPKs to support IL-6 secretion (208). Correspondingly, scavenging mtROS reduced the secretion of IL-1β and IL-6, while the levels of TNF-α and IL-10 in AMs remained unaffected by bacterial exposure. IL-6 levels were consistently diminished in murine AMs when mtROS generation was reduced, but this effect was not observed in hAMs, reflecting species-specific differences. In contrast, IL-10 secretion by AMs was not directly influenced by MPO or mtROS but was notably observed after PMN efferocytosis during bacterial encounters. The mechanism underlying enhanced anti-inflammatory IL-10 release in this context warrants further investigation. Notably, this aligns with the idea that PMN efferocytosis primes macrophages for resolving inflammation while limiting pro-inflammatory responses to bacteria. As a result, we observed a conserved effect of PMN efferocytosis on immune function, characterized by a shift from pro- to anti-inflammatory cytokines. Importantly, inflammation and resolution occur simultaneously, as the initiation of inflammation also triggers its resolution to avoid excessive responses that could lead to irreversible organ damage. Extensively studied examples, like itaconate and SPMs, are generated during inflammation to promote resolution (85-88, 90-92, 168, 169). On the other hand, persistent or dysfunctional resolution of ALI might lead to tissue injury-induced impaired gas exchange, chronic airway inflammation, or lung fibrosis (155). Resolution can be promoted by enhancing continued efferocytosis, a well-documented, self-reinforcing process (176). In line with this, ingestion of apoptotic PMNs or apoptotic AECs enhanced continued efferocytosis *in vitro*. However, AMs that ingested AECs returned its efferocytic capacity to baseline upon bacterial challenge, whereas PMN efferocytosis maintained high efferocytic capacity in AMs even in the presence of bacteria, in an MPO-induced and UCP2-mediated

manner. Our data support that PMN efferocytosis initiates and drives inflammation resolution (219-221), revealing that the ingestion of apoptotic PMNs prioritizes continual efferocytosis over antibacterial responses, mediated by UCP2 in macrophages. This strategy is logical, as accumulating necrotic PMNs can promote inflammation and tissue damage, whereas clearing MPO from extracellular spaces is anti-inflammatory (222, 223). Interestingly, MPO in PMNs protected mice during sterile endotoxemia and sepsis by limiting the extent of LPS-induced tissue injury and inflammation (224). Applying different mouse models, MPO was found to reduce inflammatory PMN tissue accumulation by attenuating neutrophil migration (225). Although these studies left in-depth mechanisms unresolved, it is tempting to speculate that a functional switch to a pro-resolution/anti-inflammatory state induced by MPO may contribute. MPO is especially intriguing as its receptor- or efferocytosis-mediated uptake by macrophages may aid in antimicrobial defense during early inflammation and later promote resolution to prevent hyperinflammation. In another study, UCP2 was reported to promote repair mechanisms in macrophages in response to alarmin IL-33 in a muscle injury model (94). Thus, different danger signals (e.g., MPO, IL-33) increase UCP2 expression to enhance macrophage resolution properties. Our study highlighted the importance of the identity of apoptotic cells, as AMs were reprogrammed by apoptotic neutrophils in a cell-type-specific manner. Since neutrophils are not common constituents of homeostatic tissue, the appearance of apoptotic PMNs and their unique secreted factors indicates tissue injury (226). It has been shown that the clearance of apoptotic PMNs triggers a tissue-remodeling signature, while the efferocytosis of apoptotic epithelial cells, specifically hepatocytes, promotes a tolerogenic phenotype in liver macrophages/monocytes in an IL-4/IL-13 enriched environment. The removal of apoptotic T-cells only marginally affected IL-4-induced gene expression in liver macrophages/monocytes. The uptake of apoptotic PMNs, but not apoptotic hepatocytes, by liver macrophages/monocytes requires the phosphatidylserine-sensing efferocytic receptors AXL and MERTK (227). Specifically apoptotic PMNs have also been shown to be crucial for promoting proper repair after myocardial infarction (185). On the other hand, specific efferocytosis of apoptotic AECs can initiate lung fibrosis (228). However, our study is the first to provide an in-depth mechanism of cell-type-specific efferocytosis. In summary, we identified a conserved mechanism of MPO-dependent mitochondrial reprogramming that limits macrophage functional plasticity to prioritize tissue protection. These findings held across species and bacterial pathogens. While likely beneficial in most contexts, this opens a

window for colonizing bacteria during inflammation resolution (e.g., aspiration or influenza pneumonia), facilitating invasive infections. With the rising number of clinical trials evaluating apoptotic cell therapies (229-232), our results emphasize the importance of understanding the effects of various apoptotic cell cargos on macrophages. Furthermore, modulating canonical glutaminolysis or UCP2 could offer therapeutic potential to enhance macrophage-driven host defense or repair functions during ALI/ARDS.

References

1. Bauer TT, Ewig S, Rodloff AC, Müller EE. Acute respiratory distress syndrome and pneumonia: a comprehensive review of clinical data. Clin Infect Dis 2006;43:748–56.
2. Bellani G, Laffey JG, Pham T, et al. Epidemiology, Patterns of Care, and Mortality for Patients With Acute Respiratory Distress Syndrome in Intensive Care Units in 50 Countries. JAMA 2016;315:788–800.
3. Matthay MA, Zemans RL, Zimmerman GA, et al. Acute respiratory distress syndrome. Nat Rev Dis Primers 2019;5:18.
4. Torres A, Cilloniz C, Niederman MS, et al. Pneumonia. Nat Rev Dis Primers 2021;7:25.
5. Waldeck F, Lemmel S, Panning M, et al. Comparing viral, bacterial, and coinfections in community-acquired pneumonia, a retrospective cohort study. Int J Infect Dis 2025;154:107841.
6. Jain S, Self WH, Wunderink RG, et al. Community-Acquired Pneumonia Requiring Hospitalization among U.S. Adults. N Engl J Med 2015;373:415–27.
7. Sadikot RT, Blackwell TS, Christman JW, Prince AS. Pathogen-host interactions in Pseudomonas aeruginosa pneumonia. Am J Respir Crit Care Med 2005;171:1209–23.
8. Letourneau AR, Issa NC, Baden LR. Pneumonia in the immunocompromised host. Curr Opin Pulm Med 2014;20:272–9.
9. Ma W, Tang S, Yao P, et al. Advances in acute respiratory distress syndrome: focusing on heterogeneity, pathophysiology, and therapeutic strategies. Signal Transduct Target Ther 2025;10:75.
10. Morens DM, Taubenberger JK, Fauci AS. Predominant Role of Bacterial Pneumonia as a Cause of Death in Pandemic Influenza: Implications for Pandemic Influenza Preparedness. J Infect Dis 2008;198:962–70.
11. Morgan DJ, Casulli J, Chew C, et al. Innate Immune Cell Suppression and the Link With Secondary Lung Bacterial Pneumonia. Front Immunol 2018;9:2943.
12. Manohar P, Loh B, Nachimuthu R, Hua X, Welburn SC, Leptihn S. Secondary Bacterial Infections in Patients With Viral Pneumonia. Front Med (Lausanne) 2020;7:420.
13. Langouët-Astrié C, Oshima K, McMurtry SA, et al. The influenza-injured lung microenvironment promotes MRSA virulence, contributing to severe secondary bacterial pneumonia. Cell Rep 2022;41:111721.
14. Garcia-Vidal C, Sanjuan G, Moreno-García E, et al. Incidence of co-infections and superinfections in hospitalized patients with COVID-19: a retrospective cohort study. Clin Microbiol Infect 2021;27:83–8.
15. Rice TW, Rubinson L, Uyeki TM, et al. Critical illness from 2009 pandemic influenza A virus and bacterial coinfection in the United States. Crit Care Med 2012;40:1487–98.
16. Chertow DS, Memoli MJ. Bacterial coinfection in influenza: a grand rounds review. JAMA 2013;309:275–82.
17. Kollef MH. Ventilator-associated pneumonia. A multivariate analysis. JAMA 1993;270:1965–70.
18. Torres A, Aznar R, Gatell JM, et al. Incidence, risk, and prognosis factors of nosocomial pneumonia in mechanically ventilated patients. Am Rev Respir Dis 1990;142:523–8.
19. Chastre J, Trouillet JL, Vuagnat A, et al. Nosocomial pneumonia in patients with acute respiratory distress syndrome. Am J Respir Crit Care Med 1998;157:1165–72.

20. Markowicz P, Wolff M, Djedaïni K, et al. Multicenter prospective study of ventilator-associated pneumonia during acute respiratory distress syndrome. Incidence, prognosis, and risk factors. ARDS Study Group. Am J Respir Crit Care Med 2000;161:1942–8.
21. Mandell LA, Niederman MS. Aspiration Pneumonia. N Engl J Med 2019;380:651–63.
22. Raghavendran K, Nemzek J, Napolitano LM, Knight PR. Aspiration-induced lung injury. Crit Care Med 2011;39:818–26.
23. Fan E, Brodie D, Slutsky AS. Acute Respiratory Distress Syndrome: Advances in Diagnosis and Treatment. JAMA 2018;319:698–710.
24. Hsia CCW, Hyde DM, Weibel ER. Lung Structure and the Intrinsic Challenges of Gas Exchange. Compr Physiol 2016;6:827–95.
25. Powers KA, Dhamoon AS. StatPearls, Physiology, Pulmonary Ventilation and Perfusion. StatPearls Publishing. Treasure Island (FL), 2025.
26. Petersson J, Glenny RW. Gas exchange and ventilation-perfusion relationships in the lung. Eur Respir J 2014;44:1023–41.
27. Brandt JP, Mandiga P. StatPearls, Histology, Alveolar Cells. StatPearls Publishing. Treasure Island (FL), 2025.
28. Weibel ER. It takes more than cells to make a good lung. Am J Respir Crit Care Med 2013;187:342–6.
29. Knudsen L, Ochs M. The micromechanics of lung alveoli: structure and function of surfactant and tissue components. Histochem Cell Biol 2018;150:661–76.
30. Martin TR, Frevert CW. Innate immunity in the lungs. Proc Am Thorac Soc 2005;2:403–11.
31. Werner JL, Steele C. Innate receptors and cellular defense against pulmonary infections. J Immunol 2014;193:3842–50.
32. Okahashi N, Sumitomo T, Nakata M, Kawabata S. Secondary streptococcal infection following influenza. Microbiol Immunol 2022;66:253–63.
33. Bos LDJ, Ware LB. Acute respiratory distress syndrome: causes, pathophysiology, and phenotypes. Lancet 2022;400:1145–56.
34. Han S, Mallampalli RK. The acute respiratory distress syndrome: from mechanism to translation. J Immunol 2015;194:855–60.
35. Cheng OZ, Palaniyar N. NET balancing: a problem in inflammatory lung diseases. Front Immunol 2013;4:1.
36. Thompson BT, Chambers RC, Liu KD. Acute Respiratory Distress Syndrome. N Engl J Med 2017;377:562–72.
37. Müller-Redetzky HC, Suttorp N, Witzenrath M. Dynamics of pulmonary endothelial barrier function in acute inflammation: mechanisms and therapeutic perspectives. Cell Tissue Res 2014;355:657–73.
38. Berthiaume Y, Matthay MA. Alveolar edema fluid clearance and acute lung injury. Respir Physiol Neurobiol 2007;159:350–9.
39. Matthay MA, Zemans RL. The acute respiratory distress syndrome: pathogenesis and treatment. Annu Rev Pathol 2011;6:147–63.
40. Bain CC, MacDonald AS. The impact of the lung environment on macrophage development, activation and function: diversity in the face of adversity. Mucosal Immunol 2022;15:223–34.

41. Murray PJ, Allen JE, Biswas SK, et al. Macrophage activation and polarization: nomenclature and experimental guidelines. Immunity 2014;41:14–20.
42. Lavin Y, Winter D, Blecher-Gonen R, et al. Tissue-resident macrophage enhancer landscapes are shaped by the local microenvironment. Cell 2014;159:1312–26.
43. Mulder K, Patel AA, Kong WT, et al. Cross-tissue single-cell landscape of human monocytes and macrophages in health and disease. Immunity 2021;54:1883-1900.e5.
44. Guilliams M, Kleer I de, Henri S, et al. Alveolar macrophages develop from fetal monocytes that differentiate into long-lived cells in the first week of life via GM-CSF. J Exp Med 2013;210:1977–92.
45. Hoeffel G, Ginhoux F. Fetal monocytes and the origins of tissue-resident macrophages. Cell Immunol 2018;330:5–15.
46. Yona S, Kim K-W, Wolf Y, et al. Fate mapping reveals origins and dynamics of monocytes and tissue macrophages under homeostasis. Immunity 2013;38:79–91.
47. van de Laar L, Saelens W, van Prijck S de, et al. Yolk Sac Macrophages, Fetal Liver, and Adult Monocytes Can Colonize an Empty Niche and Develop into Functional Tissue-Resident Macrophages. Immunity 2016;44:755–68.
48. Li F, Okreglicka KM, Pohlmeier LM, Schneider C, Kopf M. Fetal monocytes possess increased metabolic capacity and replace primitive macrophages in tissue macrophage development. EMBO J 2020;39:e103205.
49. Hashimoto D, Chow A, Noizat C, et al. Tissue-resident macrophages self-maintain locally throughout adult life with minimal contribution from circulating monocytes. Immunity 2013;38:792–804.
50. Watanabe S, Alexander M, Misharin AV, Budinger GRS. The role of macrophages in the resolution of inflammation. J Clin Invest 2019;129:2619–28.
51. Evren E, Ringqvist E, Tripathi KP, et al. Distinct developmental pathways from blood monocytes generate human lung macrophage diversity. Immunity 2021;54:259-275.e7.
52. Liu Z, Gu Y, Chakarov S, et al. Fate Mapping via Ms4a3-Expression History Traces Monocyte-Derived Cells. Cell 2019;178:1509-1525.e19.
53. Liao M, Liu Y, Yuan J, et al. Single-cell landscape of bronchoalveolar immune cells in patients with COVID-19. Nat Med 2020;26:842–4.
54. Gautier EL, Shay T, Miller J, et al. Gene-expression profiles and transcriptional regulatory pathways that underlie the identity and diversity of mouse tissue macrophages. Nat Immunol 2012;13:1118–28.
55. Pervizaj-Oruqaj L, Selvakumar B, Ferrero MR, et al. Alveolar macrophage-expressed Plet1 is a driver of lung epithelial repair after viral pneumonia. Nat Commun 2024;15:87.
56. Schneider C, Nobs SP, Kurrer M, Rehrauer H, Thiele C, Kopf M. Induction of the nuclear receptor PPAR-γ by the cytokine GM-CSF is critical for the differentiation of fetal monocytes into alveolar macrophages. Nat Immunol 2014;15:1026–37.
57. McQuattie-Pimentel AC, Ren Z, Joshi N, et al. The lung microenvironment shapes a dysfunctional response of alveolar macrophages in aging. J Clin Invest 2021;131.
58. Schneider JL, Rowe JH, Garcia-de-Alba C, Kim CF, Sharpe AH, Haigis MC. The aging lung: Physiology, disease, and immunity. Cell 2021;184:1990–2019.

59. Morales-Nebreda L, Misharin AV, Perlman H, Budinger GRS. The heterogeneity of lung macrophages in the susceptibility to disease. Eur Respir Rev 2015;24:505–9.
60. Kopf M, Schneider C, Nobs SP. The development and function of lung-resident macrophages and dendritic cells. Nat Immunol 2015;16:36–44.
61. Shibata Y, Berclaz P-Y, Chroneos ZC, Yoshida M, Whitsett JA, Trapnell BC. GM-CSF Regulates Alveolar Macrophage Differentiation and Innate Immunity in the Lung through PU.1. Immunity 2001;15:557–67.
62. Evren E, Ringqvist E, Willinger T. Origin and ontogeny of lung macrophages: from mice to humans. Immunology 2019;160:126–38.
63. Pernet E, Sun S, Sarden N, et al. Neonatal imprinting of alveolar macrophages via neutrophil-derived 12-HETE. Nature 2023;614:530–8.
64. Guilliams M, Scott CL. Does niche competition determine the origin of tissue-resident macrophages? Nat Rev Immunol 2017;17:451–60.
65. Scott CL, T'Jonck W, Martens L, et al. The Transcription Factor ZEB2 Is Required to Maintain the Tissue-Specific Identities of Macrophages. Immunity 2018;49:312-325.e5.
66. Bharat A, Bhorade SM, Morales-Nebreda L, et al. Flow Cytometry Reveals Similarities Between Lung Macrophages in Humans and Mice. Am J Respir Cell Mol Biol 2016;54:147–9.
67. Gibbings SL, Thomas SM, Atif SM, et al. Three Unique Interstitial Macrophages in the Murine Lung at Steady State. Am J Respir Cell Mol Biol 2017;57:66–76.
68. Misharin AV, Morales-Nebreda L, Mutlu GM, Budinger GRS, Perlman H. Flow cytometric analysis of macrophages and dendritic cell subsets in the mouse lung. Am J Respir Cell Mol Biol 2013;49:503–10.
69. Aegerter H, Lambrecht BN, Jakubzick CV. Biology of lung macrophages in health and disease. Immunity 2022;55:1564–80.
70. Rodriguez-Rodriguez L, Gillet L, Machiels B. Shaping of the alveolar landscape by respiratory infections and long-term consequences for lung immunity. Front Immunol 2023;14:1149015.
71. Peng W, Vanneste D, Bejarano D, et al. Endothelial-driven TGFβ signaling supports lung interstitial macrophage development from monocytes. Sci Immunol 2025;10:eadr4977.
72. Yeung ST, Damani-Yokota P, Thannickal SA, et al. Nerve- and airway-associated interstitial macrophages mitigate SARS-CoV-2 pathogenesis via type I interferon signaling. Immunity 2025;58:1327-1342.e5.
73. Zuttion MSSR, Parimon T, Yao C, et al. Interstitial Macrophages Mediate Efferocytosis of Alveolar Epithelium During Influenza Infection. Am J Respir Cell Mol Biol 2024.
74. Schyns J, Bai Q, Ruscitti C, et al. Non-classical tissue monocytes and two functionally distinct populations of interstitial macrophages populate the mouse lung. Nat Commun 2019;10:3964.
75. Hussell T, Bell TJ. Alveolar macrophages: plasticity in a tissue-specific context. Nat Rev Immunol 2014;14:81–93.
76. Green GM, Kass EH. The role of the alveolar macrophage in the clearance of bacteria from the lung. J Exp Med 1964;119:167–76.
77. Davies LC, Jenkins SJ, Allen JE, Taylor PR. Tissue-resident macrophages. Nat Immunol 2013;14:986–95.

78. Halstead ES, Chroneos ZC. Lethal influenza infection: Is a macrophage to blame? Expert Rev Anti Infect Ther 2015;13:1425–8.
79. Woo YD, Jeong D, Chung DH. Development and Functions of Alveolar Macrophages. Mol Cells 2021;44:292–300.
80. Aggarwal NR, King LS, D'Alessio FR. Diverse macrophage populations mediate acute lung inflammation and resolution. Am J Physiol Lung Cell Mol Physiol 2014;306:L709-25.
81. Gordon S, Plüddemann A, Martinez Estrada F. Macrophage heterogeneity in tissues: phenotypic diversity and functions. Immunol Rev 2014;262:36–55.
82. Murray PJ, Wynn TA. Protective and pathogenic functions of macrophage subsets. Nat Rev Immunol 2011;11:723–37.
83. Wang A, Luan HH, Medzhitov R. An evolutionary perspective on immunometabolism. Science 2019;363.
84. Voss K, Hong HS, Bader JE, Sugiura A, Lyssiotis CA, Rathmell JC. A guide to interrogating immunometabolism. Nat Rev Immunol 2021;21:637–52.
85. O'Neill LAJ, Kishton RJ, Rathmell J. A guide to immunometabolism for immunologists. Nat Rev Immunol 2016;16:553–65.
86. Peace CG, O'Neill LA. The role of itaconate in host defense and inflammation. J Clin Invest 2022;132.
87. Lampropoulou V, Sergushichev A, Bambouskova M, et al. Itaconate Links Inhibition of Succinate Dehydrogenase with Macrophage Metabolic Remodeling and Regulation of Inflammation. Cell Metab 2016;24:158–66.
88. Cordes T, Wallace M, Michelucci A, et al. Immunoresponsive Gene 1 and Itaconate Inhibit Succinate Dehydrogenase to Modulate Intracellular Succinate Levels. J Biol Chem 2016;291:14274–84.
89. Mills EL, Kelly B, Logan A, et al. Succinate Dehydrogenase Supports Metabolic Repurposing of Mitochondria to Drive Inflammatory Macrophages. Cell 2016;167:457-470.e13.
90. O'Carroll SM, Peace CG, Toller-Kawahisa JE, et al. Itaconate drives mtRNA-mediated type I interferon production through inhibition of succinate dehydrogenase. Nat Metab 2024;6:2060–9.
91. Luo Z, Sheng Z, Hu L, et al. Targeted macrophage phagocytosis by Irg1/itaconate axis improves the prognosis of intracerebral hemorrhagic stroke and peritonitis. EBioMedicine 2024;101:104993.
92. Chen L-L, Morcelle C, Cheng Z-L, et al. Itaconate inhibits TET DNA dioxygenases to dampen inflammatory responses. Nat Cell Biol 2022;24:353–63.
93. Auger J-P, Zimmermann M, Faas M, et al. Metabolic rewiring promotes anti-inflammatory effects of glucocorticoids. Nature 2024;629:184–92.
94. Faas M, Ipseiz N, Ackermann J, et al. IL-33-induced metabolic reprogramming controls the differentiation of alternatively activated macrophages and the resolution of inflammation. Immunity 2021;54:2531-2546.e5.
95. Wu Y-T, Xu W-T, Zheng L, et al. 4-octyl itaconate ameliorates alveolar macrophage pyroptosis against ARDS via rescuing mitochondrial dysfunction and suppressing the cGAS/STING pathway. Int Immunopharmacol 2023;118:110104.
96. Shan M, Zhang S, Luo Z, et al. Itaconate promotes inflammatory responses in tissue-resident alveolar macrophages and exacerbates acute lung injury. Cell Metab 2025.

97. Swain A, Bambouskova M, Kim H, et al. Comparative evaluation of itaconate and its derivatives reveals divergent inflammasome and type I interferon regulation in macrophages. Nat Metab 2020;2:594–602.
98. Tannahill GM, Curtis AM, Adamik J, et al. Succinate is an inflammatory signal that induces IL-1β through HIF-1α. Nature 2013;496:238–42.
99. Kelly B, O'Neill LAJ. Metabolic reprogramming in macrophages and dendritic cells in innate immunity. Cell Res 2015;25:771–84.
100. Liu S, Yang J, Wu Z. The Regulatory Role of α-Ketoglutarate Metabolism in Macrophages. Mediators Inflamm 2021;2021:5577577.
101. Liu P-S, Wang H, Li X, et al. α-ketoglutarate orchestrates macrophage activation through metabolic and epigenetic reprogramming. Nat Immunol 2017;18:985–94.
102. Liu M, Chen Y, Wang S, et al. α-Ketoglutarate Modulates Macrophage Polarization Through Regulation of PPARγ Transcription and mTORC1/p70S6K Pathway to Ameliorate ALI/ARDS. Shock 2020;53:103–13.
103. Zhou B, Magana L, Hong Z, et al. The angiocrine Rspondin3 instructs interstitial macrophage transition via metabolic-epigenetic reprogramming and resolves inflammatory injury. Nat Immunol 2020;21:1430–43.
104. Xia W, Mao Y, Xia Z, Cheng J, Jiang P. Metabolic remodelling produces fumarate via the aspartate-argininosuccinate shunt in macrophages as an antiviral defence. Nat Microbiol 2025;10:1115–29.
105. Pålsson-McDermott EM, O'Neill LAJ. Gang of 3: How the Krebs cycle-linked metabolites itaconate, succinate, and fumarate regulate macrophages and inflammation. Cell Metab 2025;37:1049–59.
106. Kelly D, Wischmeyer PE. Role of L-glutamine in critical illness: new insights. Curr Opin Clin Nutr Metab Care 2003;6:217–22.
107. Woods PS, Mutlu GM. Differences in glycolytic metabolism between tissue-resident alveolar macrophages and recruited lung macrophages. Front Immunol 2025;16:1535796.
108. Wculek SK, Dunphy G, Heras-Murillo I, Mastrangelo A, Sancho D. Metabolism of tissue macrophages in homeostasis and pathology. Cell Mol Immunol 2022;19:384–408.
109. Wculek SK, Heras-Murillo I, Mastrangelo A, et al. Oxidative phosphorylation selectively orchestrates tissue macrophage homeostasis. Immunity 2023;56:516-530.e9.
110. Woods PS, Kimmig LM, Meliton AY, et al. Tissue-Resident Alveolar Macrophages Do Not Rely on Glycolysis for LPS-induced Inflammation. Am J Respir Cell Mol Biol 2020;62:243–55.
111. Woods PS, Kimmig LM, Sun KA, et al. HIF-1α induces glycolytic reprograming in tissue-resident alveolar macrophages to promote cell survival during acute lung injury. Elife 2022;11.
112. Liao M, Liu Y, Yuan J, et al. Single-cell landscape of bronchoalveolar immune cells in patients with COVID-19. Nat Med 2020;26:842–4.
113. Li F, Piattini F, Pohlmeier L, Feng Q, Rehrauer H, Kopf M. Monocyte-derived alveolar macrophages autonomously determine severe outcome of respiratory viral infection. Sci Immunol 2022;7:eabj5761.
114. Aegerter H, Kulikauskaite J, Crotta S, et al. Influenza-induced monocyte-derived alveolar macrophages confer prolonged antibacterial protection. Nat Immunol 2020;21:145–57.
115. Vijayan V, Pradhan P, Braud L, et al. Human and murine macrophages exhibit differential metabolic responses to lipopolysaccharide - A divergent role for glycolysis. Redox Biol 2019;22:101147.

116. Trinchese G, Cimmino F, Catapano A, Cavaliere G, Mollica MP. Mitochondria: the gatekeepers between metabolism and immunity. Front Immunol 2024;15:1334006.
117. Afroz SF, Raven KD, Lawrence GMEP, Kapetanovic R, Schroder K, Sweet MJ. Mitochondrial dynamics in macrophages: divide to conquer or unite to survive? Biochem Soc Trans 2023;51:41–56.
118. Lane N, Martin W. The energetics of genome complexity. Nature 2010;467:929–34.
119. Gray MW. Mosaic nature of the mitochondrial proteome: Implications for the origin and evolution of mitochondria. Proc Natl Acad Sci U S A 2015;112:10133–8.
120. Marques E, Kramer R, Ryan DG. Multifaceted mitochondria in innate immunity. NPJ Metab Health Dis 2024;2:6.
121. Sesaki H, Jensen RE. Division versus fusion: Dnm1p and Fzo1p antagonistically regulate mitochondrial shape. J Cell Biol 1999;147:699–706.
122. Blackstone C, Chang C-R. Mitochondria unite to survive. Nat Cell Biol 2011;13:521–2.
123. Chen W, Zhao H, Li Y. Mitochondrial dynamics in health and disease: mechanisms and potential targets. Signal Transduct Target Ther 2023;8:333.
124. Tiku V, Tan M-W, Dikic I. Mitochondrial Functions in Infection and Immunity. Trends Cell Biol 2020;30:263–75.
125. West AP, Shadel GS, Ghosh S. Mitochondria in innate immune responses. Nat Rev Immunol 2011;11:389–402.
126. Liu X, Kim CN, Yang J, Jemmerson R, Wang X. Induction of apoptotic program in cell-free extracts: requirement for dATP and cytochrome c. Cell 1996;86:147–57.
127. Mukherjee A, Ghosh KK, Chakrabortty S, Gulyás B, Padmanabhan P, Ball WB. Mitochondrial Reactive Oxygen Species in Infection and Immunity. Biomolecules 2024;14.
128. Shadel GS, Horvath TL. Mitochondrial ROS signaling in organismal homeostasis. Cell 2015;163:560–9.
129. Sies H, Belousov VV, Chandel NS, et al. Defining roles of specific reactive oxygen species (ROS) in cell biology and physiology. Nat Rev Mol Cell Biol 2022;23:499–515.
130. Sena LA, Chandel NS. Physiological roles of mitochondrial reactive oxygen species. Mol Cell 2012;48:158–67.
131. Brand MD. The sites and topology of mitochondrial superoxide production. Exp Gerontol 2010;45:466–72.
132. Brand MD. Mitochondrial generation of superoxide and hydrogen peroxide as the source of mitochondrial redox signaling. Free Radic Biol Med 2016;100:14–31.
133. Berry BJ, Trewin AJ, Amitrano AM, Kim M, Wojtovich AP. Use the Protonmotive Force: Mitochondrial Uncoupling and Reactive Oxygen Species. J Mol Biol 2018;430:3873–91.
134. Murphy MP. How mitochondria produce reactive oxygen species. Biochem J 2009;417:1–13.
135. Forrester SJ, Kikuchi DS, Hernandes MS, Xu Q, Griendling KK. Reactive Oxygen Species in Metabolic and Inflammatory Signaling. Circ Res 2018;122:877–902.
136. Preston JA, Bewley MA, Marriott HM, et al. Alveolar Macrophage Apoptosis-associated Bacterial Killing Helps Prevent Murine Pneumonia. Am J Respir Crit Care Med 2019;200:84–97.

137. Bewley MA, Preston JA, Mohasin M, et al. Impaired Mitochondrial Microbicidal Responses in Chronic Obstructive Pulmonary Disease Macrophages. Am J Respir Crit Care Med 2017;196:845–55.
138. West AP, Brodsky IE, Rahner C, et al. TLR signalling augments macrophage bactericidal activity through mitochondrial ROS. Nature 2011;472:476–80.
139. Weinberg SE, Sena LA, Chandel NS. Mitochondria in the regulation of innate and adaptive immunity. Immunity 2015;42:406–17.
140. Nakahira K, Haspel JA, Rathinam VAK, et al. Autophagy proteins regulate innate immune responses by inhibiting the release of mitochondrial DNA mediated by the NALP3 inflammasome. Nat Immunol 2011;12:222–30.
141. Zhou R, Yazdi AS, Menu P, Tschopp J. A role for mitochondria in NLRP3 inflammasome activation. Nature 2011;469:221–5.
142. Billingham LK, Stoolman JS, Vasan K, et al. Mitochondrial electron transport chain is necessary for NLRP3 inflammasome activation. Nat Immunol 2022;23:692–704.
143. Palmieri EM, Gonzalez-Cotto M, Baseler WA, et al. Nitric oxide orchestrates metabolic rewiring in M1 macrophages by targeting aconitase 2 and pyruvate dehydrogenase. Nat Commun 2020;11:698.
144. Reynolds MB, Hong HS, Michmerhuizen BC, et al. Cardiolipin coordinates inflammatory metabolic reprogramming through regulation of Complex II disassembly and degradation. Sci Adv 2023;9:eade8701.
145. van den Bossche J, Baardman J, Otto NA, et al. Mitochondrial Dysfunction Prevents Repolarization of Inflammatory Macrophages. Cell Rep 2016;17:684–96.
146. Dowling JK, Afzal R, Gearing LJ, et al. Mitochondrial arginase-2 is essential for IL-10 metabolic reprogramming of inflammatory macrophages. Nat Commun 2021;12:1460.
147. Fleury C, Neverova M, Collins S, et al. Uncoupling protein-2: a novel gene linked to obesity and hyperinsulinemia. Nat Genet 1997;15:269–72.
148. Arsenijevic D, Onuma H, Pecqueur C, et al. Disruption of the uncoupling protein-2 gene in mice reveals a role in immunity and reactive oxygen species production. Nat Genet 2000;26:435–9.
149. Rousset S, Emre Y, Join-Lambert O, Hurtaud C, Ricquier D, Cassard-Doulcier A-M. The uncoupling protein 2 modulates the cytokine balance in innate immunity. Cytokine 2006;35:135–42.
150. Abuaita BH, Schultz TL, O'Riordan MX. Mitochondria-Derived Vesicles Deliver Antimicrobial Reactive Oxygen Species to Control Phagosome-Localized Staphylococcus aureus. Cell Host Microbe 2018;24:625-636.e5.
151. Krause K, Daily K, Estfanous S, et al. Caspase-11 counteracts mitochondrial ROS-mediated clearance of Staphylococcus aureus in macrophages. EMBO Rep 2019;20:e48109.
152. Chandel NS, Schumacker PT, Arch RH. Reactive oxygen species are downstream products of TRAF-mediated signal transduction. J Biol Chem 2001;276:42728–36.
153. Chandel NS, McClintock DS, Feliciano CE, et al. Reactive oxygen species generated at mitochondrial complex III stabilize hypoxia-inducible factor-1alpha during hypoxia: a mechanism of O2 sensing. J Biol Chem 2000;275:25130–8.
154. Guzy RD, Hoyos B, Robin E, et al. Mitochondrial complex III is required for hypoxia-induced ROS production and cellular oxygen sensing. Cell Metab 2005;1:401–8.

155. Rodríguez-Morales P, Franklin RA. Macrophage phenotypes and functions: resolving inflammation and restoring homeostasis. Trends Immunol 2023;44:986–98.
156. Vannella KM, Wynn TA. Mechanisms of Organ Injury and Repair by Macrophages. Annu. Rev. Physiol. 2017;79:593–617.
157. Melloni B, Lesur O, Bouhadiba T, Cantin A, Martel M, Bégin R. Effect of exposure to silica on human alveolar macrophages in supporting growth activity in type II epithelial cells. Thorax 1996;51:781–6.
158. Chamoto K, Gibney BC, Ackermann M, et al. Alveolar macrophage dynamics in murine lung regeneration. J Cell Physiol 2012;227:3208–15.
159. Cakarova L, Marsh LM, Wilhelm J, et al. Macrophage tumor necrosis factor-alpha induces epithelial expression of granulocyte-macrophage colony-stimulating factor: impact on alveolar epithelial repair. Am J Respir Crit Care Med 2009;180:521–32.
160. Hoagland DA, Rodríguez-Morales P, Mann AO, et al. Macrophage-derived oncostatin M repairs the lung epithelial barrier during inflammatory damage. Science 2025;389:169–75.
161. Grabiec AM, Hussell T. The role of airway macrophages in apoptotic cell clearance following acute and chronic lung inflammation. Semin Immunopathol 2016;38:409–23.
162. Cox G, Crossley J, Xing Z. Macrophage engulfment of apoptotic neutrophils contributes to the resolution of acute pulmonary inflammation in vivo. Am J Respir Cell Mol Biol 1995;12:232–7.
163. Boada-Romero E, Martinez J, Heckmann BL, Green DR. The clearance of dead cells by efferocytosis. Nat Rev Mol Cell Biol 2020;21:398–414.
164. Mehrotra P, Ravichandran KS. Drugging the efferocytosis process: concepts and opportunities. Nat Rev Drug Discov 2022;21:601–20.
165. Moon B, Yang S, Moon H, Lee J, Park D. After cell death: the molecular machinery of efferocytosis. Exp Mol Med 2023;55:1644–51.
166. Nagata S. Apoptosis and Clearance of Apoptotic Cells. Annu Rev Immunol 2018;36:489–517.
167. Rothlin CV, Hille TD, Ghosh S. Determining the effector response to cell death. Nat Rev Immunol 2021;21:292–304.
168. Mehrotra P, Maschalidi S, Boeckaerts L, et al. Oxylipins and metabolites from pyroptotic cells act as promoters of tissue repair. Nature 2024;631:207–15.
169. Dalli J, Serhan CN. Specific lipid mediator signatures of human phagocytes: microparticles stimulate macrophage efferocytosis and pro-resolving mediators. Blood 2012;120:e60-72.
170. Dalli J, Serhan C. Macrophage Proresolving Mediators-the When and Where. Microbiol Spectr 2016;4.
171. Schif-Zuck S, Gross N, Assi S, Rostoker R, Serhan CN, Ariel A. Saturated-efferocytosis generates pro-resolving CD11b low macrophages: modulation by resolvins and glucocorticoids. Eur J Immunol 2011;41:366–79.
172. Fadok VA, Bratton DL, Konowal A, Freed PW, Westcott JY, Henson PM. Macrophages that have ingested apoptotic cells in vitro inhibit proinflammatory cytokine production through autocrine/paracrine mechanisms involving TGF-beta, PGE2, and PAF. J Clin Invest 1998;101:890–8.
173. Voll RE, Herrmann M, Roth EA, Stach C, Kalden JR, Girkontaite I. Immunosuppressive effects of apoptotic cells. Nature 1997;390:350–1.

174. Zhang S, Weinberg S, DeBerge M, et al. Efferocytosis Fuels Requirements of Fatty Acid Oxidation and the Electron Transport Chain to Polarize Macrophages for Tissue Repair. Cell Metab 2019;29:443-456.e5.
175. Sukka SR, Ampomah PB, Darville LNF, et al. Efferocytosis drives a tryptophan metabolism pathway in macrophages to promote tissue resolution. Nat Metab 2024;6:1736–55.
176. Doran AC, Yurdagul A, Tabas I. Efferocytosis in health and disease. Nat Rev Immunol 2020;20:254–67.
177. Park D, Han CZ, Elliott MR, et al. Continued clearance of apoptotic cells critically depends on the phagocyte Ucp2 protein. Nature 2011;477:220–4.
178. Wang Y, Subramanian M, Yurdagul A, et al. Mitochondrial Fission Promotes the Continued Clearance of Apoptotic Cells by Macrophages. Cell 2017;171:331-345.e22.
179. Merlin J, Ivanov S, Dumont A, et al. Non-canonical glutamine transamination sustains efferocytosis by coupling redox buffering to oxidative phosphorylation. Nat Metab 2021;3:1313–26.
180. Morioka S, Perry JSA, Raymond MH, et al. Efferocytosis induces a novel SLC program to promote glucose uptake and lactate release. Nature 2018;563:714–8.
181. A-Gonzalez N, Bensinger SJ, Hong C, et al. Apoptotic cells promote their own clearance and immune tolerance through activation of the nuclear receptor LXR. Immunity 2009;31:245–58.
182. Mukundan L, Odegaard JI, Morel CR, et al. PPAR-delta senses and orchestrates clearance of apoptotic cells to promote tolerance. Nat Med 2009;15:1266–72.
183. Proto JD, Doran AC, Gusarova G, et al. Regulatory T Cells Promote Macrophage Efferocytosis during Inflammation Resolution. Immunity 2018;49:666-677.e6.
184. Wang Y-T, Trzeciak AJ, Rojas WS, et al. Metabolic adaptation supports enhanced macrophage efferocytosis in limited-oxygen environments. Cell Metab 2023;35:316-331.e6.
185. Horckmans M, Ring L, Duchene J, et al. Neutrophils orchestrate post-myocardial infarction healing by polarizing macrophages towards a reparative phenotype. Eur Heart J 2017;38:187–97.
186. Yurdagul A, Subramanian M, Wang X, et al. Macrophage Metabolism of Apoptotic Cell-Derived Arginine Promotes Continual Efferocytosis and Resolution of Injury. Cell Metab 2020;31:518-533.e10.
187. Luo B, Wang Z, Zhang Z, Shen Z, Zhang Z. The deficiency of macrophage erythropoietin signaling contributes to delayed acute inflammation resolution in diet-induced obese mice. Biochim Biophys Acta Mol Basis Dis 2019;1865:339–49.
188. Sather S, Kenyon KD, Lefkowitz JB, et al. A soluble form of the Mer receptor tyrosine kinase inhibits macrophage clearance of apoptotic cells and platelet aggregation. Blood 2007;109:1026–33.
189. Thorp E, Vaisar T, Subramanian M, Mautner L, Blobel C, Tabas I. Shedding of the Mer tyrosine kinase receptor is mediated by ADAM17 protein through a pathway involving reactive oxygen species, protein kinase Cδ, and p38 mitogen-activated protein kinase (MAPK). J Biol Chem 2011;286:33335–44.
190. Chang C-F, Goods BA, Askenase MH, et al. Erythrocyte efferocytosis modulates macrophages towards recovery after intracerebral hemorrhage. J Clin Invest 2018;128:607–24.
191. Mahida RY, Scott A, Parekh D, et al. Acute respiratory distress syndrome is associated with impaired alveolar macrophage efferocytosis. Eur Respir J 2021;58.

192. Grégoire M, Uhel F, Lesouhaitier M, et al. Impaired efferocytosis and neutrophil extracellular trap clearance by macrophages in ARDS. Eur Respir J 2018;52.
193. Newson J, Stables M, Karra E, et al. Resolution of acute inflammation bridges the gap between innate and adaptive immunity. Blood 2014;124:1748–64.
194. Guillon A, Arafa EI, Barker KA, et al. Pneumonia recovery reprograms the alveolar macrophage pool. JCI Insight 2020;5.
195. Arafa EI, Shenoy AT, Barker KA, et al. Recruitment and training of alveolar macrophages after pneumococcal pneumonia. JCI Insight 2022;7.
196. Aegerter H, Kulikauskaite J, Crotta S, et al. Influenza-induced monocyte-derived alveolar macrophages confer prolonged antibacterial protection. Nat Immunol 2020;21:145–57.
197. Feehan KT, Bridgewater HE, Stenkiewicz-Witeska J, et al. Post-resolution macrophages shape long-term tissue immunity and integrity in a mouse model of pneumococcal pneumonia. Nat Commun 2024;15:4326.
198. Newson J, Motwani MP, Kendall AC, et al. Inflammatory Resolution Triggers a Prolonged Phase of Immune Suppression through COX-1/mPGES-1-Derived Prostaglandin E2. Cell Rep 2017;20:3162–75.
199. Roquilly A, Jacqueline C, Davieau M, et al. Alveolar macrophages are epigenetically altered after inflammation, leading to long-term lung immunoparalysis. Nat Immunol 2020;21:636–48.
200. Matt U, Warszawska JM, Bauer M, et al. Bbeta(15-42) protects against acid-induced acute lung injury and secondary pseudomonas pneumonia in vivo. Am J Respir Crit Care Med 2009;180:1208–17.
201. Kaur M, Bell T, Salek-Ardakani S, Hussell T. Macrophage adaptation in airway inflammatory resolution. Eur Respir Rev 2015;24:510–5.
202. Medeiros AI, Serezani CH, Lee SP, Peters-Golden M. Efferocytosis impairs pulmonary macrophage and lung antibacterial function via PGE2/EP2 signaling. J Exp Med 2009;206:61–8.
203. Neupane AS, Willson M, Chojnacki AK, et al. Patrolling Alveolar Macrophages Conceal Bacteria from the Immune System to Maintain Homeostasis. Cell 2020;183:110-125.e11.
204. Malainou C, Abdin SM, Lachmann N, Matt U, Herold S. Alveolar macrophages in tissue homeostasis, inflammation, and infection: evolving concepts of therapeutic targeting. J Clin Invest 2023;133.
205. Pervizaj-Oruqaj L, Ferrero MR, Matt U, Herold S. The guardians of pulmonary harmony: alveolar macrophages orchestrating the symphony of lung inflammation and tissue homeostasis. Eur Respir Rev 2024;33.
206. Matute-Bello G, Frevert CW, Martin TR. Animal models of acute lung injury. Am J Physiol Lung Cell Mol Physiol 2008;295:L379-99.
207. Casey AM, Ryan DG, Prag HA, et al. Pro-inflammatory macrophages produce mitochondria-derived superoxide by reverse electron transport at complex I that regulates IL-1β release during NLRP3 inflammasome activation. Nat Metab 2025;7:493–507.
208. Naik E, Dixit VM. Mitochondrial reactive oxygen species drive proinflammatory cytokine production. J Exp Med 2011;208:417–20.
209. Shepherd VL, Hoidal JR. Clearance of neutrophil-derived myeloperoxidase by the macrophage mannose receptor. Am J Respir Cell Mol Biol 1990;2:335–40.

210. ONO T, IMAI K, YAMADA M, NAGASUE N. Endocytosis of Myeloperoxidase by Human Monocyte-Derived Macrophages and Multistep Regulation of Mannose Receptor Activity during Macrophage Differentiation. J. Clin. Biochem. Nutr. 1998;25:109–19.
211. Brand MD, Esteves TC. Physiological functions of the mitochondrial uncoupling proteins UCP2 and UCP3. Cell Metab 2005;2:85–93.
212. Pecqueur C, Alves-Guerra MC, Gelly C, et al. Uncoupling protein 2, in vivo distribution, induction upon oxidative stress, and evidence for translational regulation. J Biol Chem 2001;276:8705–12.
213. Alves-Guerra M-C, Rousset S, Pecqueur C, et al. Bone marrow transplantation reveals the in vivo expression of the mitochondrial uncoupling protein 2 in immune and nonimmune cells during inflammation. J Biol Chem 2003;278:42307–12.
214. Bouillaud F. UCP2, not a physiologically relevant uncoupler but a glucose sparing switch impacting ROS production and glucose sensing. Biochim Biophys Acta 2009;1787:377–83.
215. Pecqueur C, Alves-Guerra C, Ricquier D, Bouillaud F. UCP2, a metabolic sensor coupling glucose oxidation to mitochondrial metabolism? IUBMB Life 2009;61:762–7.
216. Rupprecht A, Moldzio R, Mödl B, Pohl EE. Glutamine regulates mitochondrial uncoupling protein 2 to promote glutaminolysis in neuroblastoma cells. Biochim Biophys Acta Bioenerg 2019;1860:391–401.
217. Vozza A, Parisi G, Leonardis F de, et al. UCP2 transports C4 metabolites out of mitochondria, regulating glucose and glutamine oxidation. Proc Natl Acad Sci U S A 2014;111:960–5.
218. Rousset S, Mozo J, Dujardin G, et al. UCP2 is a mitochondrial transporter with an unusual very short half-life. FEBS Lett 2007;581:479–82.
219. Fullerton JN, O'Brien AJ, Gilroy DW. Pathways mediating resolution of inflammation: when enough is too much. J Pathol 2013;231:8–20.
220. Peiseler M, Kubes P. More friend than foe: the emerging role of neutrophils in tissue repair. J Clin Invest 2019;129:2629–39.
221. Serhan CN, Savill J. Resolution of inflammation: the beginning programs the end. Nat Immunol 2005;6:1191–7.
222. Arnhold J. The Dual Role of Myeloperoxidase in Immune Response. Int J Mol Sci 2020;21.
223. Morioka S, Maueröder C, Ravichandran KS. Living on the Edge: Efferocytosis at the Interface of Homeostasis and Pathology. Immunity 2019;50:1149–62.
224. Reber LL, Gillis CM, Starkl P, et al. Neutrophil myeloperoxidase diminishes the toxic effects and mortality induced by lipopolysaccharide. J Exp Med 2017;214:1249–58.
225. Rehring JF, Bui TM, Galán-Enríquez CS, et al. Released Myeloperoxidase Attenuates Neutrophil Migration and Accumulation in Inflamed Tissue. Front Immunol 2021;12:654259.
226. Wong AO, Ravichandran KS. Apoptotic cells are not all created equal. Sci Immunol 2025;10:eadv4682.
227. Liebold I, Al Jawazneh A, Casar C, et al. Apoptotic cell identity induces distinct functional responses to IL-4 in efferocytic macrophages. Science 2024;384:eabo7027.
228. Kim KK, Dotson MR, Agarwal M, et al. Efferocytosis of apoptotic alveolar epithelial cells is sufficient to initiate lung fibrosis. Cell Death Dis 2018;9:1056.

229. Poon IKH, Lucas CD, Rossi AG, Ravichandran KS. Apoptotic cell clearance: basic biology and therapeutic potential. Nat Rev Immunol 2014;14:166–80.
230. Saas P, Daguindau E, Perruche S. Concise Review: Apoptotic Cell-Based Therapies-Rationale, Preclinical Results and Future Clinical Developments. Stem Cells 2016;34:1464–73.
231. Toussirot E, Bonnefoy F, Vauchy C, Perruche S, Saas P. Mini-Review: The Administration of Apoptotic Cells for Treating Rheumatoid Arthritis: Current Knowledge and Clinical Perspectives. Front Immunol 2021;12:630170.
232. van Heerden PV, Abutbul A, Sviri S, et al. Apoptotic Cells for Therapeutic Use in Cytokine Storm Associated With Sepsis- A Phase Ib Clinical Trial. Front Immunol 2021;12:718191.
233. Gorki A-D, Symmank D, Zahalka S, et al. Murine Ex Vivo Cultured Alveolar Macrophages Provide a Novel Tool to Study Tissue-Resident Macrophage Behavior and Function. Am J Respir Cell Mol Biol 2022;66:64–75.

Overview of proposed mechanism

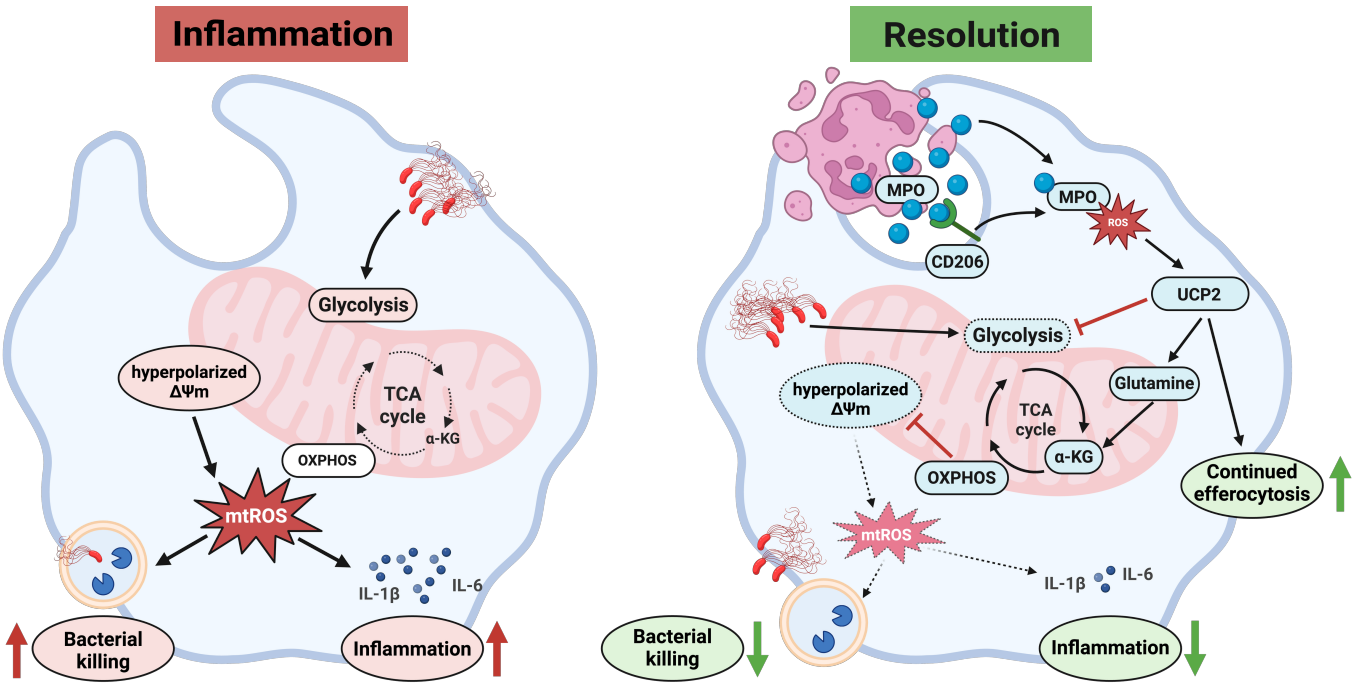

Figure 16. Synopsis of proposed mechanism

Left: Inflammation is characterized by enhanced aerobic glycolysis while oxidative phosphorylation is inhibted favoring a hyperpolarized MMP and therefore, increased mtROS production. Consecutively, mtROS-associated bacterial killing and pro-inflammatory cytokine secretion is promoted.

Right: During resolution of inflammation, AMs take up Neutrophil-derived MPO through efferocytosis or in a receptor-mediated manner (CD206). Upon secondary bacterial infection, MPO-derived ROS stabilize UCP2 which favors canonical glutaminolysis while inhibiting glycolysis. Glutaminolysis fuels the TCA cycle through α-KG and thereby, enhancing oxidative phosphorylation. This prevents hyperpolarization of the MMP and dampens mtROS production. Consecutively, mtROS-associated bacterial killing and pro-inflammatory cytokine secretion is suppressed. In summary, UCP2-mediated immunometabolic reprogramming restricts the functional plasticity of tissue-resident macrophages to prioritize resolution of inflammation over host defense against bacteria.

*Created with BioRender.com

Summary

Resolution of lung injuries is vital to maintain gas exchange and restore homeostasis. Concurrently, there is an increased risk of secondary bacterial pneumonia. AMs are crucial to not only initiate inflammation and clear bacteria but also promote resolution. However, environmental cues that switch these seemingly opposing functional phenotypes of AMs remain elusive. Resolution of lung inflammation requires efferocytosis of AECs and neutrophils.

Here, we discovered an incapacity of AMs to mount an effective immune response to bacteria during resolution of inflammation. Efferocytosis of both cell types led to an anti-inflammatory phenotype in AMs. Intriguingly though, only efferocytosis of neutrophils reprogrammed mitochondrial metabolism of AMs to restrict functional plasticity during resolution of inflammation. PMN-derived MPO fueled canonical glutaminolysis through UCP2 resulting in decreased mtROS-dependent killing of bacteria and secretion of pro-inflammatory cytokines. Instead, MPO-mediated stabilization of UCP2 inhibited mitochondrial hyperpolarization and boosted efferocytosis irrespective of the presence of bacterial pathogens. In contrast, efferocytosis of AECs resulted in a distinct anti-inflammatory phenotype in AMs maintaining phenotypic plasticity towards bacteria.

Overall, uptake of apoptotic neutrophils switches AMs to prioritize resolution of inflammation over antibacterial responses and likewise affects hAMs.

Key message

MPO activates an immunometabolic rheostat to restrict functional plasticity of macrophages to enhance resolution of inflammation and the expense of bacterial control.

Zusammenfassung

Die Resolution von Lungenschäden ist entscheidend, um den Gasaustausch aufrechtzuerhalten und die Homöostase wiederherzustellen. Gleichzeitig besteht ein erhöhtes Risiko für sekundäre bakterielle Pneumonien. AMs sind entscheidend, um sowohl den Beginn von Entzündungen einzuleiten und Bakterien zu beseitigen als auch die Resolution von Entzündungen zu fördern. Allerdings sind alveoläre Faktoren, die diese scheinbar gegensätzlichen funktionellen Phänotypen von AMs regulieren, weitgehend unbekannt. Die Resolution von Lungenentzündungen erfordert Efferozytose von AECs und Neutrophilen.

Während der Resolution von Entzündungen entdeckten wir die Unfähigkeit von AMs, eine wirksame Immunantwort auf Bakterien zu entwickeln. Die Efferozytose beider Zelltypen führte zu einem entzündungshemmenden Phänotyp in AMs. Interessanterweise führte jedoch nur die Efferozytose von Neutrophilen zu einer Umprogrammierung des mitochondrialen Stoffwechsels von AMs, um so ihre funktionelle Plastizität während der Resolution von Entzündungen einzuschränken. Neutrophilen-MPO förderte die kanonische Glutaminolyse durch UCP2, was zu einer verminderten mtROS-vermittelten Abtötung von Bakterien und Sekretion pro-inflammatorischer Zytokine führte. Stattdessen verhinderte die, durch MPO vermittelte, Stabilisierung von UCP2 die mitochondriale Hyperpolarisation und steigerte die Efferozytose sogar in Präsenz von Bakterien. Im Gegensatz dazu führte die Efferozytose von AECs zu einem distinkten entzündungshemmenden Phänotyp von AMs, aber unter Erhalt ihrer phänotypischen Plastizität gegenüber Bakterien.

In Zusammenschau führt die Aufnahme apoptotischer Neutrophile dazu, dass Alveolarmakrophagen die Auflösung von Entzündungen gegenüber bakterieller Abwehr priorisieren, welches auch für humane Alveolarmakrophagen gilt.

Schlüsselbotschaft

MPO aktiviert einen immunmetabolischen Rheostat, der die funktionelle Plastizität von Makrophagen zugunsten pro-resolutorischer Eigenschaften, aber auf Kosten der antibakteriellen Immunabwehr, einschränkt.

Methods

Animals

10-12 weeks old, female C57BL/6N wildtype mice and breeding pairs of $Mpo^{-/-}$ mice (B6.129X1-Mpotm1Lus/J) were purchased from Charles River Laboratories. $Ucp2^{-/-}$ mice (B6.129S4-Ucp2tm1Lowl) were kindly provided by the laboratory of Natascha Sommer (University of Giessen, Hesse, Germany). Female mice were used for in vivo experiments, while both, female and male, mice were used for in vitro experiments. All mice were housed in a specific pathogen-free environment. Animal experiments were conducted according to the legal regulations of the German Animal Welfare Act (Tierschutzgesetz) and approved by the regional authorities of the State of Hesse (Regierungspräsidium Giessen) and the Institutional Commission for the Care and Use of Laboratory Animals (CICUAL), Buenos Aires, Argentina. Monitoring was performed daily depending on experimental severity. A scoring system was developed based on weight reduction, general physical appearance, spontaneous behavior, as well as experiment-related criteria (tachypnea, dyspnea, visible breathing with reduced breath frequency, apathy, immobility, severe dehydration, cyanotic mucosae, and gasping). Depending on the scoring, specific measures were undertaken in line with local animal welfare laws.

Table 1. Experimental scoring for in vivo experiments.

0	Scoring every 24 hours No measures undertaken
5-9	Scoring every 12 hours 5% glucose added to the drinking water Softened food pellets placed within the cage Reduced handling
10-19	Scoring every 8 hours 5% glucose added to the drinking water Softened food pellets placed within the cage Reduced handling Consultation with a veterinarian

>=20	Scoring every 4-6 hours 5% glucose added to the drinking water High-calory wet food (e.g. Clear H2O boost) Reduced handling Consultation with the animal welfare officer
>=20 over more than 24h	Euthanasia and notification of the project leader

More specifically, animals were euthanized when a scoring of 20 was persisting over 24 hours, when a control animal had to be sacrificed due to high scoring and an analysis was possible at the given time point, or when a scoring of 10-15 was assigned to an animal for more than five successive days. Animal experiments were performed at the Biomedical Research Center Seltersberg (Biomedizinisches Forschungszentrum Seltersberg) and the Central Animal Laboratory (Zentrales Tierlabor, Room 108) of the Justus Liebig University of Giessen as well as the Max Planck Heart and Lung Laboratory of the Institute of Biomedicine Investigation of Buenos 35 Aires (Instituto de Investigación en Biomedicina de Buenos Aires, IBioBA-CONICET-Partner Institute of the Max Planck Society).

Primary cell harvest and *ex vivo* cell culture

AMs

AMs were obtained from broncho-alveolar lavage fluid (BALF). Mice were sacrificed, the trachea was exposed, incised, and intubated with a blunt 21G cannula. Broncho-alveolar lavage (BAL) was performed by successively instilling seven times 1mL of cold PBS-/- plus EDTA intratracheally (i.t.). Recovery volume was centrifuged at 500g for 10 minutes. The supernatant was discarded while the cell pellet was resuspended in an RPMI 1640-based medium containing 2.5% HEPES, 2% FCS, and 1% Penicillin/Streptomycin/L-Glutamine and cultured at 37°C/5% CO_2. Non-adherent cells were washed away.

Murine ex-vivo cultured AMs (mexAMs)

mexAMs were acquired according to the manuscript of Gorki et al. (233). AMs were obtained as described above and cultured in RPMI containing 10% FCS and 1% Penicillin/Streptomycin/L-Glutamine supplemented with murine GM-CSF (30ng/mL), human

TGF-β (10ng/mL), and Rosiglitazone (1µM). Medium was changed twice per week, and cells were passaged when 70-90% confluency was reached. For this, cells were gently washed with PBS before being trypsinized to detach cells at 37°C. After centrifugation, cells were counted and seeded at 2.5-3x10^4 cells/cm^2. All experiments were performed between passage 4-10. mexAMs were used to confirm the results of functional assays, such as bacterial phagocytosis and bacterial killing, which had been obtained with primary AMs.

Human AMs

Human AMs were obtained from human BALF with a macrophage purity >=90% of patients that underwent bronchoscopy for diagnostic purposes. In general, patients were non-smokers without any chronic pulmonary disease who provided written consent to the use of biomaterial using the consent form of the DZL (Deutsches Zentrum für Lungenforschung). The project was reviewed and is covered under the University of Giessen ethics committee decision (AZ 58/15) and was performed according to the appropriate regulations and the Declaration of Helsinki. Human BALF was centrifuged before cells were resuspended in an RPMI-based medium containing 2.5% HEPES, 2% FCS, and 1% Penicillin/Streptomycin/L-Glutamine, and cultured at 37°C/5% CO_2. Non-adherent cells were removed.

Murine bone marrow-derived PMNs

PMNs were isolated from femoral and tibial bone marrow as described above. PMNs were isolated with a magnetic purification kit according to manufacturer's instructions (Miltenyi Biotec; Neutrophil Isolation Kit, Mouse).

Primary AECs

Primary AECs were isolated from murine lungs. Therefore, lung homogenates were obtained by instillation of Dispase II i.t. into HBSS perfused lungs, followed by incubation in Dispase II for 45min at RT. After removal of the trachea and proximal bronchial tree, the lungs were homogenized (gentleMACS Dissociator; MACS Miltenyi Biotec) in DMEM/2.5% HEPES with 0.01% DNase I and filtered successively through 100 and 40µm nylon filters. Cell suspensions were incubated with biotinylated anti-mouse CD45, CD16/32, and CD31 monoclonal antibodies for 30 min at 37°C followed by incubation with biotin-binding magnetic beads and magnetic separation to deplete leukocytes and endothelial cells. AEC suspensions with a

purity >= 90% as determined by flow cytometry were cultured in DMEM-based medium enriched with HEPES, 10% FCS, and 1% Penicillin/Streptomycin/L-Glutamine at 37°C/5% CO_2.

In vitro cell culture

AECs

AECs were represented by the in vitro cell line MLE-12 (ATCC: CRL-2110). As an exception, they are denoted as "MLE" when directly compared to primary AECs (pAECs). MLE-12 were grown in a T-75 cell culture flask supplemented with a RPMI-based medium containing 10% FCS, ITS (Insulin 0.005 mg/mL), Transferrin (0.01 mg/mL), Sodium selenite (30nM), 1% Penicillin/Streptomycin/L-Glutamine at 37°C/5% CO_2.

Jurkat T-cells

Jurkat cells (ATCC: TIB-152) were grown in a T-75 cell culture flask supplemented with an RPMI-based medium containing 10% FCS, 1% Penicillin/Streptomycin/L-Glutamine at 37°C/5% CO_2.

Madin-Darby canine kidney (MDCK) II cells

MDCK II cells were cultured in T-75 cell culture flasks in DMEM supplemented with 10% FCS, 1% Penicillin/Streptomycin/L-Glutamine, and 2.5% HEPES at 37°C/5% CO_2. Cells were detached and singularized with Trypsin-EDTA before being passaged thrice per week.

In vitro/ex vivo treatment

Macrophages were treated *in vitro*/*ex vivo* as follows:

MPO, NGAL, ELA-2:

0.5μM for 3h

GNP:

100μM for 1h

DM-α-KG:

1mM concomitantly with GNP

MitoT and TPP (Triphenylphosphonium)

Pre-incubation: 100μM for 1h

concomitantly with bacterial stimulation/infection: 100µM

ABAH:

100µM concomitantly with MPO

Antioxidants (N-acetyl-L-cystein (ACC) and α-D-Tocopherolsuccinate):

10mM (ACC) and 1nM (Tocopherol) concomitantly with MPO

BPTES:

3µM concomitantly with efferocytic treatment or bacterial stimulation

EGCG:

Pre-incubation: 100µM for 1h

concomitantly with bacterial stimulation/infection: 100µM

Assessment of mtROS, cROS, and MMP using flow cytometry

Primary macrophages were seeded with 2.5x105 viable cells per well in a 48-well plate. After adherence, heat-killed *P. aeruginosa* (PA), *K. pneumoniae* (KP), or *S. pneumoniae* (SP) (MOI 100) were added for 6-8h. Subsequently, cells were incubated with MitoSOX Red (3.5µM, 15min) and CM-H2DCFDA (3.5µM, 15min) for the assessment of mtROS or cROS, respectively, at 37°C/5% CO_2. MMP was determined using JC-1 (7.7µM, 30min) or TMRM+ (20nM, 30min) at 37°C/5% CO_2. Oligomycin (1.5µM, 30min) and CCCP (50mM, 30min) constitute important controls to induce a high or low MMP, respectively. Finally, cells were transferred to round-bottom test tubes for flow-cytometric analysis (BD LSRFortessa, BD).

Protein concentration of BALF and cell culture supernatant

BALF or conditioned cell culture supernatant was placed in a protein concentrator (2-6mL capacity, molecular weight cut-off (MWCO) 3kDa) and centrifuged at 4000g, 30min, at RT. Concentrated retentates were collected from sample chambers to treat AMs with concentrated BALF or cell culture supernatant as indicated.

Flow cytometric immunophenotyping of BALF and cell sorting

BAL was centrifuged and subsequently counted with an NC-250 NucleoCounter (ChemoMetec, Denmark). Cells were resuspended in flow cytometry buffer (PBS+/+, 0.09% sodium azide, 0.5% BSA, 2mM EDTA, pH=7.2) containing 10% Fc blocking reagent (Gamunex)

and indicated antibodies for surface staining for 30min at 4°C. Cell suspensions were centrifuged and resuspended in flow cytometry buffer. SYTOX Blue or 7-AAD were added immediately prior to flow cytometric immunophenotyping and/or sorting to discriminate viable from dead cells.

For quantification of apoptosis induction, cells were resuspended in annexin V binding buffer (10 mM HEPES, 140 mM NaCl, and 2.5 mM $CaCl_2$) at a concentration of 0.1-1.0x10e^{7}cells/mL. Then, 100µL of the cell suspension was transferred to a round-bottom test tube. Subsequently, 5µL of each, a Pacific Blue anti-Annexin V antibody and 7-AAD, were added to the cell suspension. The solution was vortexed gently and incubated for 15 min at RT in the dark. Finally, 400µl of Annexin V binding buffer was added. Flow cytometric analysis was performed with a BD LSRFortessa or BD FACSAria III cell sorter.

Intracellular flow cytometry

AMs were harvested from BALF 24h after acid aspiration compared to sham treatment. After surface staining for alveolar macrophages, cells were fixed and permeabilized using the eBioscience Foxp3/Transcription Factor Staining Buffer Set (Invitrogen) according to the manufacturer's instructions. Each sample was split into three and intracellularly stained with an APC anti-Ly6G antibody (2µg/mL = 1:100), APC antiEpCAM antibody (2µg/mL = 1:100), and primary anti-MPO polyclonal antibody (1:1000) followed by secondary AF488-coupled antibody (1:1000). Unpermeabilized fully stained samples served as baseline controls. Samples were prepared and subjected to flow cytometric measurement. Data was expressed as MFI of intracellular Ly6G/EpCAM/MPO and % of AMs positive for Ly6G/EpCAM/MPO.

Intratracheal application

For intratracheal (i.t.) instillation, mice were premedicated with atropin (0.05mg/kg) and anesthetized by isoflurane inhalation. More specifically, oxygen containing 4% isoflurane was supplied under constant flow into the induction chamber of an anesthesia device. The induction chamber was automatically heated up to maintain body temperature upon device ignition. Once gas flow had been stabilized, mice were placed into the induction chamber until loss of their righting reflex, upon which they were transferred from the induction chamber onto the rodent tilt table. Mice were then fixed by their incisors and hindlegs in a supine

position, while 2-3% isoflurane was applied at a flow rate of 0,3L/min through a nose mask. An endotracheal tube was then inserted orally, passing between the vocal cords into the trachea. Using a 27G syringe, mice were inoculated intratracheally with bacteria/virus or HCl/chemicals/drugs were instilled intratracheally as indicated.

Induction of acid aspiration

Acid pneumonitis was induced by instillation of HCl (50µl, 0.1M) i.t.. Sham-treated controls received NaCl (50µl, 0.9%).

Bacterial culture of *P. aeruginosa*

P. aeruginosa, strain PA103, was streaked on 4 blood agar plates and left to grow at 37°C/5% CO_2 for 8-10h two days prior to infection. Single colonies of P. aeruginosa were then harvested using an inoculation loop and cultured in 50mL of Luria broth (LB) medium at 37°C with aeration in an orbital shaker (180rpm) overnight until bacterial solution was fully saturated. On the day of the experiment, 10mL of the bacterial solution was then diluted 10-fold (V=100mL) with LB medium and cultured at 37°C with aeration in an orbital shaker (180rpm) until desired OD (mid-log phase) was reached (OD_{600nm}=2, after 2-fold dilution with LB medium → expected OD_{600nm}=1.4-1.6). LB medium was used as baseline for measurement of optical density. The bacterial solution (V=100mL) was transferred to 2x50mL conical tubes and pelleted at 4000rpm, 10°C, 10min followed by thorough washing with NaCl 0.9%. Bacterial pellets were resuspended and pooled in V=10mL NaCl. This bacterial stock solution equals $2x10^{10}$CFU/mL. Serial dilutions of the bacterial stock solution were performed to prepare a bacterial inoculum tailored to the experimental aim:

1. 20-fold dilution; c=$10e^{9}$CFU/mL
    i. Heat killing (90°C, 60min, 850rpm on Thermoshaker) of bacteria:
    ii. In vitro bacterial stimulation of macrophages with heat-killed bacteria
    iii. Multiplicity of infection (MOI)=100, for 6-8 hours
2. 2000-fold dilution; c=$1x10e^{7}$CFU/mL
    i. In vitro bacterial infection of macrophages with viable bacteria
    ii. Multiplicity of infection (MOI)=10
3. 20,000-fold dilution; c=$1x10e^{6}$CFU/mL

i. In vivo infection of mice with viable bacteria
ii. Infectious inoculum=5x10e^4 CFU/50µL NaCl 0.9%
iii. Route of administration: Intranasally

Infection dose was confirmed by overnight culture of serial dilutions of the infectious inoculum on blood agar plates. Colony-forming units were quantified 16h later.

Bacterial culture of *K. pneumoniae*

K. pneumoniae (ATCC 700721) was streaked on 4 blood agar plates and left to grow at 37°C/5% CO_2 for 8-10h on the day prior to infection. Beacteria were then harvested using an inoculation loop and cultured in 2mL of Luria broth (LB) medium at 37°C with aeration in an orbital shaker (180rpm) overnight until bacterial solution was fully saturated. On the day of the experiment, the bacterial solution was diluted 5-fold (V=10mL) with LB medium and cultured for about an hour at 37°C with aeration in an orbital shaker (180rpm) until desired OD (mid-log phase) was reached (OD_{600nm}=2). LB medium was used as baseline for measurement of optical density. The bacterial solution was pelleted at 4000rpm, 10°C, 10min followed by thorough washing with NaCl 0.9%. Bacterial pellet was resuspended in NaCl to an OD of 1 (=2x10^8 CFU/mL). Serial dilutions of the bacterial stock solution were performed to prepare a bacterial inoculum tailored to the experimental aim. Infection dose was confirmed by overnight culture of serial dilutions of the infectious inoculum on blood agar plates. Colony-forming units were quantified 16h later.

Bacterial culture of *S. pneumoniae*

S. pneumoniae serotype 3 was streaked on 4 blood agar plates and left to grow at 37°C/5% CO_2 for 8-10h on the day prior to infection. *Pneumococci* were then harvested using an inoculation loop and cultured in liquid THY medium (30g Todd-Hewitt broth powder; 5g yeast extract; 1L ddH_20) containing 10% heat-inactivated FCS at 37°C/5%CO_2 until the desired optical density (OD_{600nm}) of 0.03-0.04 was reached. Once the OD_{600nm} of 0.03-0.04 had been established, liquid culture was stored on ice overnight. On the day of infection, the liquid bacterial culture was removed from ice and allowed to grow at 37°C/5% CO_2 for 3h until an OD_{600nm} of 0.3-0.4 (equals 3-4x10^8 CFU/mL) was achieved, upon which it was centrifuged at 3100U/min, for 10min, at 10°C, at a deceleration rate of 1. Bacteria were then resuspended

in the appropriate volume of sterile NaCl 0.9% in order to achieve a concentration of $1x10^9$CFU/mL and were further diluted up to a final concentration that matches the infectious. Infection dose was confirmed by overnight culture of serial dilutions of the infectious inoculum on blood agar plates. Colony-forming units were quantified 16h later.

Influenza A virus propagation and titration

Influenza A virus/PR8/34 (H1N1) was propagated on MDCK II cells. Cells were passaged in a T75-cell culture flask at a ratio of 1:3 one day prior to infection up to 85-90% confluency at the time point of infection. Cells were then infected at a 0.001 multiplicity of infection (MOI). The virus dilution was prepared in MDCK II infection medium (MDCK II medium supplemented with 0.2% BSA instead of FCS). Cells were inoculated with 5mL virus dilution for 1h at 37°C/5% CO_2. After that, they were washed and further incubated with 10mL infection medium containing immobilized Trypsin (Trypsin-TPCK) in a 1:1000 dilution. Cell culture supernatants containing virus particles released from the infected cells were harvested after 36-48h when a cytopathic effect of approximately 70% had been achieved and centrifuged at 1600rpm at 4°C for 30min. Supernatants were aliquoted and stored at -80°C.

To determine the amount of virus particles capable of multicycle replication (foci forming units, ffu), MDCK II cells were seeded in T-shaped 96-well plates one day prior to infection. Cells were infected with 50µL of serial 1:10 dilutions of the virus stock in PBS+/+ containing 0.2% BSA and 1% Penicillin/Streptomycin/L-Glutamine, covering a range of dilutions from 10^{-1}-10^{-8}. Virus dilutions were inoculated at 37°C/5% CO_2 for 45-60min. Cells were then covered with 100µL Avicel medium (10% 10X MEM, 30% ddH2O, 0.3% BSA, 1% DEAE dextran, 0.3% $NaHCO_3$, 1% Penicillin/Streptomycin, 1.25% Avicel) containing 1µg/mL Trypsin-TPCK. Due to its high viscosity, Avicel prevents viral spread through the cell culture by diffusion and only allows for virus spread from cell to cell. Cells were incubated for further 24-36h at 37°C/5% CO_2, to allow formation of foci caused by local virus propagation. After this incubation step, PBS+/+ was added to the cells for 10-15min at RT, in order to reduce Avicel viscosity. Following thorough washing with PBS+/+, cells were fixed and permeabilized through the addition of fixing solution (PBS+/+, 3.7% PFA, 1% Triton X-100) for 30min at RT. After that, fixing solution was discarded, cells were washed thoroughly with washing solution (PBS+/+, 0.05% Tween 20), and plates were left to dry. Plaques were visualized by immunohistochemical staining.

Incubation with a primary anti-influenza nucleoprotein (NP) antibody (diluted 1:100 in PBS+/+, 3% BSA) for 1h at RT was followed by incubation with a secondary, horseradish peroxidase (HRP)-marked, anti-mouse antibody (diluted 1:1000 in PBS+/+, 3% BSA) for 1h at RT. Addition of TrueBlue, an HRP substrate yielding a blue color after enzymatic progressing, allowed for counting of the number of foci per well. The titer of the virus stock was calculated according to the following equation: number of ffu/well * 20 ($V_{infection}$ = 50µl) * 10^x (dilution where single foci could be counted) = number of ffu/mL.

Bacterial superinfection of IAV pneumonia followed by Spn

For bacterial superinfection, mice were inoculated with 100ffu of Influenza A virus (PR8) diluted in 70µl sterile PBS-/- i.t.. Seven days after Influenza A virus infection, mice were treated with GNP (50µl, 300µM) or DMSO (control for GNP) i.t. followed by intranasal (i.n.) infection with S. pneumoniae (30CFU/50µl NaCl 0,9%) two hours later.

mtROS production *ex vivo* in AMs and MDMs after IAV pneumonia

Mice were infected i.t. with 200ffu *Influenza A virus* (PR8) diluted in 70µl sterile PBS-/-. 7 or 14 days after *Influenza* infection, cellular fraction of BALF was seeded *ex vivo*, purified by adherens, and stimulated with heat-killed *P. aeruginosa* for 6-8 hours. Consecutively, surface staining for AMs and MDMs including CD206 was performed before MitoSOX Red was added. Cells were then subjected to flow cytometric analysis quantifying mtROS production *ex vivo* by and CD206 expression of AMs and MDMs.

mtROS production using live cell confocal microscopy

To measure mtROS production *ex vivo*, $2x10^5$ AMs were harvested from BALF after acid aspiration (24h to 8d HCl) compared to sham and seeded into 35mm glass-bottom cell culture dishes (Greiner AG) supplemented with full medium. Upon adherens, cells were pre-incubated with 100µM MitoT (control/carrier=TPP) for 1h before being stimulated stimulated with heat-killed PA (MOI=100, for 6-8h) in presence of 100µM MitoT (control/carrier=TPP). Subsequently, macrophages were incubated with the mitochondria-targeted dye MitoNeoD (5µM, 20min) in culture medium at 37°C/5% CO_2. Cells were then washed with pre-warmed PBS+/+ and images were acquired using a STELLARIS 5 confocal scanning microscope (Leica

Microsystems, Wetzlar, Germany) with an 80% white laser and 2% intensity excitation at 488nm, and emission detected between 520–540 nm. The images were analyzed using LAS X software (Leica Microsystems, Wetzlar, Germany).

Efferocytosis, continued efferocytosis, and efferocytic uptake

Induction of apoptosis

Murine bone marrow-derived PMNs were resuspended at 1-5x10^6 cells/mL in an RPMI-based medium containing 10% FCS and 1% Penicillin/Streptomycin/L-Glutamine before 0.2µM staurosporine was added. The cell suspension was incubated for 6 hours at 37°C/5%CO_2. MLE-12 cells and pAECs were treated with 0.4µM staurosporine for 24 hours at 37°C/5% CO_2 in MLE or pAEC cell culture medium, respectively. Finally, cells were centrifuged and washed thoroughly to remove extracellular staurosporine. Jurkat cells were exposed to 150mJ/cm^2 ultraviolet C (Stratalinker) and further incubated in RPMI only (serum starvation) for 5-6 hours to induce apoptosis. A subsequently performed flow cytometry-based annexin V/7-AAD staining confirmed equal amounts of apoptotic cells (75 +/- 5%) and less than 10% dead cells for both PMNs and AECs.

Efferocytosis

For all efferocytosis experiments, three apoptotic cells (PMNs or AECs) per macrophage were added, meaning an apoptotic cell to efferocyte ratio of 3:1 (AC to EC ratio), unless otherwise stated, and incubated for 4 hours before apoptotic cells were removed. These efferocytosis experiments refer to efferocytosis as a macrophage treatment.

Efferocytic capacity

When determining the efferocytic capacity of primary macrophages *in vitro*, i.e., their capacity to clear apoptotic cells, bone-marrow-derived apoptotic PMNs were pre-incubated with CellTrace Calcein Red-Orange (5µM, 30min) or DiD (5µM, 10min) at a cell concentration of 1-10x10^6 cells/mL. *Ex vivo* assessment was conducted with tdtomato+ bone-marrow-derived apoptotic PMNs. Apoptotic cells were added at an AC to EC ratio of 3:1 and incubated for 60 min before apoptotic cells were removed. Macrophages were then subjected to flow cytometric analysis to quantify the fluorescence signal of CellTrace Calcein Red-Orange, DiD,

or tdtomato in macrophages. The mean fluorescence intensity and % of positive macrophages correlate with the capacity of macrophages to clear apoptotic bodies.

Continued efferocytosis

Quantification of continued efferocytosis, referring to the continued clearance of apoptotic cells, was performed in a two-step model. During the first round of efferocytosis, macrophages were incubated with either apoptotic PMNs or AECs for 4 hours compared to control (no efferocytosis). Then, samples were stimulated with heat-killed P. aeruginosa (MOI=100, 6-8 hours). In a second round of efferocytosis, macrophages of all conditions were incubated with apoptotic Calcein Red-Orange pre-stained PMNs, to determine their efferocytic capacity via flow cytometry.

Sample preparation for fixed-cell confocal microscopy

2-3x10^5 AMs were seeded equally on high-precision coverslips (diameter: 10mm; thickness: #1.5H) and treated as indicated. MitoTracker Deep Red or LysoTracker Red DND-99 was added prior to fixation/permeabilization when indicated. Cell fixation was achieved by adding 4% PFA (pH 7.4) for 10min at RT. Then, cells were thoroughly washed with PBS. Next, PBS containing 0.1% Triton X-100 had been applied to permeabilize cells at RT for 15min before cells were rinsed with PBS. Blocking was performed by adding 5% goat serum containing 0.1% sodium azide at RT for 60min, followed by staining with primary antibody (1:1000) in 5% goat serum containing 0.1% sodium azide overnight at 4°C. The next day, cells had been thoroughly washed with PBS-T (Tween 0.05%) before secondary antibody (1:1000) in 5% goat serum containing 0.1% sodium azide, was added to the cells for 1h at RT protected from light. Cells were thoroughly washed with PBS-T. Nuclei were stained with DAPI 10µg/mL in PBS for 10 minutes and rinsed with PBS-T. Finally, coverslips were air-dried as well as mounted with ProLong glass antifade mountant (ThermoFischer Scientific). After >24h coverslips were subjected to confocal imaging.

Continued efferocytosis applying confocal microscopy

AMs were seeded on high-precision cover slips as described above and incubated with pre-stained apoptotic PMNs (DiI: 5µM, 10min) for 4h at an AC:EC ratio of 3:1 compared to control.

PMNs were washed away before macrophages were stimulated with heat-killed *P. aeruginosa*, MOI = 100, for 6-8 hours. Then, all conditions received pre-stained apoptotic PMNs (DiD: 5µM, 10min) for 4h at an AC:EC ratio of 3:1. Cell fixation and nuclear staining had been performed as mentioned above before samples were subjected to confocal microscopy. Single xy confocal images were acquired with a 20x 0.75NA air objective with a pixel size of 0.189x0.189 um. For the excitation of DAPI we used 0.2% of the power of a 405nm laser while for the excitation of DiI we used 2.5% of the 549nm laser line and for the DiD 0.5% of the 644nm laser line, both derived from a WLL which was operated at 50% of its nominal power.

Ucp2 transcription *in vitro*

RNA was isolated using RNeasy Micro Kit (QIAGEN) according to manufacturer's protocol. 250ng of isolated RNA was reverse transcribed into cDNA. Quantitative PCR was performed with SYBR green I in the AB StepOnePlus Detection System (Applied Bioscience). mRNA amounts are presented as fold change normalized to β-actin expression as well as relative to the untreated/sham control. The following primers were used: murine β-actin (forward primer, 5'-ATGGGAAGCCGAACATACTG-3'; reverse primer, 5'-CAGTCTCAGTGGGGGTGAAT-3') and murine Ucp2 (forward primer, 5'-AAGGGCTCAGAGCATGCAG-3'; reverse primer, 5'-TGGAAGCGGACCTTTACCAC-3').

Bacterial killing assay

Primary macrophages were cultured for 3 hours before analysis. *P. aeruginosa*, *S. pneumoniae*, and *K. pneumoniae* were grown at mid-log phase in LB medium. Subsequently, bacteria were added with a calculated multiplicity of infection (MOI) of approximately 5 (PA), 10 (KP), and 250 (Spn), and both plates were incubated for 1h (PA and KP) or 10 min (SP) with antibiotic-free medium. Then both plates were washed four times again. One plate was immediately lysed with distilled water to assess intracellular bacterial uptake (time point t0). The other plate was left for an additional 1.5h (PA), 3h (KP), or 20 min (Spn) and subsequently lysed (time point t1) to assess intracellular bacterial killing (relative to bacterial uptake). Serial dilutions of the lysate were incubated overnight on blood agar plates to quantify real MOI.

Bacterial phagocytosis

Bacterial phagocytosis was quantified with the following two techniques. Firstly, bacterial uptake as determined by intracellular bacterial outgrowth at time point t0 is integral part of the above-mentioned bacterial killing assay. Secondly, FITC-labeled E. coli bioparticles (Invitrogen Cat No E2861) were opsonized with Opsonizing Reagent (Cat No E2870) as per manufacturer's instructions. Macrophages were then incubated with FITC-labeled E. coli for 1h, MOI=10, at 37°C/5%CO_2. In parallel, one sample per each condition was incubated at +4°C on ice to serve as a baseline. Cells were washed and prepared to be analyzed by flow cytometry. Phagocytosis Index was quantified as follows: (MFI FITC-channel * % pos. at 37°C) - (MFI FITC-channel * % pos. at 4*C).

Cytokine Measurements

Primary macrophages were cultured for 3h prior to analysis and incubated with heatkilled P. aeruginosa (MOI 100) for 6-8 hours. Protein concentrations of selected cytokines and chemokines were measured in supernatants of macrophages using a BioPlex MAGPIX Multiplex Reader (BIO-RAD, United States) according to manufacturer's instructions. Data were analyzed with Bio-Plex Data Pro software.

Microarray

Purified total RNA was amplified using the Ovation PicoSL WTA System V2 kit (NuGEN Technologies, Bemmel, Netherlands). Per sample, 2µg amplified cDNA was Cy-labeled using the SureTag DNA labeling kit (Agilent, Waldbronn, Germany). The Cy5-labeled cDNA was hybridized overnight to 8 x 60K 60mer oligonucleotide spotted microarray slides (Agilent Technologies, design ID 074809). Hybridization and subsequent washing and drying of the slides was performed following the Agilent hybridization protocol. The dried slides were scanned at 2 µm/pixel resolution using the InnoScan is900 (Innopsys, Carbonne, France). Image analysis was performed with Mapix 8.2.5 software, and calculated values for all spots were saved as GenePix results files. Stored data were evaluated using the R software (Team, 2007) (3.5.1) and the limma package (3.30.13) from BioConductor. Gene annotation was supplemented by NCBI gene IDs via bioMart (accessed 2018-03-08). Mean spot signals were background corrected with an offset of 1 using the NormExp procedure on the negative control spots. The logarithms of the background-corrected values were quantile-normalized.

The normalized values were then averaged for replicate spots per array. From different probes addressing the same NCBI gene ID, the probe showing the maximum average signal intensity over the samples was used in subsequent analyses. Genes were ranked for differential expression using a moderated t-statistic. Pathway analyses were done using gene set tests on the ranks of the t-values. Gene sets were defined according to the KEGG database (accessed 2018-03-08).

Extracellular flux analysis

Real-time bioenergetic profiles of macrophages were observed by measuring OCR and ECAR using either Agilent Seahorse XF HS Mini or XFe96 analyzer (Seahorse Bioscience, Agilent Technologies, North Billerica, MA). Macrophages were plated on an 8-well XF HS Mini PDL and a 96-well XFe96 cell culture microplate at a density of 25,000 cells or 70,000 cells per well, respectively. After indicated treatments, extracellular flux analysis was performed as per manufacturer's instructions. In brief, cellular bioenergetics were investigated by applying an “XF Mito Stress Test” or “XF Glycolysis Stress Test”. “XF Mito Stress Test”, quantifying OCR, necessitates the sequential injection of 1.5µM oligomycin, 2.5µM carbonyl cyanide 4-(trifluoromethoxy) phenylhydrazone (FCCP), and 0.5/0.5µM rotenone/antimycin A. “XF Glycolysis Stress Test”, measuring ECAR, required the sequential injection of 10mM glucose, 1.5µM oligomycin, and 50mM 2-DG. To reveal the metabolic phenotype and function of macrophages, “XF Substrate Oxidation Stress Test” was conducted, combining pathway-specific inhibition of the primary mitochondrial substrates with a subsequent “XF Mito Stress Test”. Therefore, 2µM UK5099, 3µM BPTES, 4µM Etomoxir, and medium only (control) were injected concomitantly in Port A of separate wells to interrogate the contribution of glycolysis, glutaminolysis, or fatty-acid oxidation to mitochondrial respiration. Each of these injections were followed by an “XF Mito Stress Test” as described above. The relative importance of each of the mentioned pathways for feeding mitochondrial respiration was determined by the potential of the pathway-specific inhibitors to reduce maximal OCR in comparison to the uninhibited control meaning the greater the reduction of maximal respiration, the greater the cell relies on the specific pathway for fueling mitochondrial respiration and vice versa. Data were analyzed with Seahorse Analytics (Agilent).

Western Blot

Macrophages were treated as indicated, detached by adding Trypsin/EDTA for 10min at 37°C/5%CO_2. Cells had been centrifuged at 500g for 10min before supernatant was discarded. Subsequently, cell pellet was resuspended in lysis buffer containing 900µL NP-40 buffer, 100µL Proteinase-Inhibitor Cocktail (PIC), and 3.4µL DDT. Samples were then incubated on ice for 30min while being puls-vortexed every 5-10min. Finally, cell debris was precipitated by centrifugation at maximum speed (>= 16,000g) for 15min at 4°C. Protein concentration was quantified by Bradford Assay according to manufacturer's instructions. A sample volume containing 20-30µg of protein was mixed with loading buffer (900µL 4x Laemmli buffer + 100µL 2-Mercaptoethanol) in a ratio of 3:1. Samples were further boiled at 95°C for 5min before being cooled on ice again. 20-40µg of total protein per well were loaded on a gel (5-15%). The membrane was blocked at RT for 1h in 2% BSA in TBS-T 0.01%. Primary antibody solution was prepared by diluting UCP2 (D105V) Rabbit mAb 1:1000 in 2% BSA in TBS-T 0.01% and added to membrane overnight at 4°C. The membrane was washed three times with TBS-T before the secondary antibody (HRP anti-Rabbit 1:1000) was added for 1h at RT. Finally, imaging was performed. To detect the b-Actin or GAPDH loading control, the membrane was stripped for 30min at RT and subsequently incubated with primary and secondary antibody.

TUNEL assay

In situ nick-end labeling of nuclear DNA fragmentation was performed with a TUNEL apoptosis detection kit (DeadEnd Fluorometric TUNEL system, Promega) according to the supplier's instructions. For the acquisition of fluorescence images of the TUNEL staining, we used the EVOS widefield microscope and the 10x air objective performing a tiled fluorescence acquisition, capturing the fluorescence signal as well as the transmitted light for brightfield images. Similarly, we captured the brightfield images of the H&E staining setting the camera of the system to color mode. The number of TUNEL-positive cells was counted from the widefield fluorescence images using a custom-made Fiji macro. After thresholding the positive TUNEL cells were automatically counted within the boundaries of the lung tissue defined by the brightfield images. Their number was then normalized by the total tissue area and reported as the number of cells per mm^2 tissue.

Mitochondrial content *in vivo* (quantitative PCR)

DNA from cell lysates of alveolar macrophages, harvested 24 hours after acid aspiration compared to sham treatment, was isolated using DNeasy Blood & Tissue Kit (QIAGEN) according to manufacturer's protocol and normalized using NanoDrop (ThermoFischer Scientific). Quantitative PCR was performed with SYBR green I (Invitrogen) in the AB StepOnePlus Detection System (Applied Bioscience). Mitochondrial content was quantified by the ratio of mitochondrial DNA to genomic DNA. The following primers were used: genomic DNA (murine β2 microglobulin) (forward primer, 5'-ATGGGAAGCCGAACATACTG-3'; reverse primer,
5'-CAGTCTCAGTGGGGGTGAAT-3') and mitochondrial DNA (forward primer,
5'-CTAGAAACCCCGAAACCAAA-3'; reverse primer,
5'-CCAGCTATCACCAAGCTCGT3').

Mitochondrial content *in vitro* (confocal microscopy)

After treatment, mitochondria were stained with MitoTracker deep red 100nm for 30min, before being fixed and permeabilized. Primary antiTOM20 recombinant rabbit monoclonal antibody was added at a 1:1000 dilution, followed by Alexa Fluor 555 coupled goat anti-rabbit recombinant secondary antibody at a 1:1000 dilution in 5% goat serum containing 0.1% sodium azide. Successful mitochondrial staining was confirmed by colocalization of anti-TOMM20 and MitoTracker deep red staining. TOMM20 is a translocase of the outer mitochondrial membrane. Mitochondrial content was finally quantified by the mean intensity of the anti-TOMM20 signal. Confocal images were acquired with an SP8 confocal microscope (Leica Microsystems). Stained samples were scanned sequentially using a PL APO 63xOil /1.40 NA objective with a voxel size of 28x28x200nm. To measure the mean intensity of TOMM20, we acquired confocal images with a lower magnification objective (20xAir/0.75NA) to capture as many cells as possible. The mean intensity of the TOMM20 marker as a surrogate marker for mitochondrial content was quantified as follows: The images were computationally cleared, and upon a maximum intensity projection and thresholding we measured the mean fluorescence intensities of the TOM20 positive pixels.

Uptake of MPO (confocal microscopy)

After treatment macrophages were then stained with 50nM LysoTracker Red DND-99 in pre-warmed full medium for 1h before being fixed and permeabilized. Samples were incubated with a primary anti-MPO polyclonal rabbit anti-mouse antibody at a 1:1000 dilution followed by a secondary polyclonal goat anti-rabbit IgG (H+L) highly cross-adsorbed AF488-coupled antibody at a 1:1000 dilution.

Uptake of MPO in presence of Mannose and LysoTracker close-up view:

Confocal z-stacks were acquired with a 20x 0.75NA air objective and a voxel size of 0.284x0.284x0.586 um. The close-up views were captured with a 63x 1.4NA oil objective using a pixel size of 39nm and a pinhole of 70um.

Bioluminescent metabolic measurement

AMs were isolated from WT or Ucp2-/- mice and seeded at a density of 5x104 cells per well supplemented with 100µL cell culture medium. In the following, cells were treated as indicated. Supernatant of each well was taken up, diluted 50-fold and split into three while cells were lysed in 100µL lysis solution (50µL 0.6M HCl and 50µL 1M TRIS) before being split into three. From different fractions of supernatant and cell lysate concentration of glucose, lactate, and glutamine or glutamine and glutamate were quantified, respectively. Measurement was performed by applying Glucose-Glo (Glucose), Lactate-Glo (Lactate), and Glutamine/Glutamate-Glo (Glutamine and Glutamate) kits from Promega according to manufacturer's instructions. For GlucoseGlo kit supernatant was further diluted three-fold. relative light units were measured by a luminometer (Flx800, Biotek). Actual concentrations were then quantified from standard curves of each metabolite.

Statistical analysis

Statistical analyses were performed in GraphPad Prism v.9 software. Data are presented as the means +/- standard error of the mean (s.e.m.). p-values less than 0.05 were considered significant, whereas p-values more than 0.05 were considered nonsignificant and not indicated unless stated otherwise. The mean between two groups was analyzed using the two-sided Student's t-test. Statistically significant differences between the means of three or more unrelated and independent groups were compared using the one-way ANOVA test. p-values were corrected by Dunnet's multiple comparisons test when comparing different groups to

one control group or Tukey’s multiple comparisons test when comparing all different groups with each other. The two-way and three-way ANOVA approaches were used to estimate how the mean of a quantitative variable changes according to the levels of two or three categorical variables, respectively. Šídák's multiple comparisons test was further applied to adjust p-values. Survival distributions of two samples were followed up by a log-rank test (Mantel-Cox test). Data distribution was assumed to be normal, but this was not tested formally. Plated cells were allocated randomly to each treatment group; C57Bl/6 mice were assigned randomly to each treatment group. Data collection and analysis were not performed blind to the conditions of the experiments.

List of abbreviations

4-OI	4-octyl itaconate
AA	Amino acid
ABAH	4-aminobenzoic acid hydrazide
AC:EC-ratio	Apoptotic cell to efferocytic cell ratio
AEC	Alveolar epithelial cell
αKG	Alpha-ketoglutarate or 2-oxoglutarate
ALI	Acute lung injury
AM	Alveolar macrophage
ARDS	Acute respiratory distress syndrome
BAL	Broncho-alveolar lavage
BALF	Broncho-alveolar lavage fluid
BMDM	Bone-marrow-derived macrophage
CAP	Community-acquired pneumonia
CCCP	Carbonyl cyanide m-chlorophenyl hydrazone
CFU	Colony forming unit
COVID-19	Coronavirus disease 2019
cROS	Cytosolic reactive oxygen species
DAMP	Damage- or danger-associated molecular pattern
DI	Dimethyl itaconate
ECAR	Extracellular acidification rate
EGCG	Epigallocatechin-3-gallate
ELA-2	Neutrophil elastase 2
ETC	Electron transport chain
FAO	Fatty acid oxidation
FAS	Fatty acid synthesis
GM-CSF	Granulocyte-macrophage colony-stimulating factor
GNP	Genipin
hAM	Human alveolar macrophage
HAP	Hospital-acquired pneumonia

HCl	Hydrochloric acid
HIF	Hypoxia inducible factor
hIM	Human interstitial macrophage
IAV	Influenza A Virus
IFN	Interferon
IL	Interleukin
IM	Interstitial macrophage
IMM	Inner mitochondrial membrane
i.n.	Intranasally
i.p.	Intraperitoneally
i.t.	Intratracheally
KEGG	Kyoto Encyclopedia of Genes and Genomes
K. pneumoniae/KP	Klebsiella pneumoniae
LPS	Lipopolysaccharide
MDM	Recruited inflammatory monocyte-derived macrophage
mexAM	Murine ex-vivo cultured alveolar macrophages
MFI	Mean fluorescence intensity
MitoT	MitoTEMPO
MLE	Murine lung epithelial cell
MMP	Mitochondrial membrane potential
mtDNA	Mitochondrial DNA
mtROS	Mitochondrial reactive oxygen species
MOI	Multiplicity of infection
MPO	Myeloperoxidase
NGAL	Neutrophil gelatinase-associated lipocalin
OCR	Oxygen consumption rate
OMM	Outer mitochondrial membrane
OxPhos	Oxidative phosphorylation
pAEC	Primary alveolar epithelial cell
P. aeruginosa/PA	Pseudomonas aeruginosa
PAMP	Pathogen-associated molecular pattern
PM	Peritoneal macrophage

PMN	Polymorphonuclear leukocyte (=neutrophil)
PPAR -γ	Peroxisome proliferator-activated receptor gamma
PRR	Pattern recognition receptor
ROS	Reactive oxygen species
S. pneumoniae/Spn	Streptococcus pneumoniae
TCA cycle	Tricarboxylic acid cycle
TMRM+	Tetramethylrhodamine-methylester
TNF-α	Tumor necrosis factor-α
TOMM20	Translocase of the outer mitochondrial membrane 20
TPP	Triphenylphosphonium
Ucp2	Uncoupling protein 2
VAP	Ventilator-associated pneumonia
WT	Wildtype

Resources Table

Machines and devices

Machine or device	Identifier	Source
Anesthesia workstation	MiniHub V2.1 gas anesthesia workstation for small animals	TemSega
Flow Cytometers	BD LSRFortessa	Becton Dickinson
	BD FACS ARIA III	
Microscopes	BX41 light microscope	Olympus
	EVOS M700	Thermo Fisher
	SP8 confocal microscope	Leica Microsystems
	STELLARIS 5 confocal microscope	Leica Microsystems
Multiplex Reader	Bio-Plex MAGPIX Multiplex Reader	BIO-RAD
Seahorse	Seahorse XFe96 and XF HS Mini Analyzer	Agilent
Cell Counter	NucleoCounter NC-250	ChemoMetec
PCR System	StepOnePlus™ Real-Time PCR System	Applied Biosystems
Fluorescence Microplate Reader	FLx800	Biotek
UV Cross Linker	Stratalinker	Stratagene
Dissociator	gentleMACS™ Dissociator	Miltenyi Biotec

Mitochondrial probes

Mitochondrial probe	Identifier	Source
MitoSOX	#M36008	

CM-H2DCFDA	#C6827	Invitrogen by Thermo Fisher Scientific
JC-1	#T3168	
TMRM	#T668	
MitoTracker Deep Red FM	#M22426	
MitoTEMPO	#SML0737	Sigma-Aldrich
Methyl-TPP	#468002	

Antibodies and fluorescent dyes

Target	Fluoro-chrome	Clone	Isotype	Host species	Identi-fier	Source
CD45	APC-Cy7	30-F11	IgG_{2b},κ	Rat	#103116	BioLegend
Ly6G	APC	1A8	IgG_{2a},κ	Rat	#127614	
Ly6G	PE-Cy7	1A8	IgG_{2a},κ	Rat	#127618	
CD11b	FITC	M1/70	IgG_{2b},κ	Rat	#101206	
CD11c	PE-Cy7	N418	Armenian Hamster IgG	Arme-nian Hams-ter	#117318	
CD11c	FITC	N418	Armenian Hamster IgG	Arme-nian Hams-ter	#117306	
7-AAD	7-AAD	n.a.	n.a.	n.a.	#420404	
Annexin V	Pacific-Blue	n.a.	n.a.	n.a.	#640918	
CD206	APC	C068C2	IgG_{2a},κ	Rat	#141708	
CD326/ EpCAM	APC	G8.8	IgG_{2a},κ	Rat	#118214	
CD170/ Siglec-F	BV421	E50-2440	IgG_{2a},κ	Rat	#565934	BD Biosciences
CD11b	Horizon V500	M1/70	IgG2b, κ	Rat	# 562127	
CD45		30-F11	n.a.	Rat	#553078	

CD16/32	Biotiny-lated	2.4G2	n.a.	Rat	#553143	
CD31		MEC13.3	n.a.	Rat	#553371	
n.a.	CellTrace™ Calcein Red-Orange, AM	n.a.	n.a.	n.a.	#C34851	Invitrogen
Tomm20	Recombinant Alexa Fluor® 555 Anti-TOMM20 antibody	EPR15581-54	Alexa Fluor® 555 Rabbit IgG, mono-clonal (EPR25A)	Rabbit	#ab221292	Abcam
UCP2	UCP2 (D1O5V) Rabbit mAb	D1O5V	Rabbit IgG	Rabbit	#89326	Cell Signaling
β-Actin	β-Actin Antibody	n.a.	n.a.	Rabbit	#4967	
GAPDH	GAPDH Antibody	n.a.	n.a.	Rabbit	#PA1-987	Invitrogen

Critical commercial assays and kits

Assay	Identifier	Source
WST-1 Assay Kit (Cell Proliferation)	#ab65473	Abcam
Seahorse XFp Cell Mito Stress Test Kit	#103010-100	Agilent
Seahorse XF Cell Mito Stress Test Kit	#103015-100	
Seahorse XFp Mito Fuel Flex Test Kit	#103270-100	
Seahorse XF Mito Fuel Flex Test Kit	#103260-100	

Bio-Plex Pro Human Cytokine 27-plex Assay	#M500KCAF0Y	BIO-RAD
Bio-Plex Pro Mouse Cytokine 23-plex Assay	#M60009RDPD	
RNeasy Micro Kit	#74004	Qiagen
DNeasy Blood & Tissue Kit	#69506	
Macrophage Isolation Kit (Peritoneum), mouse	#130-110-434	Miltenyi Biotec
MACSxpress Whole Blood Neutrophil Isolation Kit, human	#130-104-434	
Neutrophil Isolation Kit, mouse	#130-097-658	
Glucose-Glo	#J6021	Promega
Lactate-Glo	#J5021	
Glutamine/Glutamate-Glo	#J8021	
eBioscience™ Foxp3 / Transcription Factor Staining Buffer Set	#00-5523-00	Invitrogen
Vybrant™ Multicolor Cell-Labeling Kit (DiO, DiI, DiD)	#V22889	
ThermoScientificTM PierceTM, 2-6mL capacity, MWCO 3kDa	#88515	Thermo Fischer Scientific

Chemicals, peptides, and recombinant proteins

Chemical, peptide, or recombinant protein	Identifier	Source
Recombinant Mouse Myeloperoxidase Protein, CF	#3667-MP-250	R&D Systems
Recombinant Mouse M-CSF Protein, CF	#416-ML-050/CF	
Recombinant Human Myeloperoxidase Protein, CF	#3174-MP-250	

Recombinant Mouse Lipocalin-2/NGAL Protein, CF	#1857-LC-050	
Recombinant Mouse Neutrophil Elastase/ELA2 Protein, CF	#4517-SE	
HCl (hydrochloric acid solution) 0,1M 50mL	#2104	Sigma-Aldrich
Staurosporine from Streptomyces sp.	#S5921	
DMSO (dimethylsulfoxide)	#D2650	
2-Oxoglutarsäure-dimethylester	#349631	
(−)-Epigallokatechingallat	#E4143	
(+)-Etomoxir	#E1905	
BPTES	#SML0601	
Mitochondrial Pyruvate Carrier Inhibitor, UK5099	#5.04817	
CCCP	#C2759	
EDTA (ethylenediaminetetraacetic acid)	#108418	Merck
PBS (phosphate-buffered saline)	#D1408-500ML	
NP-40 lysis buffer	#J60766.AP	Thermo Fischer Scientific
Genipin	#466642500	
4-Aminobenzoic Acid (ABAH)	#146210010	
Protease Inhibitor Cocktail (PIC)	#ab65621	Abcam
SYBR green 1	#1725124	Invitrogen

Cell culture/ in-vitro assay media and supply

Medium or supply	Identifier	Source
FBS (Fetal Bovine Serum)	#10270-106	Life Technologies, Gibco
HBSS (hanks buffered saline solution)	#14175-053	
RPMI 1640 medium	#31870-074	

HEPES buffer (4-(2-hydroxyethyl)-1-piperazineethanesulfonic acid)	#15630080	
Insulin-Transferrin-Selenium (ITS - G) (100X)	#41400045	
Dispase II	#17105041	
Deoxyribonuclease I from Bovine Pancreas (>=3000U/mg protein)	#18535	SERVA
Seahorse XF HS mini FluxPak	#103724-100	Agilent
Seahorse XF Pro M FluxPak	#103775-100	
Penicillin(10^3U/mL)-Streptomycin(10mg/mL)-L-Glutamine(200mM) solution	#G1146	Sigma-Aldrich
Sodium Azide	#S2002	
HCl (hydrochloric acid solution) 0,1M 50mL	#2104	
Staurosporine from Streptomyces sp.	#S5921	
DMSO (dimethylsulfoxide)	#D2650-5X5ML	
Bovine Serum Albumin (BSA)	#A7030	
LB medium	#X968.1	Carl Roth
Todd Hewitt Bouillon	#500G	NutriSelect® Plus
Thermo Scientific Blood Agar (TSA with Sheep Blood) Medium	#10362223	Thermo Fischer Scientific
FITC-labeled E. coli bioparticles	#E2861	Invitrogen
Opsonizing Reagent (Cat No)	#E2870	

Anesthesia and in vivo experiments

Anesthetic or supply	Identifier	Source
Isoflurane 250mL (Isofluran)	n.a.	Baxter
Ketaset 100mg/mL injection solution (Ketamin)	n.a.	Zoetis

Xylariem 20mg injection solution (Xylazin)	n.a.	Ecuphar GmbH
Atropin sulfate 0.5mg/mL injection solution (Atropin)	n.a.	B. Braun
Mouse Intubation Pack	#000A3747	Hallowell EMC
Rodent, Tilting WorkStand	#000A3467	

Bacteria and virus

Bacterial culture	Identifier	Source
K. pneumoniae	American Type Culture Collection (ATCC) 700721	Cryo stock
S. pneumoniae (PN23)	PN23	
P. aeruginosa (PA103)	PA103	
Influenza A Virus	Mouse-adapted PR8	

Experimental models: Organisms/strains

Organisms/strains	Genetic Background	Source
WT	C57BL/6N	Charles River
$Ucp2^{-/-}$	B6.129S4-Ucp2tm1Lowl	Laboratory N. Sommer, Justus-Liebig-University Gießen, Germany
$Mpo^{-/-}$	B6.129X1-Mpotm1Lus/J	Charles River

Software

Software	Application	Website
Biorender	Corresponding figures and panels are highlighted:	www.biorender.com

	*Created with BioRender.com	
GraphPad Prism (>v9.5.1)	Statistics	www.graphpad.com
FlowJo (>v10.8)	Analysis of flow cytometry data	www.flowjo.com
Bio-Plex Manager Software	Analysis of Multiplex data	www.bio-rad.com
BD FACSDiva software (v6.1.3)	BD FACS software	www.bdbiosciences.com
Seahorse Analytics	Analysis of Seahorse data	www.seahorseanalytics.agilent.com/Account/Login

Declaration

I declare that I have completed this dissertation single-handedly without the unauthorized help of a second party and only with the assistance acknowledged therein. I have appropriately acknowledged and referenced all text passages that are derived literally from or are based on the content of published or unpublished work of others, and all information that relates to verbal communications. I have abided by the principles of good scientific conduct laid down in the charter of the Justus Liebig University of Giessen in carrying out the investigations described in the dissertation.

The scientific findings from my PhD research, as detailed and presented in this dissertation, have been published online in Science Immunology. The American Association for the Advancement of Science (AAAS) has granted permission to reprint the figures in both the electronic and printed versions of this thesis:

Better J, Estiri M, Wetstein M, et al. Cell type-specific efferocytosis determines functional plasticity of alveolar macrophages. Sci Immunol 2025;10:eadl3852. DOI: 10.1126/sciimmunol.adl3852

An editorial discussed the influence of the published research findings on the scientific community:

Wong AO, Ravichandran KS. Apoptotic cells are not all created equal. Sci Immunol 2025;10:eadv4682. DOI: 10.1126/sciimmunol.adv4682

Some of the figures included in this thesis were created using Biorender.com, as indicated. While some figures are inspired by existing literature, all figures were exclusively designed using Biorender.com and do not contain any copied material from published sources.

Gießen, 21st of August 2025

Place and date | Signature

Acknowledgments

I am deeply grateful to everyone who made my journey through this PhD possible. Your support, encouragement, and camaraderie have been invaluable.

First, I would like to thank the entire team of the Medical IMC/ICU (P-IMC 2.6 and P-ICU 2.5) at the university hospital in Giessen, including the incredible nurses, residents, senior physicians, and directors. Working with you all felt like being part of a big, supportive family. To the nurses and resident colleagues: Thank you for the teamwork, the familiar atmosphere, and all the laughter we shared. To the senior physicians and directors—István V., Matthias H., Khodr T., and Werner S.—I am immensely grateful for your guidance. You are extraordinary doctors and working with you has been inspiring. You opened the door to the world of research while nurturing my growth as an intensive care specialist.

My heartfelt thanks to the entire Herold lab for enriching my research with fruitful discussions and standing by me through both the struggles and triumphs.

To the wonderful technicians— Larissa H., Stefanie J., Florian L., Julia B., Julia S., Maria G., and Josephine G.—your continuous support, both inside and outside the lab, humbles me. You are the heart of the lab that keeps our research going.

I appreciate my consultants—Irina K., Jürgen L., Christina M., Monika H., Learta P.-O., and Maximilian F.—for their invaluable support in my experimental work and for sharing their extensive knowledge.

To all the collaborators on the project, your expertise was indispensable. A special thanks to Ioannis A., Rajkumar S., Siavash M., and Natascha S., whose scientific insights helped place our findings within the broader context of existing literature.

Theresa S. and Mohammad E., sharing an office with you and creating a friendly, enriching atmosphere filled with coffee and tea breaks was a daily joy.

To the entire AG Matt, thank you for supporting my work and helping to achieve the group's greater goals. Our friendship means much to me.

To my dear friends Martin L., Lucas K., Michael W., Marco O., and Mohammad E.—you are like family to me. Martin, I cherish our shared experiments and great talks about biking; your reliability and humor have made you a cherished friend. Lucas, even after you left, your impressive legacy endures, and you remain a role model as a doctor and researcher. You are founder of the unforgotten Matt institute of greatnes and legendariness (MIGL). Michael, your warmth and intelligence were constant, especially during our night shifts filled with music and scientific discussions. Marco, you transformed from merely my English teacher to a source of strength and guidance during happy and tough times sharing my passion for the United States of America. Mohammad, your enthusiasm and support have been invaluable. You are warm hearted, enthusiastic, and passionate personifying the warm Iranian culture and providing us with Iranian black tea and Safran. We shared countless experimental hours, and endless writing sessions. I would not have been able to do this without your help and moral support. I look forward to continuing our journey together and eventually exploring southern Iran.

Susanne H., your exceptional scientific and medical achievements continue to inspire and motivate me. You provided the scientific infrastructure that made this project possible and successful.

To my family—my parents Waltraud and Roland B., my brother Manuel B. and his family, my grandparents Rolf and Edeltraud B., Margarethe D., my godparents Annette and Giso, my cousin Jenny D., and the entire family—words fall short in expressing my gratitude for your unwavering love and support. Everything I have accomplished is because of you. I cherish and love you all deeply. Waltraud and Roland B., and Rolf B., I will forever remember your presence during good times and bad.

Ariana B., the mother of my son and my best friend, I hold our deep friendship, and mutual understanding and support very close to my heart. Sharing the joys of watching our son grow is a treasure.

Marie-Charlotte V., you are the most warm-hearted and understanding person in my life. I appreciate every moment we spend together with Liam—whether at home, on vacation, in swimming pools, or at amusement parks.

To my son Liam B., you are my greatest inspiration and motivation. Watching you grow and spending time with you are the most important things in my life.

Lastly, my deepest thanks to Ully M. Your work ethic, scientific interest, and mastery over both research and clinical practice set a standard of excellence. Thank you for guiding us into the exciting field of immunometabolism and promoting macrophage therapy. I am honored to know you and your family, and I value our relationship immensely. You are a constant source of knowledge and inspiration, and I am grateful for the opportunity to continue working with you.

Thank you all.